Profile Changes in the Propagation of Shock Waves of Varying Curvature

Sarah Soshe Lewin

A dissertation submitted to the Faculty of Engineering and the Built Environment, University of the Witwatersrand, Johannesburg, in fulfilment of the requirements for the degree of Master of Science in Engineering.

Johannesburg, May 2020

Declaration

I declare that this dissertation is my own, unaided work, except where otherwise acknowledged. It is being submitted for the degree of Master of Science in Engineering in the University of the Witwatersrand, Johannesburg. It has not been submitted before for any degree or examination at any other university.

Signed this 9th day of May 2020

Sarah Soshe Lewin

For Ta and his gang

Acknowledgements

I would like to thank my supervisor, Prof B.W. Skews for giving me the opportunity to do this research, and for his unwavering patience and guidance throughout. It is a rare privilege to be mentored by an individual of Prof. Skews' knowledge.

Thanks to Dr R.T. Paton for the assistance and insights he gave with regards to the computational and experimental components of this research.

Thanks also to Mr S. Riekert, Mr L. Claassen, and the entire laboratory staff, for the manufacture of the facility and their assistance with its assembly.

Thanks to my fellow student, Tim, for unassumingly giving generously of his time and assisting with the set-up of the experimental facilities.

Finally, to my parents and sisters, Feig, and Zee; there are truly no words to express my gratitude!

This research was funded by the SITA Air Transport Community Foundation. I am immensely grateful to have been afforded the opportunity. Thank you.

Abstract

In two distinct studies, the change in the profile of a curved shock wave, from one continuous shock front to a configuration resembling a symmetrical pair of Mach reflections, was observed. The physical mechanisms associated with the evolution of the shock profile was evaluated for shock waves with initial profiles comprising a cylindrical arc, placed in-between two straight segments. This was achieved through a series of Computational Fluid Dynamics (CFD) simulations and experimental tests. An understanding of this phenomenon contributes fundamental insights regarding the behaviour of curved shock waves.

The propagation of these shock waves in a converging channel was modelled numerically. The temporal variation of the pressure distribution immediately behind the shock wave was examined. This revealed a pressure imbalance in the region where the curved (which was initially cylindrical) and straight shock segments meet. This imbalance occurs due to the difference in the propagation behaviour of curved and planar shock waves, and results in the development of reflected shocks on the shock front.

Throughout the numerical simulations, the angle at which the channel walls converge, the initial curvature radius, and the shock Mach number, was varied between 40 and 60 degrees, 130 and 190 mm and 1.1 to 1.4, respectively. This enabled the influence of these parameters on various aspects of the evolution of the shock profile to be determined. The variation with time of the pressure-gradient distribution and the maximum pressure gradient behind the shock wave was evaluated. From this, the trajectory angle of the triple points, and the rate at which the reflected shocks develop, was deduced. It was found that when shock waves with larger curvature radii propagate in channels with lower wall angles, the reflected shocks develop at a slower rate, and the triple points follow a steeper trajectory. Consequently, the likelihood of reflected shocks emerging on the shock front, within the duration of the shock propagation, is reduced. This is due to the triple points intersecting the walls, before reflected shocks can fully develop. Similarly, when the shock Mach number is higher, the trajectory angle of the triple points is greater, and they intersect the walls before the reflected shocks can emerge.

Shock waves with curvature radii of 145 mm and 215 mm were produced experimentally using the existing facility. Various tests were conducted for shock waves with Mach numbers ranging from 1.15 - 1.34. The schlieren images obtained from these tests were compared with the results from the corresponding CFD. There was general agreement in terms of the overall profile change that the shock wave experienced. However, a secondary wave, which followed behind the primary shock front, was observed. Furthermore, a quantitative analysis demonstrated that the shock in the experiment was accelerating, whereas in the CFD, the shock Mach number was approximately constant. This was found to be a result of the secondary wave catching up to the primary shock front and reinforcing it. The origin of these secondary waves is the reflection of the shock wave, off the side wall of the propagation chamber, upon exiting the slit. To correct the mismatch in these results, the facility must be modified so that this effect is eliminated.

Contents

List of Figures

List of Tables

List of Symbols

The units of quantities defined by a symbol are indicated in square brackets following the description of the symbol. Quantities with no indicated units may be assumed to be dimensionless.

AB Distance between the points A and B [px].

H Real distance between points A and B [mm].

M Mach number.

P Static pressure [Pa].

R Specific gas constant [J·kg^{-1}·K^{-1}].

S Scale of image.

T Absolute temperature [K].

a Speed of sound [m/s].

t Time [s].

v Fluid velocity [m/s].

x_{0m} Horizontal distance between the midpoint of AB and the datum [mm].

$\overline{v}$ Average velocity of shock wave [m/s].

x, y Real coordinates of a point on an image with respect to the datum [mm].

x_i, y_i Coordinates of a point on an image [px].

x_m, y_m Coordinates of the midpoint of line AB [px].

β Angle of incidence between an oblique shock wave and the oncoming flow [rad].

κ Curvature of shock wave [°].

γ Ratio of specific heats.

θ Flow deflection angle [rad].

θ_1 Approximate shock slope before intersection of curved and straight shock segments [°].

θ_2 Approximate shock slope after intersection of curved and straight shock segments [°].

θ_{TP} Angle of the trajectory of the triple points of the eventual Mach reflection pair to the line of symmetry [°].

θ_t Angle at which image is tilted [rad].

List of Acronyms

CFD Computational Fluid Dynamics.

CFL Courant number.

DiMR direct Mach reflection.

fps frames per second.

InMR inverse Mach reflection.

LSDST Large-Scale Diffraction Shock Tube.

MR Mach reflection.

PPE Personal Protective Equipment.

ROC Rate of Change.

RR regular reflection.

StMR stationary Mach reflection.

1 Introduction

1.1 Background and Motivation

When shock waves with wave fronts concave in the direction of propagation converge, regions of high energy density are produced (Grönig, 1986). Applications for which this energy can be utilized include; the initiation of detonations (Grönig, 1986), the fracturing of kidney and gall bladder stones (Takayama & Saito, 2004), and the production of diamonds (Glass & Sharma, 1976), as cited in (Grönig, 1986). Consequently, various studies involving the production of such waves, and the evaluation of their behaviour, have been undertaken.

Of interest to the current investigation, is the facility designed by Skews, Gray and Paton (2015), with which approximately two-dimensional curved shock waves could be produced, and its subsequent propagation in a converging channel, visualized. Since it was intended that the facility should be capable of producing shock waves of arbitrary profile, the sensitivity of the facility to the shape of the shock wave had to be assessed. This encompassed several numerical and experimental studies, which demonstrated the general propagation behaviour of shock waves with varying compound profiles.

The numerical results of one of the profiles that was investigated, are shown in Figure 1.1. This profile comprises a cylindrical arc placed in-between two straight segments. In this case, the shock wave propagates in-between a pair of straight converging walls, which form the converging channel. Initially, the shape of the shock wave resembles its original profile. This is illustrated in Figure 1.1a. Compression waves emanating behind the central region of the shock wave propagate outwards along the shock front and gradually coalesce. Immediately behind the shock front, this occurs in the region where the cylindrical and straight shock segments meet. This is evident in Figure 1.1b. As a result of the extent to which the compressions have steepened at this instant in time, two discontinuities in the form of kinks can be seen on the shock front.

As the propagation of the shock wave progresses, two secondary shock waves eventually emerge from the kinks. The profile of the resulting shock wave has effectively transitioned

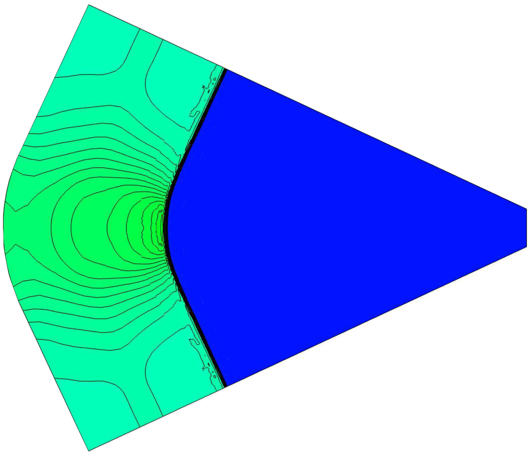

(a) Profile of initial shock wave

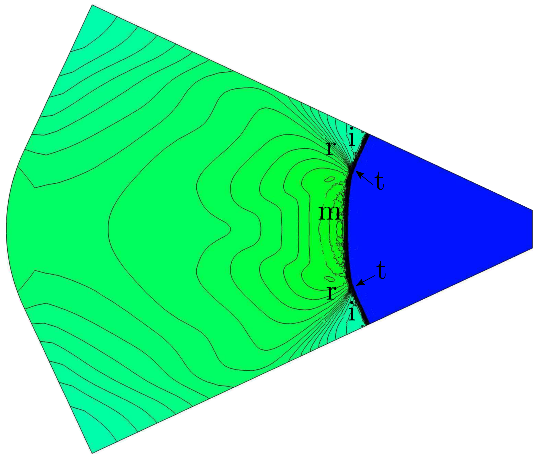

(b) Profile of transitioned shock wave

Figure 1.1: Propagation of a compound shock wave with an initial Mach number of 1.4. The initial shock wave has a cylindrical segment with a radius of 145 mm, and the channel converges at 50 degrees (Adapted from Gray (2014)).

from what was initially one curved shock wave, to a configuration which resembles a symmetrical pair of Mach reflections (Gray, 2014). In this new configuration, the originally straight segments of the shock wave represent the incident wave (i), the cylindrical segment, the Mach stem (m), the secondary shocks, the reflected waves (r), and the kinks, the triple points (t). These features are labelled in Figure 1.1b with the abbreviations shown in parentheses.

An analogous case can be found in the results of Skews, Komljenovic and Sprich (2008) in their investigation into the generation of unsteady flows from rapidly moving boundaries. In this case, the contraction of a parabolic wall at a constant velocity produces a shock wave. As the contraction progresses, the shock wave propagates within the cavity bounded by the parabolic wall. Figure 1.2 depicts the shock wave at distinct times during its motion.

In Figure 1.2a, it is apparent that the shape of the initial shock wave is similar to that of the parabolic wall. However, as the wall is contracted, the shock profile evolves with the development on the shock front of kinks and secondary waves. These transitions are illustrated in Figure 1.2b and Figure 1.2c respectively. At the time shown in Figure 1.2c, the shock wave has a configuration characteristic of a symmetrical pair of Mach reflections.

The transition of a curved shock wave to a Mach reflection has also been observed when a plane shock enters a cylindrical cavity. This is illustrated schematically in Figure 1.3. As the shock propagates into the cavity, successive compression waves are generated on the cavity wall (Figure 1.3a). These compressions converge, curving the shock forwards, until a kink is formed, and eventually coalesce into a short reflected shock, resulting in the Mach reflection depicted in Figure 1.3b (Skews & Kleine, 2007).

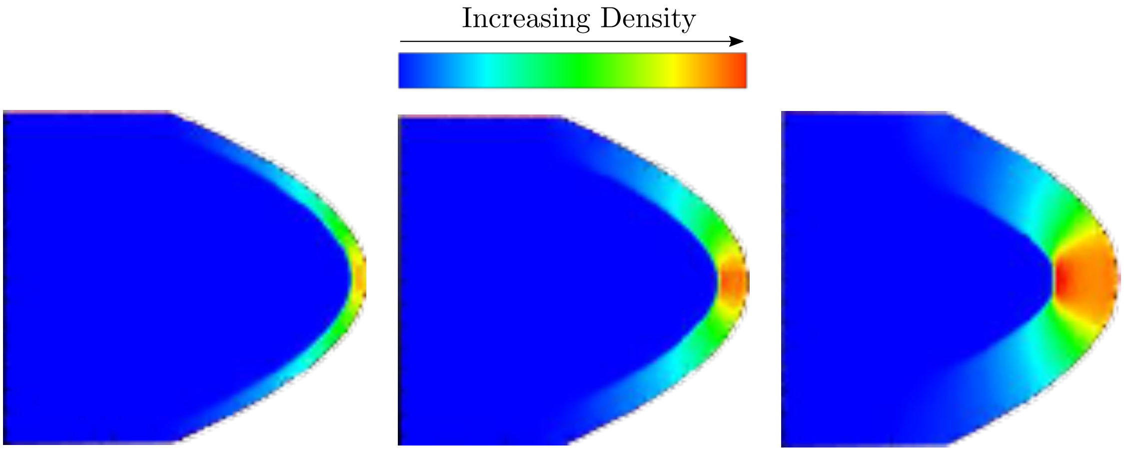

(a) Initial parabolic profile (b) Development of kinks (c) Mach reflection configuration

Figure 1.2: Unsteady flow generated from the contraction of a parabolic wall at Mach 0.5. The wall has cavity depth to aperture ratio of 0.75 (Skews, Komljenovic & Sprich, 2008).

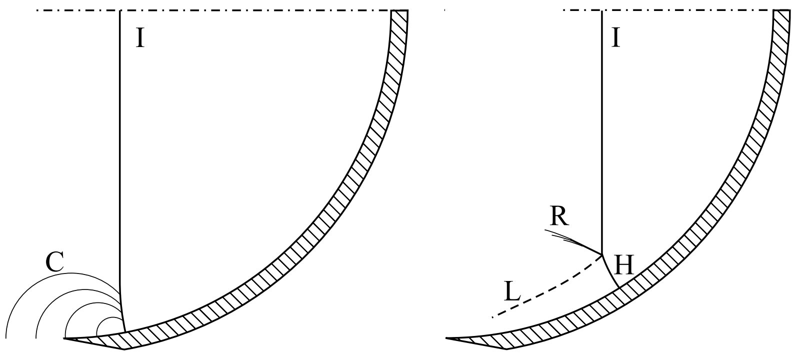

(a) (b)

Figure 1.3: Development of a Mach reflection on a plane shock wave propagating into a cylindrical cavity (Skews & Kleine, 2007). The successive compressions generated on the cavity wall (C), incident shock wave (I), reflected shock (R), Mach stem (H) and shear layer (L) are shown.

In this investigation, the propagation in a converging channel, of shock waves with initial profiles comprising a cylindrical arc placed in-between two straight segments, is explored. An analysis of the physical mechanisms associated with the propagation of these waves contributes fundamental insights to the body of knowledge concerning curved shock waves.

1.2 Literature Review

This section provides a synopsis of the relevant gas dynamics fundamentals, followed by a short survey of some of the previous work regarding the problem of converging cylindrical shock waves. Finally, a description is given of the operating principles of the shock tube, flow visualization techniques, and a concept for the experimental production of arbitrarily shaped shock waves.

1.2.1 Propagation of disturbances in compressible fluids

When a disturbance is present in a compressible fluid, it changes the density of the fluid. This is accomplished by means of a wave, defined as a sound wave. A sound wave is propagated throughout the fluid by collisions of its constituent molecules. As a result, the speed of the sound wave is related to the mean molecular velocity, and for a perfect gas is given by Anderson (2003) as,

$$a = \sqrt{\gamma R T} \tag{1.1}$$

where a is the speed of the sound wave, γ is the ratio of specific heats, R is the specific gas constant, and T is the absolute temperature of the fluid. A sound wave is a weak wave. Thus, it results in only a slight change in the thermodynamic properties of the fluid. A sound wave that increases the fluid's thermodynamic properties can be defined as a compression wave, while one that decreases them, can be defined as an expansion wave.

The velocity of a fluid is related to the speed of a sound wave in the fluid by its Mach number M, given by Anderson (2003) as,

$$M = \frac{v}{a} \tag{1.2}$$

where v is the velocity of the fluid. It follows, that the flow of a fluid can be classified according to its Mach number as:

$$subsonic\ flow \rightarrow M < 1$$
$$supersonic\ flow \rightarrow M > 1$$

1.2.2 Oblique shock waves

Following on from the classification of a flow based on its Mach number, the mechanism by which a supersonic flow adjusts to the presence of a disturbance can be distinguished. Consider the infinitesimally small disturbance in Figure 1.4 moving in a stationary fluid with velocity v (in the frame of reference of the disturbance, it is stationary, and the fluid moves towards it). As it moves, it continually emits sound waves which propagate outwards at the speed of sound a of the fluid. If $v < a$, v is subsonic (Figure 1.4a), and at some time t after the disturbance began its motion, the sound wave emitted at that instant, has travelled a distance at, while the disturbance has only moved a distance vt. Hence, the sound waves are always ahead of the disturbance, and thus, the presence of the disturbance is transmitted everywhere in the fluid, well before the disturbance arrives. However, if $v > a$, v is supersonic (Figure 1.4b). Therefore, the disturbance is always ahead of the sound waves. As a result, successive sound waves overlap, forming a disturbance envelope, defined as a Mach wave (Anderson, 2003).

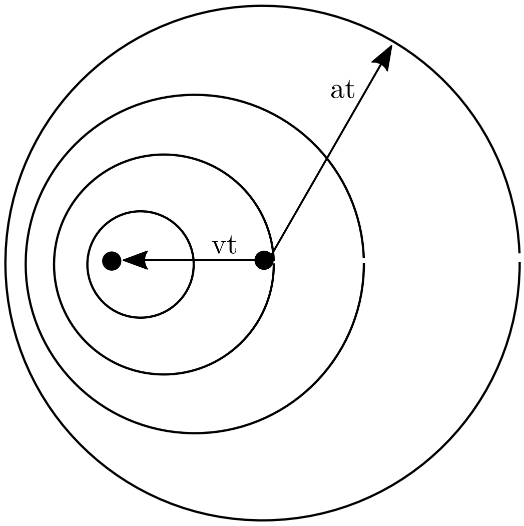

(a) Subsonic flow

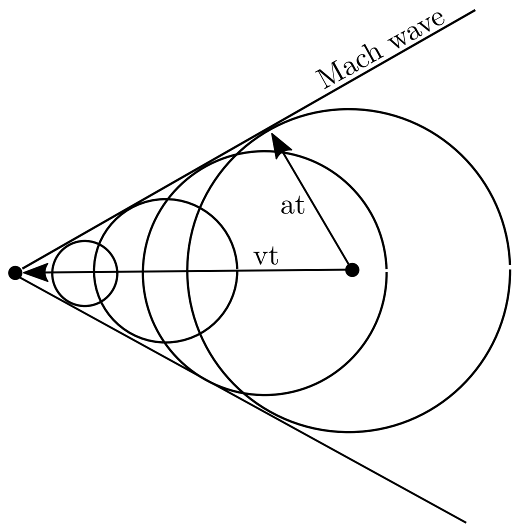

(b) Supersonic flow

Figure 1.4: Propagation of sound waves in a compressible fluid.

Since the disturbance is infinitesimally small, a Mach wave is a weak wave. When the disturbance is stronger, such as the corner shown in Figure 1.5, subsequent sound waves coalesce into an oblique shock wave, at an angle β with respect to the direction of the flow. Across an oblique shock wave, there is a decrease in the Mach number, and an increase in the pressure, density and temperature of the fluid. As illustrated in Figure 1.5, these changes, as well as the change in the direction of the fluid streamlines are discontinuous.

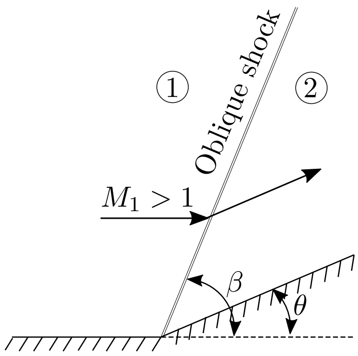

Figure 1.5: Oblique shock wave.

The simplest case of a fluid moving through a stationary normal shock wave (i.e. $\beta = 90$ degrees) can be analysed with the physical laws governing the one-dimensional, and adiabatic (no heat is added to or taken away from the fluid) flow of a fluid. The changes in the thermodynamic properties across the shock wave are thus obtained. This includes the strength of the shock wave $\frac{P_2}{P_1}$, and is given by Anderson (2003) as,

$$\frac{P_2}{P_1} = 1 + \frac{2\gamma}{\gamma+1}(M_1^2 - 1) \tag{1.3}$$

where P is the static pressure, and the subscripts *1* and *2* denote the conditions ahead of, and behind the shock wave respectively. M_1 is determined using the velocity of the fluid relative to the shock wave, and the direction of the flow is perpendicular to the shock. Therefore, by transforming to the frame of reference of the shock wave (i.e. the shock wave is stationary), Equation 1.3 can be applied to the case of a moving shock wave. In addition, by substitution of the normal component of the flow Mach number, Equation 1.3 can be applied to oblique shock waves. This is because the changes across an oblique shock wave are governed by the normal component of the fluid velocity (Anderson, 2003).

The angle θ by which the flow is deflected through the oblique shock is then given by Anderson (2003) as,

$$\tan\theta = 2\cot\beta \left(\frac{M_1^2 \sin^2\beta - 1}{M_1^2(\gamma + \cos 2\beta) + 2} \right) \tag{1.4}$$

Equation 1.4 is known as the θ-β-M relation and is plotted in Figure 1.6 for different values of M_1. Figure 1.6 shows that for a given value of M_1, there is a maximum angle θ_{max} for which a solution for an oblique shock wave exists. Therefore, when a flow encounters a boundary which requires that it be deflected by an angle $\theta > \theta_{max}$, it is not possible for this to occur through a straight oblique shock wave. Instead, the shock wave is curved and detached, as depicted in Figure 1.7.

1.2.3 Shock wave reflection

It was established in the previous section, that shock waves arise in supersonic flows to ensure that any disturbances therein can be negotiated, and the associated boundary conditions satisfied. The situation depicted in Figure 1.5 demonstrated how a supersonic flow handles a single boundary condition.

In many instances, multiple boundary conditions must be met. Figure 1.8 shows one such scenario. A supersonic flow is bounded by an upper and lower wall. When it arrives at point A, it encounters a change in the direction of the lower wall. A straight oblique shock wave is formed, which turns the flow upwards by the angle θ. This enables the flow to continue beyond point A parallel to the lower wall. Behind the shock, the flow is directed into the upper wall, where it must once again be deflected downwards by θ. This is necessary so that

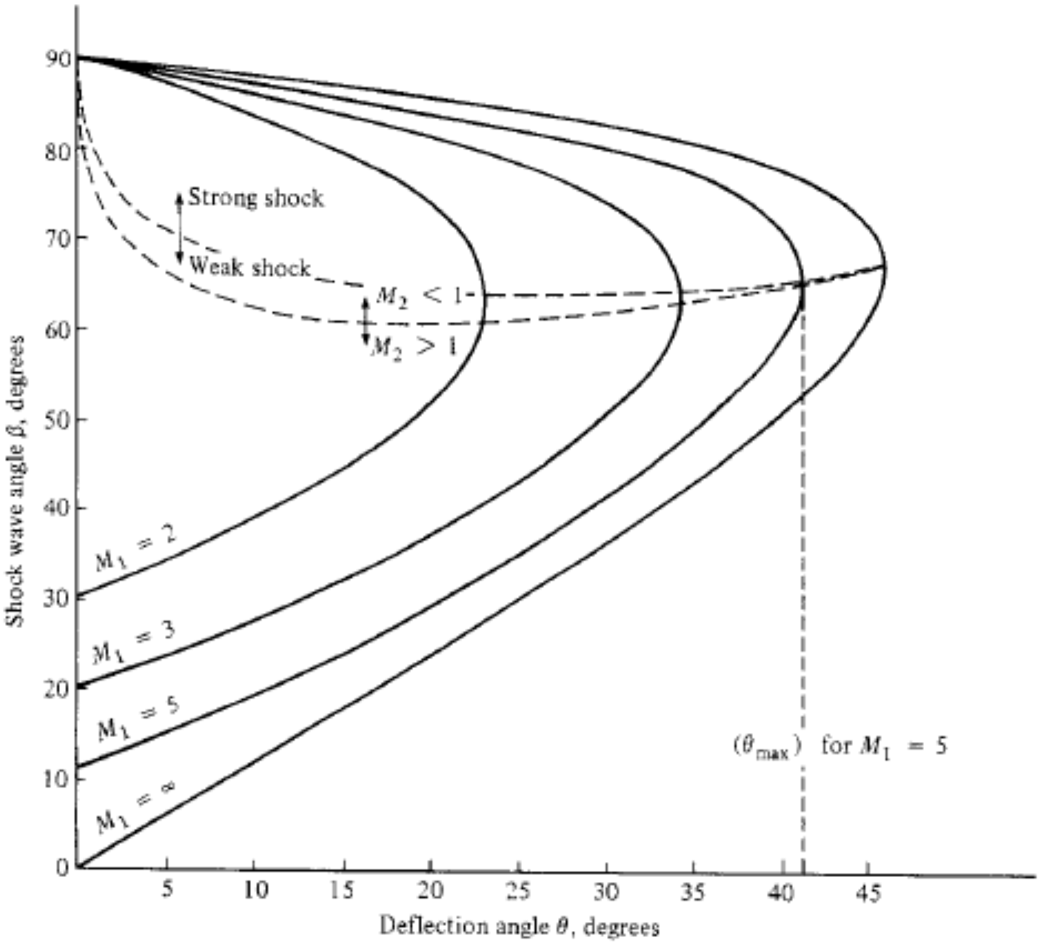

Figure 1.6: The θ-β-M relation (Anderson, 2003).

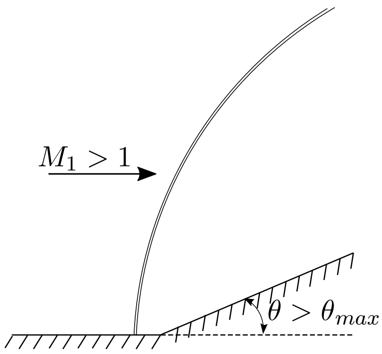

Figure 1.7: Detached shock wave.

it does not impinge on the upper wall. The required deflection occurs across an additional shock wave at point B, where the incident shock intersects the upper wall. This configuration is known as a regular reflection (RR) (Figure 1.8a). It comprises the incident oblique shock wave (i) and the reflected shock wave (r), which meet at the reflection surface.

If the Mach number M_2 of the flow behind the incident oblique shock is such that $\theta > \theta_{max}$ for M_2, an oblique shock is not possible at the upper wall. Instead, a normal shock wave turns the

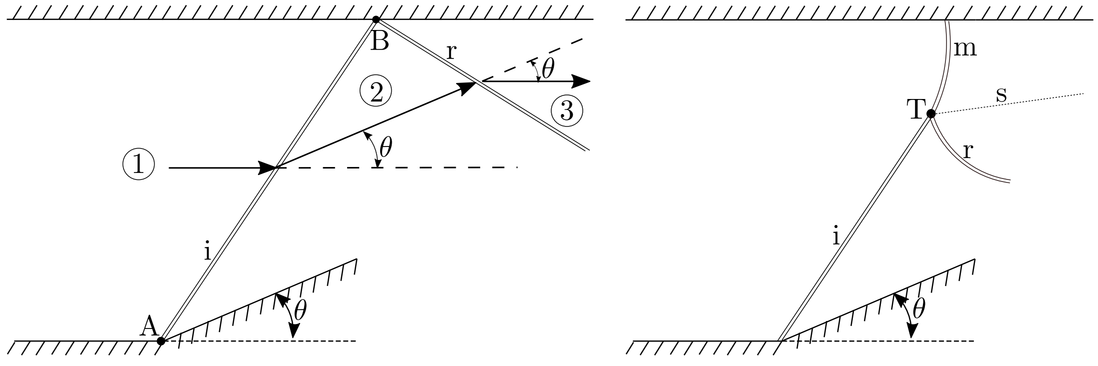

(a) Regular reflection

(b) Mach reflection

Figure 1.8: Oblique shock wave reflection.

flow parallel to the upper wall. Away from the wall, it curves and intersects the incident shock, resulting in a reflected shock which propagates downstream. This configuration is known as a Mach reflection (MR) (Figure 1.8b). It comprises the incident oblique shock wave (i), the reflected shock wave (r), the Mach stem (m) and a slipstream (s). The slipstream separates the regions behind the Mach stem and reflected shock. These four discontinuities meet at the triple point (T). At the triple point, there is a clear discontinuity in the slope between the incident shock wave and the Mach stem (Ben-Dor, 2007).

In an unsteady flow, a MR can be further classified, according to the direction in which the triple point propagates with respect to the reflection surface (Ben-Dor, 2007). When the triple point moves parallel to the reflection surface, the reflection configuration is termed a stationary Mach reflection (StMR) (Figure 1.9a). However, if it moves away or towards the reflection surface, it is termed a direct Mach reflection (DiMR) (Figure 1.9b) and inverse Mach reflection (InMR) (Figure 1.9c), respectively.

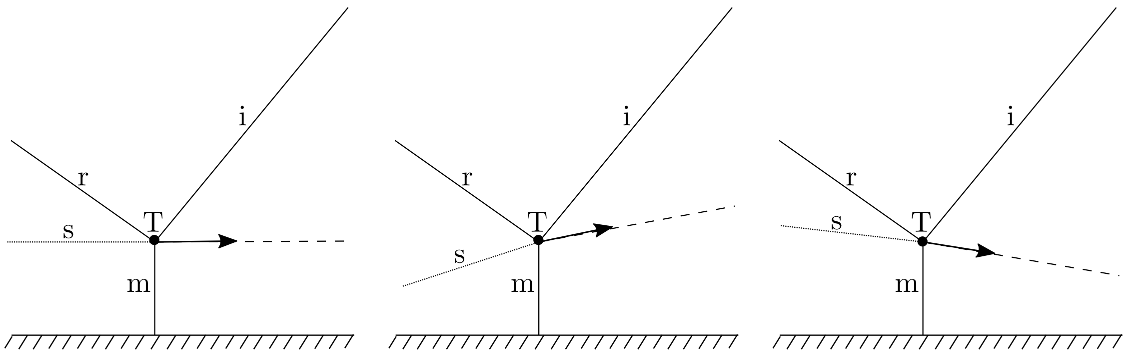

(a) Stationary Mach reflection

(b) Direct Mach reflection

(c) Inverse Mach Reflection

Figure 1.9: Mach reflection configurations in unsteady flows.

It should be noted that there are many types of reflection configurations possible. However, only the general configurations, which are relevant to the current investigation have been described.

1.2.4 Converging cylindrical shock waves

In this section, a brief review of some of the previous investigations into the propagation behaviour of converging cylindrical waves is given.

When a cylindrical shock wave converges, it increases in strength (Payne, 1957). This has been demonstrated experimentally by Perry and Kantrowitz (1951), and numerically by Sod (1977).

The relationship between the strength of a shock wave and a small area change has been described analytically by Chisnell (1957). This relation (typically referred to as the Area-Mach number relation) can be used to obtain the strength of a cylindrical shock wave as it converges. Payne (1957) examined the flow behind these waves, using a numerical technique developed by Lax (1954) as cited in Payne (1957). He found that a converging cylindrical shock wave increases in strength in agreement with the Area-Mach number relation of Chisnell (1957). Additionally, the results of Payne (1957) showed that stronger shocks increase in strength more rapidly than weak shocks.

The propagation of a converging cylindrical shock wave can be evaluated with the general theory of shock-dynamics formulated by Whitham (1957). By using the general theory together with the Area-Mach number relation, and taking into consideration the geometry of the problem, a kinematic equation for the Mach number of the shock can be obtained. From this equation, the trajectory of the shock can be determined.

The formulations of the Area-Mach number relation and the general theory of shock-dynamics are beyond the scope of this investigation. Therefore, they are not included here.

1.2.5 Shock tubes

An important application, which enables shock waves to be studied experimentally, is the shock tube. The basic operating principle of a shock tube is illustrated in Figure 1.10. Essentially, a shock tube is a tube, which has been divided into two chambers by a diaphragm. One chamber (the compression chamber) contains a gas at a high pressure, while the other chamber (the expansion chamber) contains a gas at a low pressure (Figure 1.10a).

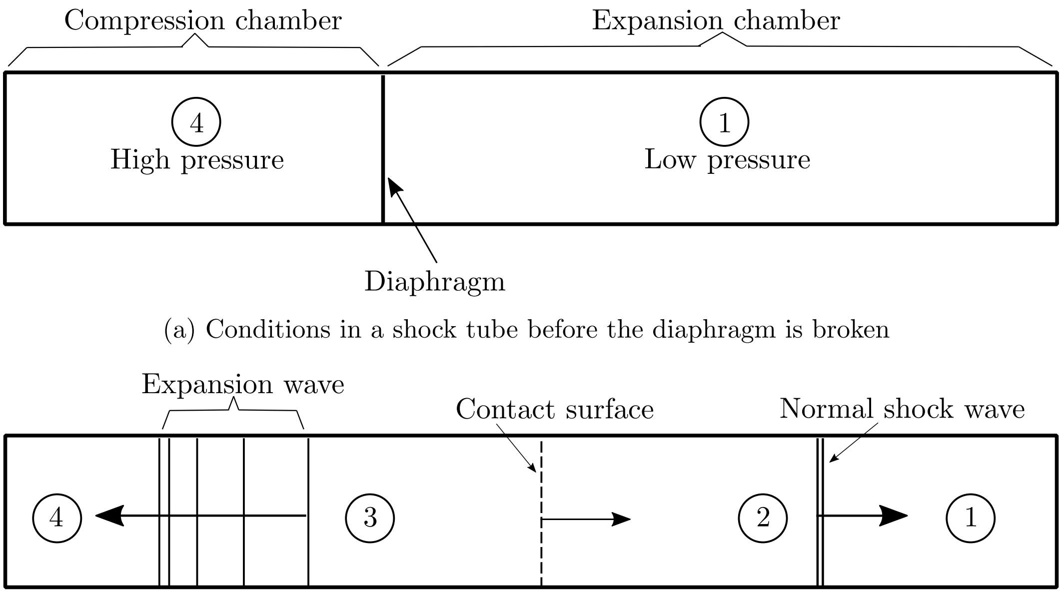

(a) Conditions in a shock tube before the diaphragm is broken

(b) Conditions in a shock tube after the diaphragm is broken

Figure 1.10: Schematic of a shock tube.

A shock wave is generated within the tube by rupturing the diaphragm. This can be achieved either by pricking the diaphragm with a needle, or spontaneously as a result of the pressure difference between the two chambers (Nishida, 2001). When the diaphragm is ruptured, the high-pressure gas which was originally in the compression chamber expands into the expansion chamber. This results in a normal shock wave which propagates down the expansion chamber, and an expansion wave which propagates into the compression chamber (Figure 1.10b). At the interface between the two gases that were initially on either side of the diaphragm, there is a discontinuity in the density and temperature of the gas. This discontinuity is known as the contact surface. The contact surface follows behind the shock wave at the velocity of the gas behind the shock wave.

The strength $\frac{P_2}{P_1}$ of the shock wave generated by the rupturing of the diaphragm is governed by the pressure ratio $\frac{P_4}{P_1}$ across the diaphragm before it is ruptured. This is given by Liepmann and Roshko (2001) as,

$$\frac{P_4}{P_1} = \frac{P_2}{P_1}\left(1 - \frac{(\gamma_4 - 1)\left(\frac{a_1}{a_4}\right)\left(\frac{P_2}{P_1} - 1\right)}{\sqrt{2\gamma_1}\sqrt{2\gamma_1 + (\gamma_1 + 1)\left(\frac{P_2}{P_1} - 1\right)}}\right)^{\frac{-2\gamma_4}{\gamma_4 - 1}} \tag{1.5}$$

where the subscripts *1*, *4*, and *2* correspond to the conditions in the expansion chamber, compression chamber, and behind the normal shock wave respectively. Equation 1.5 can be used to determine the diaphragm pressure ratio necessary to produce a normal shock wave with a given strength.

1.2.6 Flow visualisation

The speed of light in a medium is dependent on the density of the medium. Therefore, when light traverses an area of varying density, it is displaced, deflected, retarded or accelerated (Kleine, 2001). Since flows containing shock waves are accompanied by corresponding density gradients, utilizing this principle provides a means by which such flows can be visualized. A picture of the flow is obtained by recording the changes an array of light passing through these gradients undergoes. The various flow visualization techniques that are generally used are distinguished by the specific change (displacement, deflection, or acceleration) that is recorded.

In this investigation, the schlieren method is employed. A schlieren image displays the deflection angle (which corresponds to the first derivative of the density in the area of varying density) that the light experiences (Settles, 2001). Figure 1.11 depicts a simple schlieren system to illustrate the basic operation of this technique. It comprises a point light source, two lenses, a screen on which the changes can be recorded, and a knife edge positioned at the focus of the second lens. Light emanating from the point source is collimated by the first lens and thus, passes through the test area as parallel rays. The second lens refocuses the light to an image of a point source from where it proceeds to the screen upon which a real inverted image of the test area is formed (Settles, 2001).

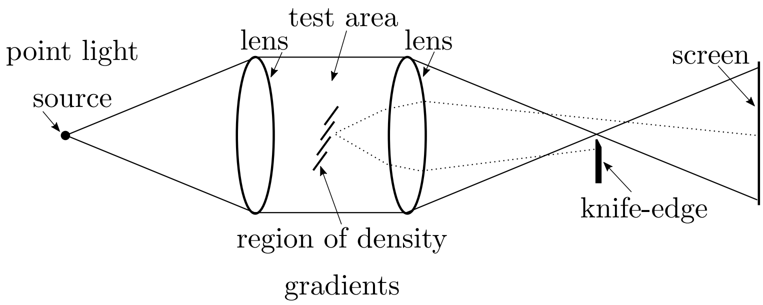

Figure 1.11: Layout of a simple schlieren system.

The rays drawn in Figure 1.11 demonstrate what happens to the light when it encounters density gradients in the test area. As the light passes through these gradients, it is refracted. Rays that are bent upwards brighten their corresponding point on the screen. However, if a ray is deflected downwards, it is blocked by the knife edge and its corresponding point on the screen is darker. The resulting pattern of brighter and darker fringes represents a picture of the flow. Only deflections perpendicular to the knife edge are blocked. Hence, a schlieren image displays the density gradients in one direction.

The most common implementation of the schlieren technique is the Z-type configuration illustrated in Figure 1.12. In this configuration, a lens condenses the beam from the light source (such as a lamp) to a point source at the first slit. Instead of lenses, two parabolic mirrors are used, and an additional lens is positioned after the knife edge. This lens enables the size of the image formed at the screen (which in practise would be a camera) to be controlled. The coma produced by tilting the mirrors off their optical axis is eliminated by ensuring that both mirrors are tilted by the same angle, but in opposite directions. This results in a configuration which resembles a z-shape.

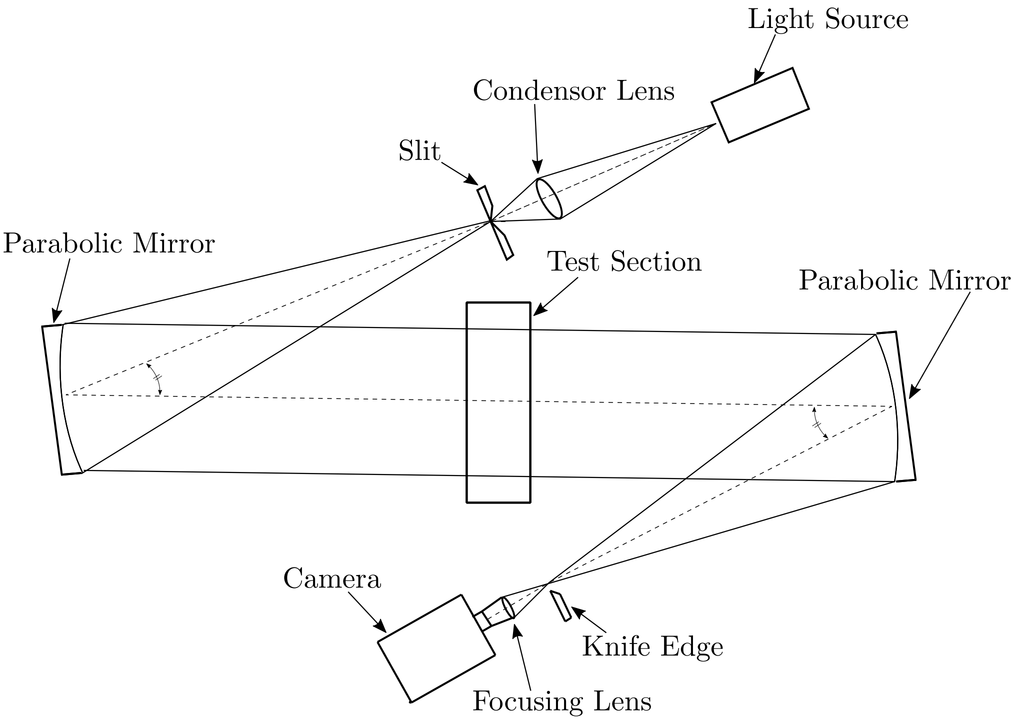

Figure 1.12: Schematic of a Z-Type schlieren configuration.

1.2.7 Experimental production of shock waves of arbitrary profile

In this section, the concept from which the facility mentioned in section 1.1 was derived, is described. This concept is unique in that the shape of the shock wave generated, as well as the channel into which it propagates, can be arbitrarily defined. The experiments of Skews et al. (2015) validated this concept, by demonstrating that the facility could produce high quality shock waves, with a profile that closely conformed to the required shock shape.

This concept is illustrated in Figure 1.13 for the propagation of a cylindrical shock wave segment in a converging channel. The basic principle is that when a planar shock wave passes through a slit of some given profile, the shock wave assumes this profile. The required profile is machined into a flange in which it forms a narrow slit. This flange is attached to the end of a conventional shock tube. Upon exiting the slit, the shock wave enters the propagation channel, which is positioned perpendicular to the main shock tube axis (Skews et al., 2015). The shape of the channel is defined by its top and bottom surfaces, while the rear internal surface must match the slit profile. The width of the slit and channel must be narrow, so that an approximately two-dimensional wave is generated.

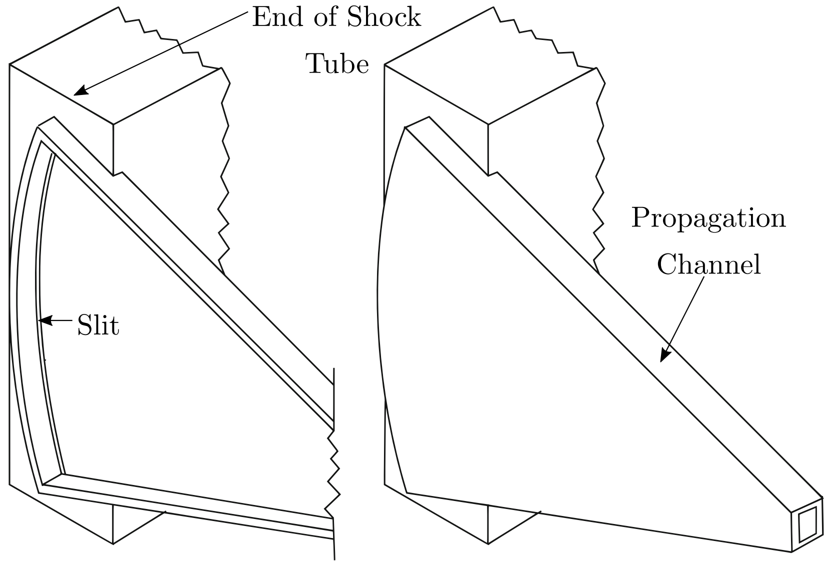

Figure 1.13: Concept for the experimental production of converging cylindrical shock waves (Adapted from Skews, Gray and Paton (2015)).

2 Objectives

The primary aim of this investigation is to evaluate the physical mechanisms associated with the propagation of shock waves, of varying curvature, in a converging channel. This involves the following objectives:

- Carry out numerical studies for various initial shock profiles and converging channels, and;
  - Describe the physical mechanism responsible for the development of reflected shocks on an initially smooth and continuous shock front.
  - Investigate the effect of the initial curvature radius, shock Mach number and wall convergence angle on the characteristic aspects of the shock propagation.
- Conduct corresponding experiments to;
  - Validate the evolution of the shape of shock waves with initially smooth, continuous profiles.
  - Compare the behaviour of the shock waves produced in the experiments with those in the numerical simulations.

3 Experimental Method

The experimental component of this investigation was conducted using the facilities in the North West Engineering Laboratory at the University of the Witwatersrand. This chapter provides details of the facilities and instrumentation that were used.

3.1 Shock tube

Planar shock waves were generated using the Large-Scale Diffraction Shock Tube (LSDST) rendered in Figure 3.1. It comprises a cylindrical driver vessel, sealed at its ends with circular flanges, and a rectangular driven section (expansion chamber) with its ends open. At the interface with the driven section, there is a rectangular cavity in the driver flange with dimensions matching those of the internal cross section of the driven section. A plastic diaphragm is fitted across this flange. The driver vessel has been filled with D-shaped inserts (Figure 3.2) fabricated from wooden planks, in order to reduce its capacity, and thus, the time required to pressurize the driver. A 100 mm wide gap, conforming with the width of the driven section is maintained between the inserts. The driver is mounted on rails, allowing it to be slid open (away from the driven section) and closed (joining it with the driven section) when changing the diaphragm. Sixteen M32 bolts are used to secure the interface between the driver and driven sections. The specifications of the LSDST are given in Table 3.1.

3.2 Apparatus

Shock waves with the required profile were achieved by attaching the facility designed by Skews et al. (2015) to the exit of the driven section of the LSDST and allowing the planar shock wave generated by the tube to pass through the slit in the facility. The facility consists of a series of three plates arranged in layers (Figure 3.3). The first layer is positioned at the interface between the shock tube and the facility. It comprises two smaller plates; a short outer plate, and a profile plate in which a slit of the required shock profile has been machined.

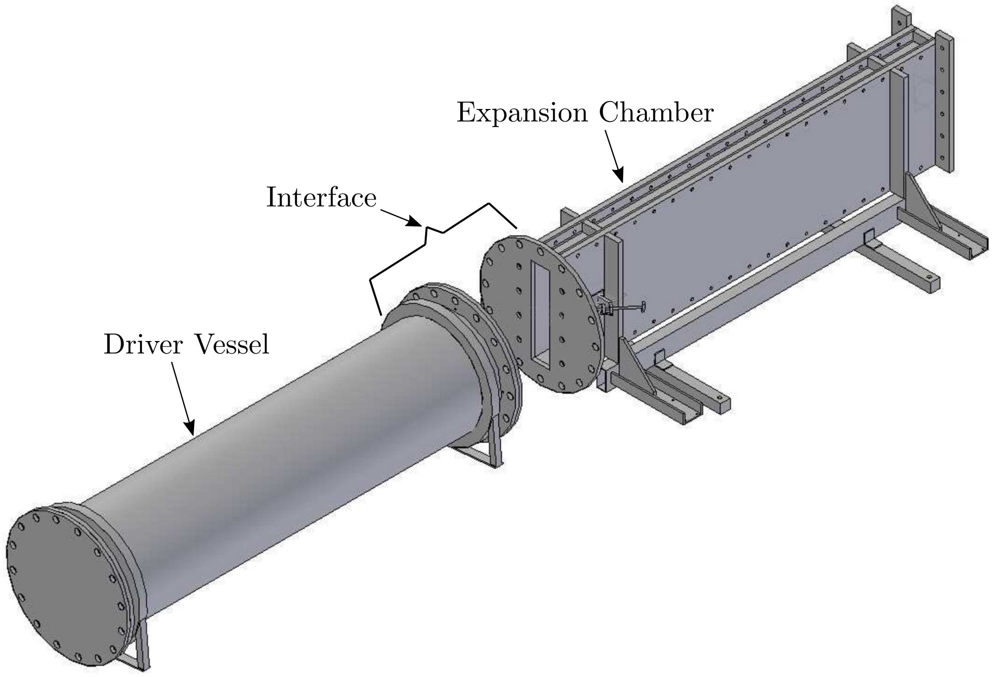

Figure 3.1: Rendering of the interface between the driver and driven sections of the LSDST (Adapted from Gray (2014)).

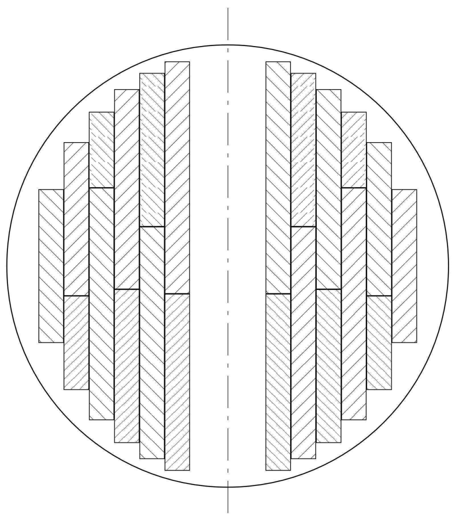

Figure 3.2: Internal cross section of the driver vessel of the LSDST (Gray, 2014).

This is followed by a propagation plate with converging walls (which forms the propagation chamber), and a large outer plate.

Two glass windows, 354 mm in diameter, are embedded in the outer plates so that the flow within the propagation plate can be visualised. On the outer face of the plates, a steel frame clamps the windows in place (Gray, 2014). This leaves an effective viewing area, 330 mm in diameter.

Table 3.1: Specifications of the LSDST

Driver Vessel			Expansion Chamber		
Physical Property	**Unit**	**Specification**	**Physical Property**	**Unit**	**Specification**
Gas	-	Air	Gas	-	Air
Maximum Pressure	bar	10	-	-	-
Length	m	2	Length	m	6
Diameter	mm	450	Internal Cross Section (height x width)	mm	450 x 100

A groove, 3 mm deep and 5 mm wide, has been cut into the side of the profile plate. A 4 mm O-ring cord is inserted in this groove, ensuring that that there is an adequate seal between the profile and short outer plate. Additionally, both faces of the propagation plate, as well as the flange at the exit of the shock tube, is lined with paper gasket, 0.4 mm thick, to prevent air leaks through these interfaces when a test is conducted.

In a later study (Ndebele, 2017), the propagation plate was modified by dividing it into three component plates; a side, top and bottom propagation plate (Figure 3.4). The interface between the component plates is a step, 7.5 mm deep, which has been cut into the top and bottom of the side propagation plate, and at one end of both the top and bottom propagation plates. Six M6 bolts are used to fasten the top and bottom plates to the side plate at their corresponding interfaces. The inserts shown in Figure 3.4 were specific to Ndebele's (2017) investigation and were not needed for the current experiments.

Seven M14 bolts are used to secure the plates together, while another seven M14 bolts fix the facility to the shock tube exit. Tabs at the top of each plate allow a hook from an overhead gantry to be connected to the facility. This facilitates moving the facility when attaching or disconnecting it from the shock tube. Engineering drawings for this facility can be found in Gray (2014) and Ndebele (2017). The general procedure for assembling and disassembling the facility is detailed in Appendix A.

In this investigation, shock waves with various initial profiles were tested. This required a distinct profile and propagation plate to those used in the previous studies with this facility. Although the original facility was designed to produce a cylindrical shock segment with a radius of 450 mm, the modular nature of the facility allows any of the component plates to be substituted with those required for a particular study. Thus, it was only necessary to manufacture the profile and side propagation plates corresponding to the shock wave profiles

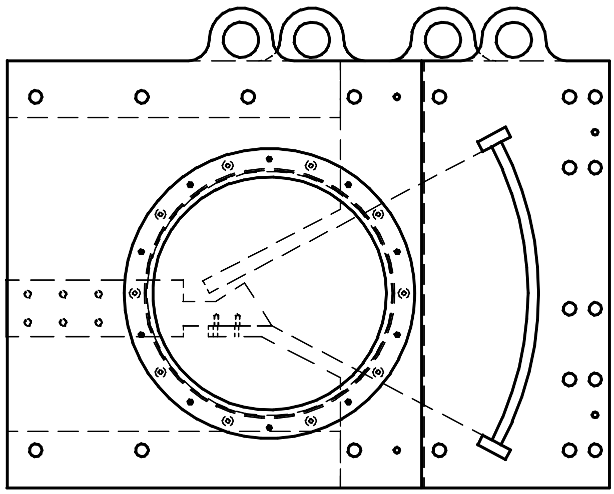

(a) View of assembled apparatus

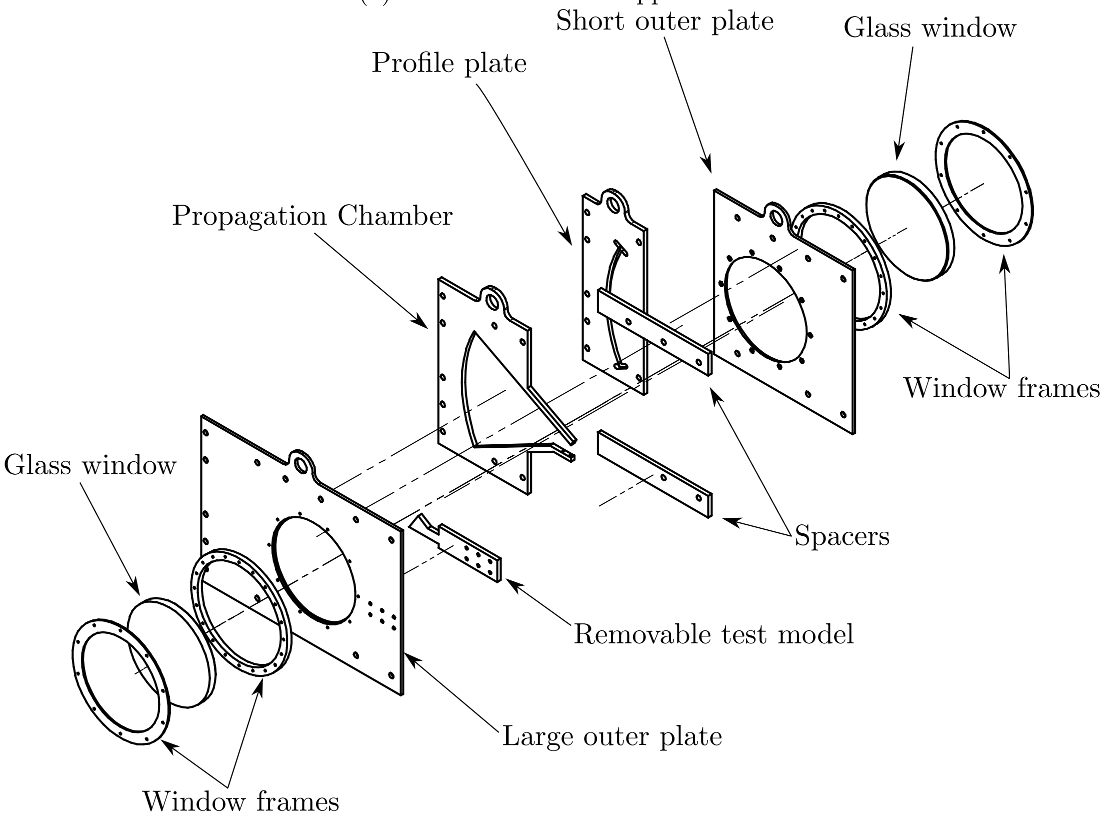

(b) Exploded view of apparatus

Figure 3.3: Apparatus used for the generation of shock waves with arbitrarily defined profiles (Gray, 2014).

that were going to be tested. Engineering drawings for these can be found in Appendix B. Details of the initial shock wave profiles that were selected for the experimental tests are discussed in section 6.1.

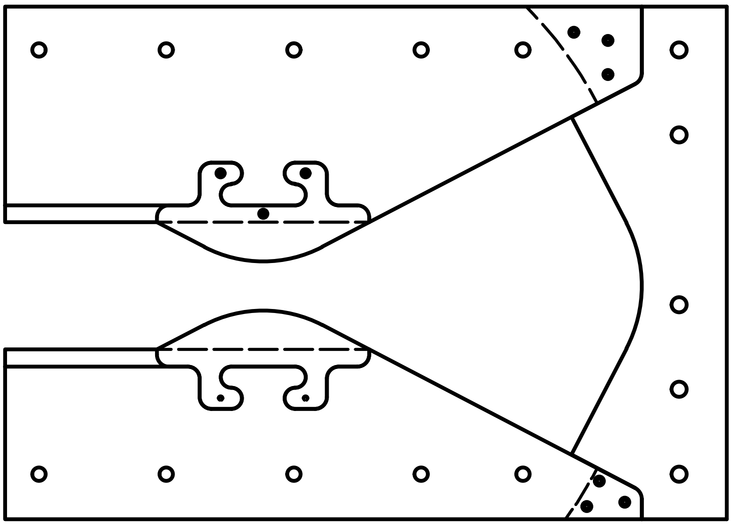

(a) Assembly view of modified propagation plate

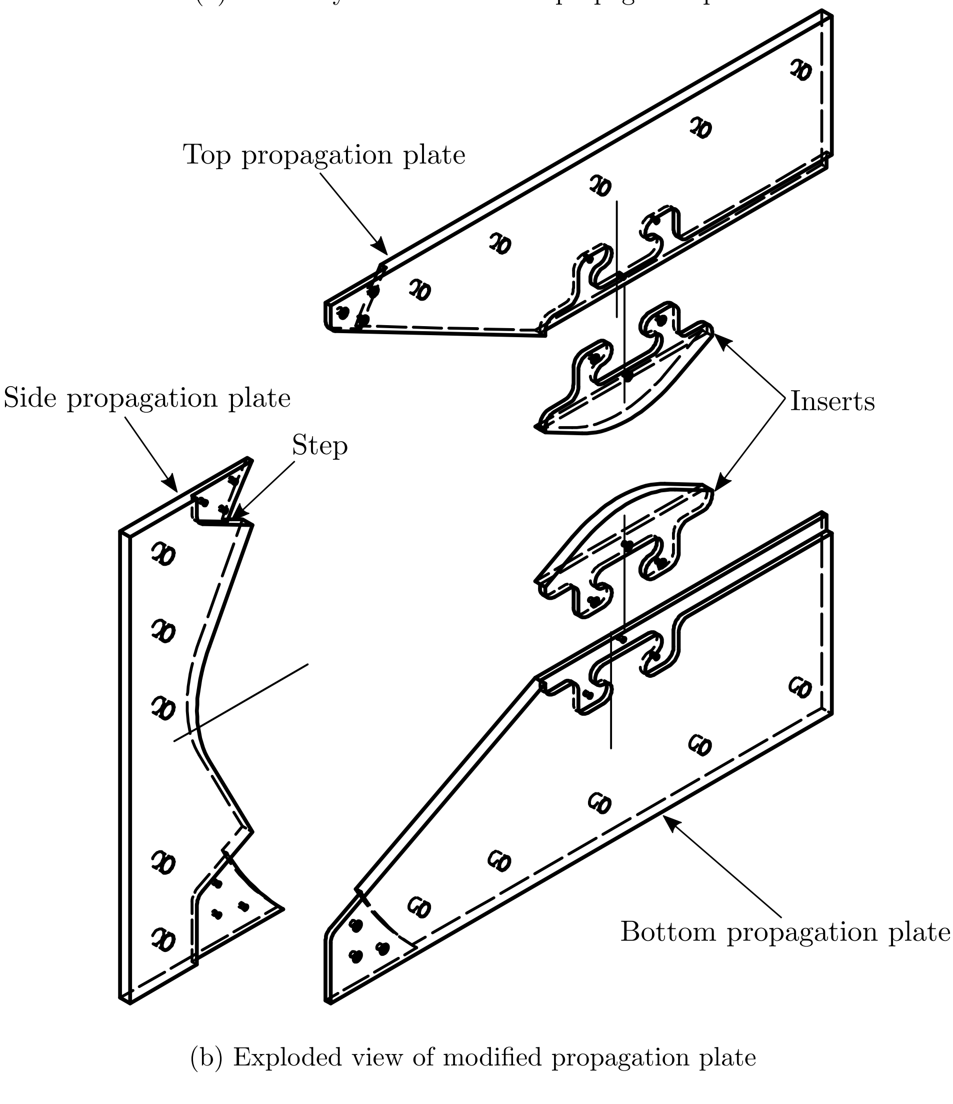

(b) Exploded view of modified propagation plate

Figure 3.4: Modified propagation plate

3.3 Flow visualisation

The propagation of the shock wave in-between the converging walls of the propagation chamber was captured using the schlieren flow visualization technique, in the Z-type configuration depicted in Figure 1.12 (in section 1.2.6). The optical equipment used in this system included:

- **Light source** - The Megaray Lab-Light MRLL17 was used in continuous mode. It contains a short-arc xenon lamp.
- **Condensing lens** - with a focal length of 85 mm.
- **Slit** - an 0.5 mm thick aluminium plate with a pin-sized hole.
- **Two parabolic mirrors** - with a diameter of 406 mm and respective focal lengths of 1836 mm and 1841 mm.
- **Knife edge** - comprising a razor blade mounted on an adjustable stand.
- **Focusing lens** - with a focal length of 75 mm.
- **Camera** - Photron FASTCAM SA5 high-speed camera. High speed images were obtained at a frame rate of 42 000 fps with a shutter speed of 1 μs.

The optics were mounted on two rails which were positioned at approximately fifteen degrees with respect to the test section. The beam from the finite light source was passed through a pin-sized hole in a 0.5 mm thick aluminium plate. An approximate point source (as required by the schlieren technique) was thus achieved. Pieces of black cardboard, extending from the light source to this plate, were placed around the edges of these components. This ensures that no light leaks around the edges so that the only light passing through the schlieren system emanates from the manufactured point source. The knife edge was oriented horizontally, and its height adjusted to achieve the required sensitivity. A shutter speed of 1 μs was required to minimize motion blur, and the choice of frame rate was a compromise between the corresponding resolution and the quantity of images that could be obtained. Rotating the camera ninety degrees allowed the entire region of interest to be captured at a higher frame rate. A frame rate of 42 000 frames per second (fps) was the maximum at which this was possible.

3.4 Instrumentation

The layout of the facility and its auxiliary instrumentation is illustrated schematically in Figure 3.5

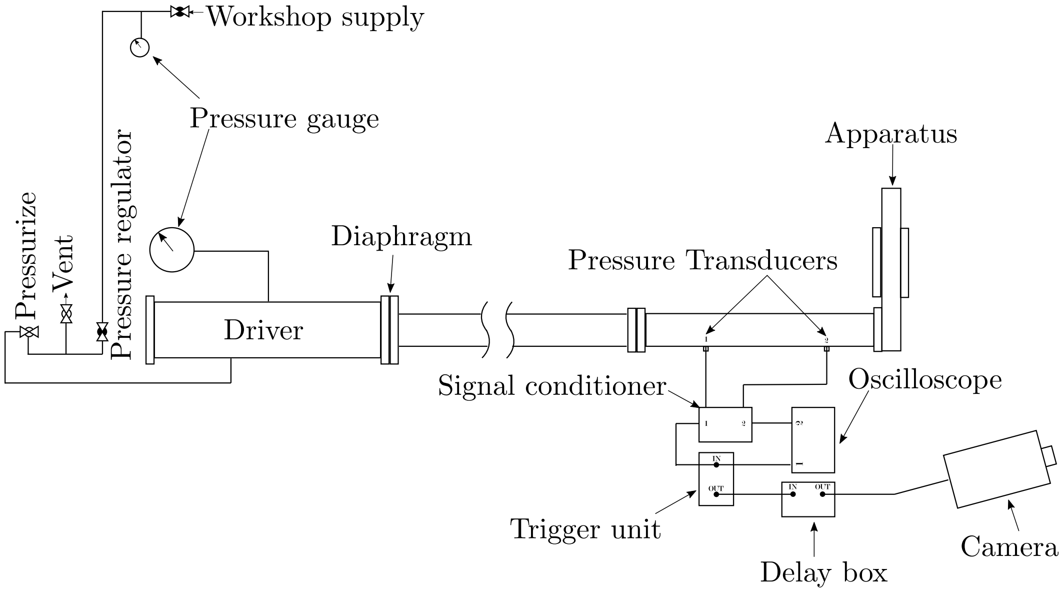

Figure 3.5: Layout of the facility and auxiliary instrumentation

Air is supplied from the laboratory reservoir to pressurize the driver vessel. The laboratory supply is regulated with a globe valve, and a pressure gauge, located nearby, measures the pressure at which the air is supplied. A control panel, located on the wall behind the shock tube, contains a globe valve, a pair of ball valves and a pressure gauge. The globe valve controls the rate at which the driver is pressurized, the ball valves are used to either pressurize or vent the driver, and the pressure gauge allows the pressure inside the driver to be measured.

In all the experiments that were conducted, the diaphragm was ruptured spontaneously. The Mach number of the shock wave generated was varied by using diaphragms with different thicknesses. Diaphragms with thicknesses of 25 μm, 50 μm and 100 μm were available. This produced shock waves with Mach numbers that ranged between 1.14 - 1.37.

Two pressure transducers, embedded in the walls of the driven section of the tube, detect the shock wave as it passes and send a signal to an oscilloscope. The interval of time over which the shock wave propagates in-between the two transducers is then measured with the oscilloscope, enabling the velocity of the shock wave to be calculated.

The signal from one of the pressure transducers is split at a trigger unit, so that it can also be sent via a programmable time delay unit to trigger the high-speed camera. The time delay is required so that the camera is triggered when the shock wave enters the facility's viewing window. The time delay is specified prior to conducting a given test and is based on the requirements of that test. For the current experiments, a delay of 300 μs was set. This was based on the highest expected shock Mach number and for convenience, it was used for all tests.

The serial numbers of the optical equipment and auxiliary instrumentation that were used are given in Appendix C. The operating procedure of the LSDST can be found in Appendix D.

4 Numerical Method

The propagation of curved shock waves in a converging channel was analysed with CFD simulations for a variety of channels, initial shock wave profiles and Mach numbers. Various software was available for this purpose. The geometry of the computational domain was constructed with Autodesk Inventor, while ANSYS' Meshing and Fluent packages were used to generate the mesh and solve the governing equations of the flow.

Post-processing of the subsequent results was performed with Tecplot 360, and scripts were written in MATLAB to analyse and generate plots of the relevant data. This chapter details how the flow was modelled and solved, and how the data required for analysis was obtained from the simulation. The descriptions that follow are typical of any of the cases for which simulations were executed.

4.1 Computational Fluid Dynamics

4.1.1 Geometry

The primary consideration when constructing the geometry of the computational domain was correspondence with the experiment. Therefore, the edges defining the computational domain are determined by the boundaries of the facility's propagation chamber. Due to the inherent symmetry of the geometry, it was only necessary to compute half the domain. A typical geometry is shown in Figure 4.1.

The left boundary was defined by the profile of the initial shock wave, which as mentioned in section 1.1, comprises a cylindrical arc and a straight segment. The straight segment must be tangent to the cylindrical segment so that the composite profile is smooth and continuous. It must also be normal to the walls of the propagation chamber. This constraint is in accordance with the experimental facility and was required there to ensure the integrity of the shape of the shock waves in the experiments (Gray, 2014). The length of the straight segment is thus

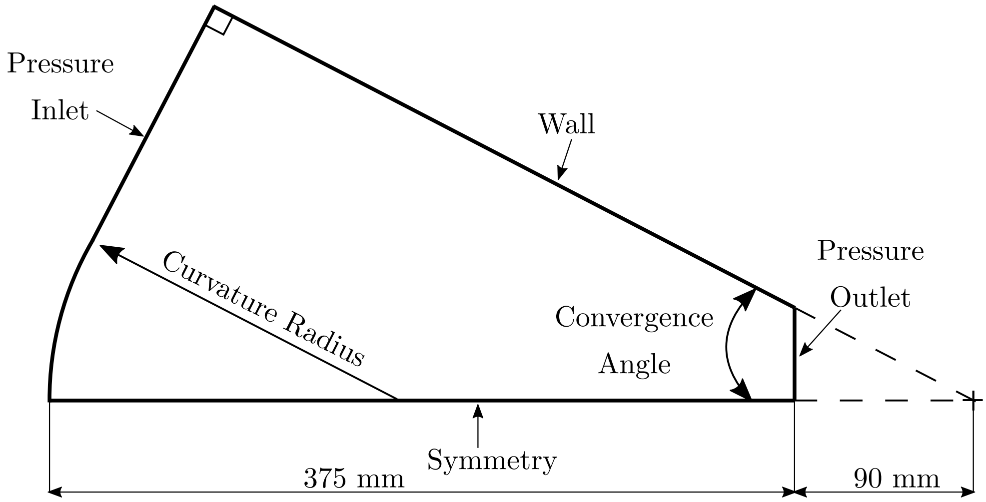

Figure 4.1: Typical geometry of computational domain.

determined by the length required to satisfy these conditions. The distance between the left boundary (which corresponds to the back face of the slit in the experimental facility) and the point at which the walls of the chamber converge was specified to match the experimental facility. The length of the computational domain was truncated, since beyond this point in the experiments, the flow is no longer of interest (this was typically true in the numerical simulations as well). The radius of the cylindrical segment (referred to as the curvature radius of the shock wave) and the angle at which the chamber walls converge (referred to as the convergence angle of the walls) was varied in the different simulations.

4.1.2 Mesh

To ensure that the curved surface at the inlet of the domain (Figure 4.1) was accurately represented, the initial mesh was generated based on curvature, with a curvature normal angle of 5 degrees, and a maximum cell size of 2 mm. It was also necessary to utilize adaptive mesh refinement during the simulations so that the shock wave was sufficiently resolved. Cells were marked for either refining or coarsening based on normalised gradients of pressure, density, temperature and velocity magnitude. Cells were refined up to four times if the normalised gradients were greater than 3% of the maximum and coarsened if the normalised gradients were less than 1.5% of the maximum. A typical initial and adapted mesh is shown in Figure 4.2.

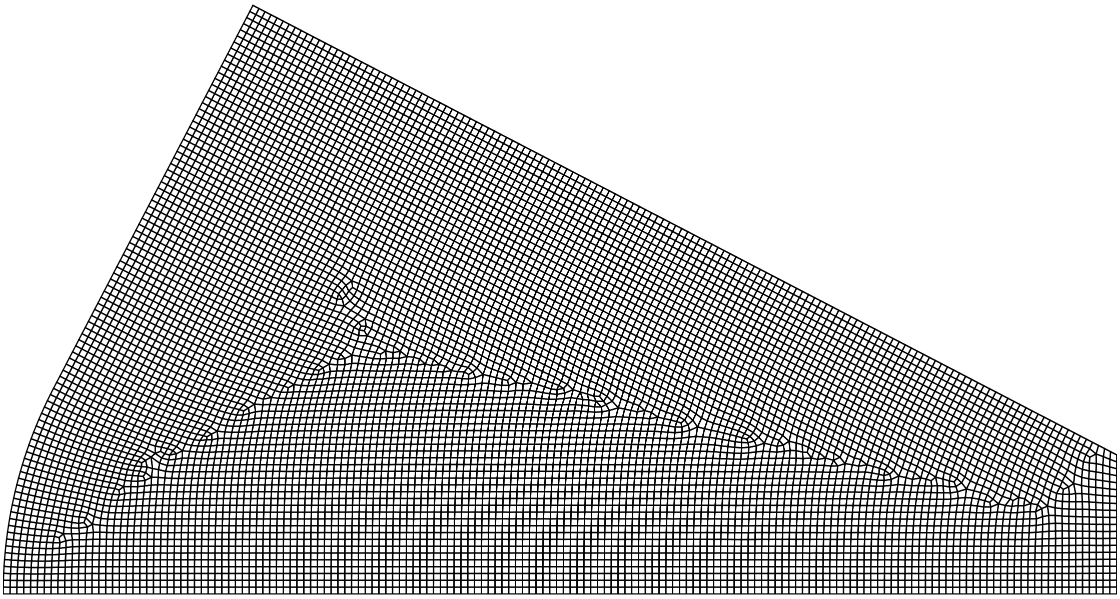

(a) Initial mesh

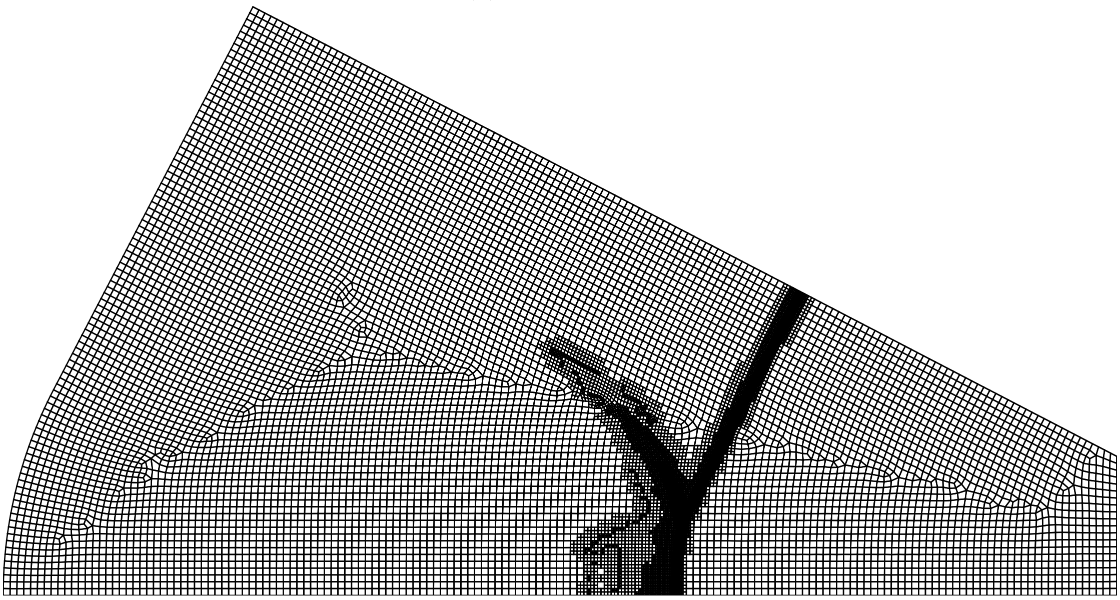

(b) Adapted mesh

Figure 4.2: Typical meshes (Cells with pale outlines are a result of the scaling down of the image)

4.1.3 Solver

The flow field under investigation contained shock waves (and hence, concerned a high-speed compressible flow), therefore, it was analysed using ANSYS Fluent's density-based solver. The speed at which the solution converged, the memory requirements, as well as, solution accuracy, were considered when specifying the various settings of the density-based solver. The ideal settings were those which resulted in the fastest solution convergence and required the least memory, while simultaneously maintaining sufficient accuracy. As a result, the explicit formulation of the density-based solver was selected, with the Roe flux-difference splitting (Roe-FDS) and Least Squares Cell Based Spatial Discretization schemes. The first order implicit transient formulation was used, and the default Courant number (CFL) of 1 was retained. These settings provided the optimal combination of the afore-mentioned criteria. The size of the time step was determined so that the shock would be resolved sufficiently. A time step of 1 x 10^{-7} s was found to be appropriate.

The air inside the domain was modelled as an inviscid, ideal gas and initialized with atmospheric conditions (pressure of 101325 Pa and temperature of 300 K). The types of physical and inertial conditions that were imposed on the boundaries of the domain are shown in Figure 4.1. A shock wave was simulated at the pressure inlet boundary by specifying the conditions (static pressure, total pressure, total temperature) behind the shock wave of the desired strength.

4.2 Extracting the Properties behind the Shock Wave

In order to provide a physical description of the shock propagation, it was necessary to obtain a temporal profile of the properties (specifically the pressure) immediately behind the shock wave. This required the nodes in the interior of the domain that represented the shock wave to be identified, so that the corresponding properties at these nodes could be exported into a suitable file for further analysis in MATLAB.

The post-processing suite available in ANSYS Fluent allows cells with constant values of a specified variable to be distinguished and grouped together as a distinct surface. Since the shock wave was captured during the simulations with adaptive mesh refinement, it was possible to generate an iso-surface representing the shock wave based on constant values of adaption space gradient. At each instant in time for which an analysis was required, the iso-value corresponding to the shock wave was selected interactively. As the iso-value was varied, an instantaneous preview of the corresponding iso-surface was created. Superimposing this preview on a contour of the entire domain enabled an iso-value that accurately captured the shock wave to be determined.

Figure 4.3 demonstrates an example preview for one of the numerical simulations that was carried out. A preview of the surface corresponding to an iso-value of 0.05 is shown in Figure 4.3a. In Figure 4.3b, this is superimposed on a pressure contour of the domain, where it can be ascertained, that this specific iso-value does indeed correspond to the shock wave. Once the shock wave was successfully detected, the properties (particularly the static pressure and x and y coordinates) at the iso-surface's constituent nodes were exported to an ASCII file. This file was then imported into MATLAB for further processing.

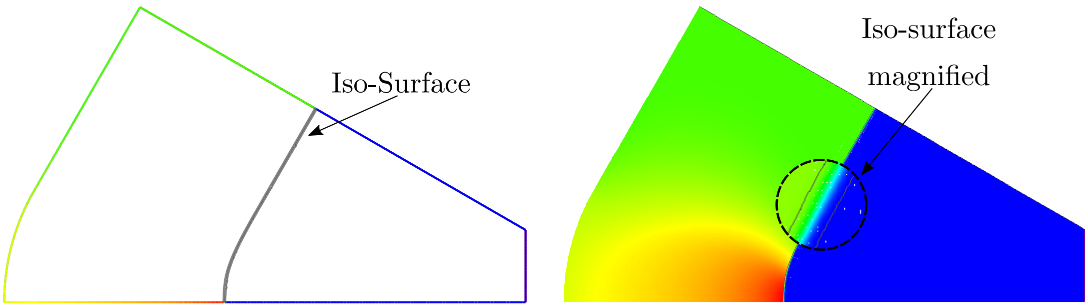

(a) Preview of the iso-surface corresponding to an isovalue of 0.05

(b) Iso-surface superimposed on pressure contour

Figure 4.3: Selection of a suitable iso-value at 300 μs

Since the shock is detected based on the property gradients across it, the iso-surface that is generated comprises two lines of nodes corresponding to the fluid immediately behind and in front of the shock wave. This is evident in the magnified view of the iso-surface in Figure 4.3b. In order to evaluate the temporal variation of the properties of the fluid immediately behind the shock wave, it is the information at the corresponding line of nodes that is pertinent. As the fluid in front of the shock wave is undisturbed, the pressure at the corresponding line of nodes is atmospheric. Using this fact, the data at the line of nodes representing the fluid immediately behind the shock wave was distinguished for use in the subsequent analyses, by examining whether the static pressure at these nodes was significantly greater than atmospheric.

5 Numerical Results

Numerical simulations were undertaken for the propagation of shock waves, with various initial profiles, in a converging channel. In these simulations, the angle at which the channel walls converged (Wall Convergence Angle), and the initial Mach number and curvature radius of the shock wave, ranged from 40 - 60 degrees, 1.1 - 1.4 and 130 -190 mm, respectively. A summary of the simulations that were performed is given in Table 5.1.

Table 5.1: Summary of numerical simulations for a curved shock wave propagating in a converging channel

Wall Convergence Angle [°]	**Curvature Radius [mm]**	**Mach Number**
40	130	1.1, 1.2, 1.3, 1.4
40	160	1.1, 1.2, 1.3, 1.4
40	190	1.1, 1.2, 1.3, 1.4
45	130	1.1, 1.2, 1.3, 1.4
45	160	1.1, 1.2, 1.3, 1.4
45	190	1.1, 1.2, 1.3, 1.4
50	130	1.1, 1.2, 1.3, 1.4
50	160	1.1, 1.2, 1.3, 1.4
50	190	1.1, 1.2, 1.3, 1.4
55	130	1.1, 1.2, 1.3, 1.4
55	160	1.1, 1.2, 1.3, 1.4
55	190	1.1, 1.2, 1.3, 1.4
60	130	1.1, 1.2, 1.3, 1.4
60	160	1.1, 1.2, 1.3, 1.4
60	190	1.1, 1.2, 1.3, 1.4

In this chapter, the results from these simulations are presented and discussed. As mentioned in section 4.1.1, due to the inherent symmetry of the geometry, only half the domain was computed. Accordingly, it was only necessary to conduct the following analyses on half the domain. The shock waves investigated have initial profiles comprising a cylindrical and straight segment. It will be shown that during the course of the shock propagation, the initially cylindrical shock segment is distorted, and hence, does not remain cylindrical. Thus, from here on, this portion of the shock will be referred to as the curved shock segment. The implications that the interaction of the curved and straight shock segments have on the phenomena that occur as the shock wave propagates in the channel will be elucidated in the following sections.

5.1 General description of shock propagation

The results for a typical case, in which the profile of the initial shock wave transitioned into a configuration resembling a symmetrical pair of Mach reflections, is shown in Figure 5.1. Pressure contours depict the shock wave at different times during its progression in the converging channel. In this case, the walls of the channel converge at fifty degrees, and the shock wave has an initial Mach number and curvature radius of 1.3 and 160 mm, respectively.

Initially, the shock front is smooth and continuous (Figure 5.1a and 5.1b). As the shock wave converges, the curved segment straightens, and two kinks develop on the shock front (Figure 5.1c and 5.1d), from which reflected shocks emerge (Figure 5.1e and 5.1f). At this stage, the transition of the original shock wave profile into a symmetrical pair of Mach reflections is evident. As the shock continues down the channel, the triple points of the Mach-reflection pair follow a divergent trajectory towards the channel walls. Eventually, the reflected shocks and triple points meet the walls (Figure 5.1g), where the former is reflected (Figure 5.1f).

An evaluation of the pressure distribution immediately behind the shock wave, over the duration of its propagation, demonstrates the mechanisms responsible for the phenomena depicted in Figure 5.1. For any time during the shock's progression, the x and y coordinates of the nodes representing the fluid immediately behind the shock wave, and the corresponding values of static pressure at those nodes, were obtained using the method described in section 4.2. At any node, the length of the shock wave relative to the axis of symmetry was determined with numerical integration using the trapezoidal rule. It was then possible to plot the temporal variation of the pressure distribution along the length of the shock (L_{shock}). This is shown in Figure 5.2 for the same case portrayed in Figure 5.1.

It is evident that throughout the duration of the shock's progression, the pressure distributions are analogous. For each curve, consider the distribution from the origin (which is at the axis of symmetry) to where the end of the shock wave meets the channel wall. The pressure is approximately constant up until some point, where there is a drop in the

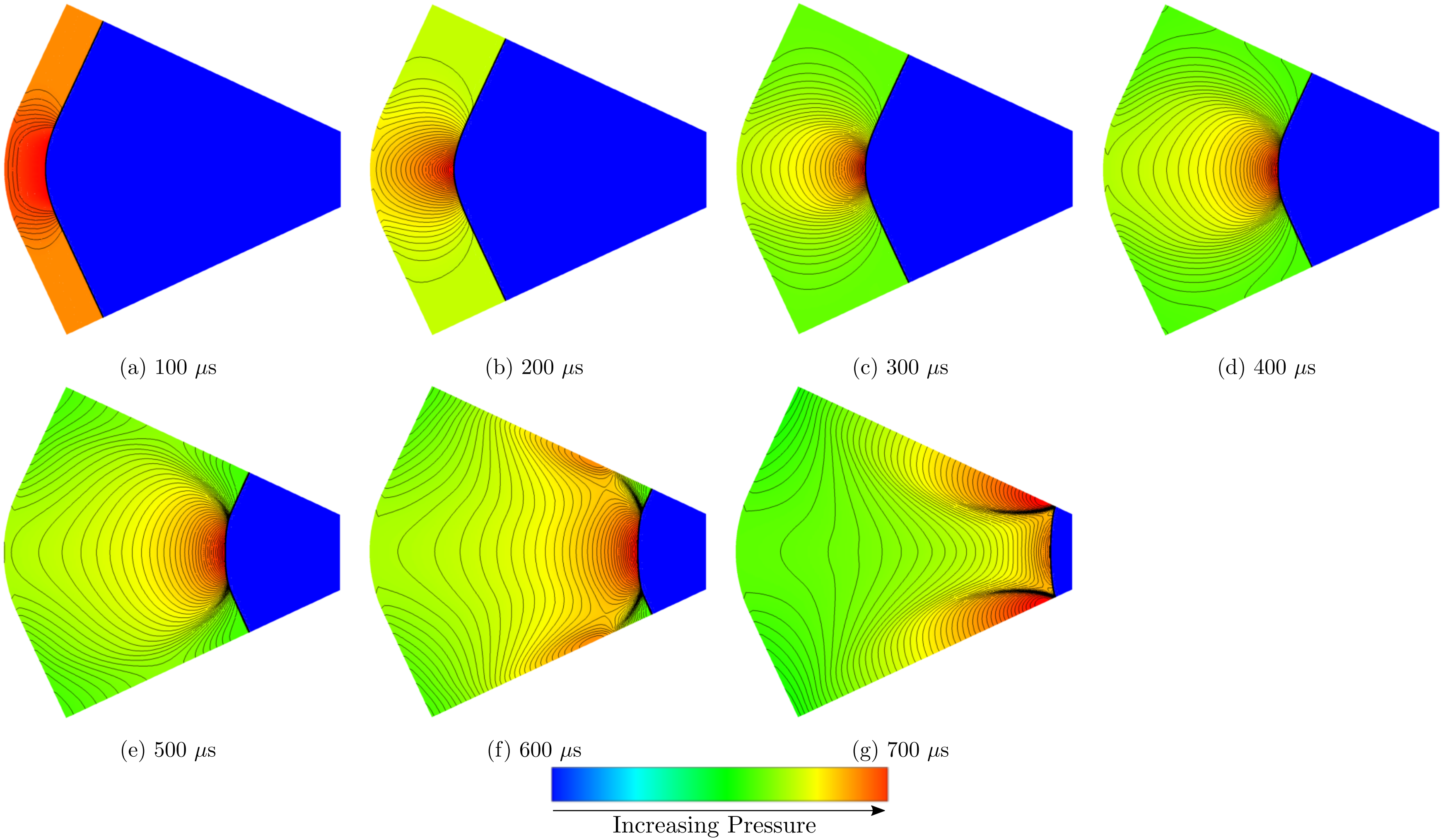

(a) 100 μs (b) 200 μs (c) 300 μs (d) 400 μs

(e) 500 μs (f) 600 μs (g) 700 μs

Figure 5.1: Pressure contours for the propagation of a curved shock wave in a converging channel (Wall Convergence Angle: 50 Degrees; Initial Shock Mach Number: Mach 1.3; Initial Shock Curvature Radius: 160 mm)

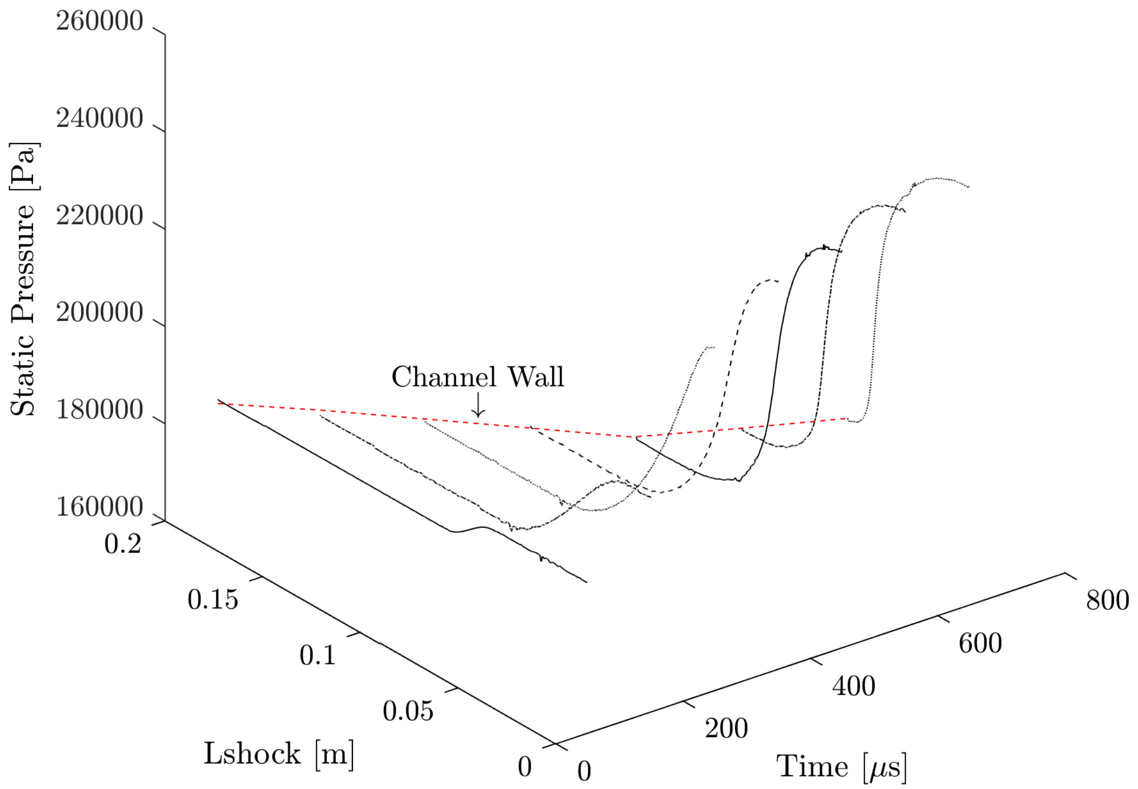

Figure 5.2: Temporal profile of pressure distribution along the length of the curved shock wave (Wall Convergence Angle: 50 Degrees; Initial Shock Mach Number: Mach 1.3; Initial Shock Curvature Radius: 160 mm)

pressure. Beyond this region, the pressure is once again constant. Over time, the pressure before the pressure drop increases, while the pressure after it remains essentially constant. The increase in the slope of the curve at the pressure drop indicates that this drop becomes steeper with time.

It is well-established, that the strength of planar shock waves is constant as they propagate. In contrast, cylindrical shock waves increase in strength as they converge. Since the pressure across the shock is directly related to its strength, it can be inferred that the pressure before the pressure drop, at the pressure drop, and after the pressure drop, corresponds to the pressure behind the curved shock segment, the region where the curved and straight shock segments meet, and the straight shock segment, respectively.

The result of the pressure difference between these two regions manifests in the phenomenon depicted in Figure 5.1. To repair this imbalance, compression waves, emanating from the region behind the curved segment, propagate outwards towards the region behind the straight segment. The effect of these compressions is to distort the shape of the curved shock segment (this effect is discussed further in section 5.2.2). As the strength of the curved shock segment increases (and consequently, the pressured difference steepens), the velocity of the subsequent compressions increases. As a result, they eventually coalesce into an additional pair of shock waves on the originally smooth shock front (Figure 5.1f), resulting in the configuration, which has been termed a symmetrical pair of Mach reflections.

5.2 Influence of critical parameters

The initial Mach number and curvature radius of the shock wave, as well as the angle at which the walls of the propagation channel converge, are critical in determining how certain features of the shock evolution are manifested. The influence of these parameters on this process is discussed in the following sections.

5.2.1 Trajectory of pressure variations

The pressure distribution behind the shock wave was numerically differentiated using finite difference approximations. This gave the distribution of the pressure gradients along the length of the shock wave. The temporal variation of the pressure gradient distribution is shown in Figure 5.3 for the case portrayed in Figure 5.1.

At any time during the shock's progression, the pressure gradient distribution is characterised by a rapid rise, followed almost immediately by a sharp dip in the pressure gradient. This occurs at some distance above the axis of symmetry (located at L_{shock} equals zero in Figure 5.3), and is a consequence of the pressure drop behind the shock wave (Figure 5.2). In section 5.1, it was deduced that the pressure drop behind the shock wave corresponds to the region behind the intersection of the curved and straight shock segments. Therefore, here too, this rise and fall in the pressure gradient, and in particular, the pressure gradient peak, must correspond to the region behind the intersection of the curved and straight shock segments.

As the shock progresses through the channel, the dip in the pressure gradient becomes steeper, and the pressure gradient peak increases. This is in accordance with the increase in the strength of the curved shock segment with time. The pressure gradient peak increases rapidly until some time, after which the increase is relatively gradual. The implications of this is discussed in section 5.2.1.1.

It is apparent in Figure 5.3, that the position behind the shock wave, at which the pressure gradient peak occurs, varies over time. Since this position corresponds to the region where the curved and straight shock segments meet, it follows that by plotting the temporal variation of its position, the trajectory of this region can be obtained. This has been demonstrated in

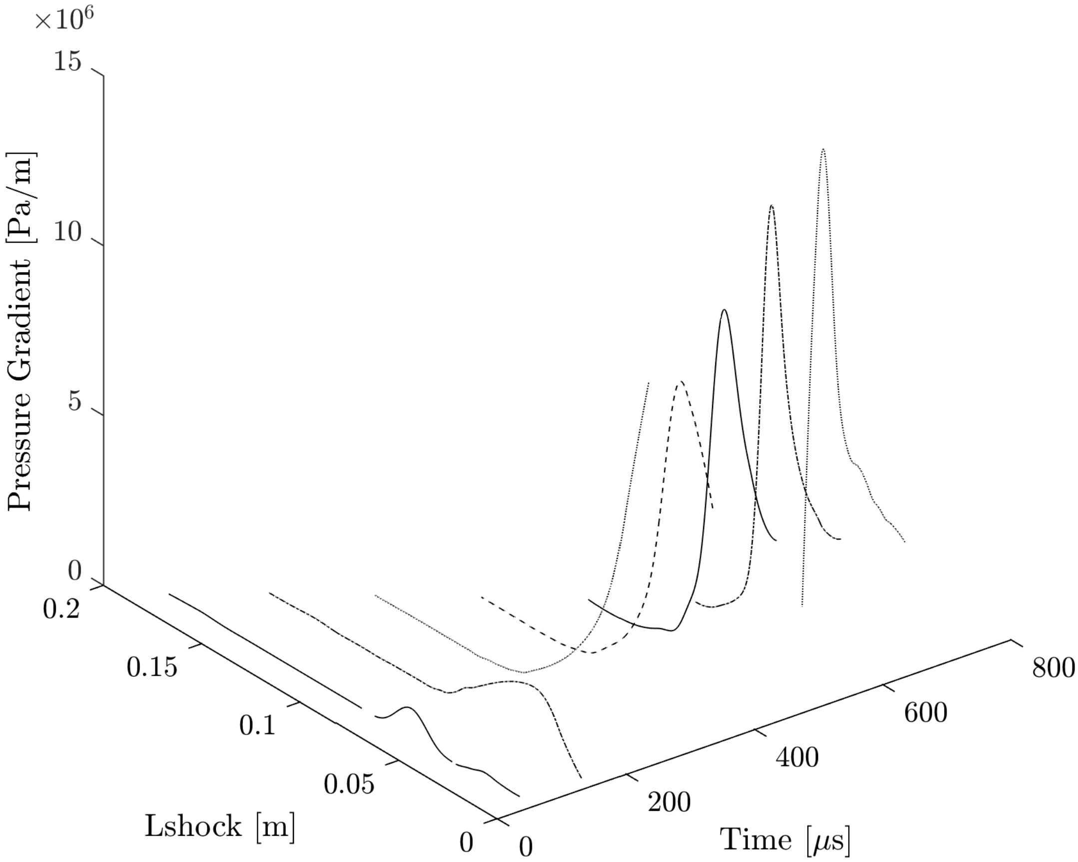

Figure 5.3: Temporal profile of the pressure gradient distribution along the length of the curved shock wave (Wall Convergence Angle: 50 Degrees; Initial Shock Mach Number: Mach 1.3; Initial Shock Curvature Radius: 160 mm)

Figure 5.4, where the position of the pressure gradient peak, represented by the filled circles, has been plotted on the shock wave at various times during its propagation.

At first, the pressure gradient peak moves towards the axis of symmetry (the x-axis in Figure 5.4), and then after reaching some minimum distance above it, it diverges away from the symmetry axis. As mentioned, the pressure gradient peak occurs behind the region where the curved and straight shock segments meet. Therefore, the propagation of the curved segment can be inferred from the trajectory of the pressure gradient peak. This conforms with what is known regarding the propagation of cylindrical shock waves; Initially, the curved segment (which was initially cylindrical) converges towards its focus, and then expands as it moves away from the focus. Clearly, the minimum height that the pressure gradient peak reaches, before diverging away from the symmetry axis, must then be the focus. The influence of the critical parameters on the trajectory of the pressure gradient peak (and by inference, the intersection of the curved and straight shock segments), as the shock wave moves towards and away from the focus, is discussed in the following sections.

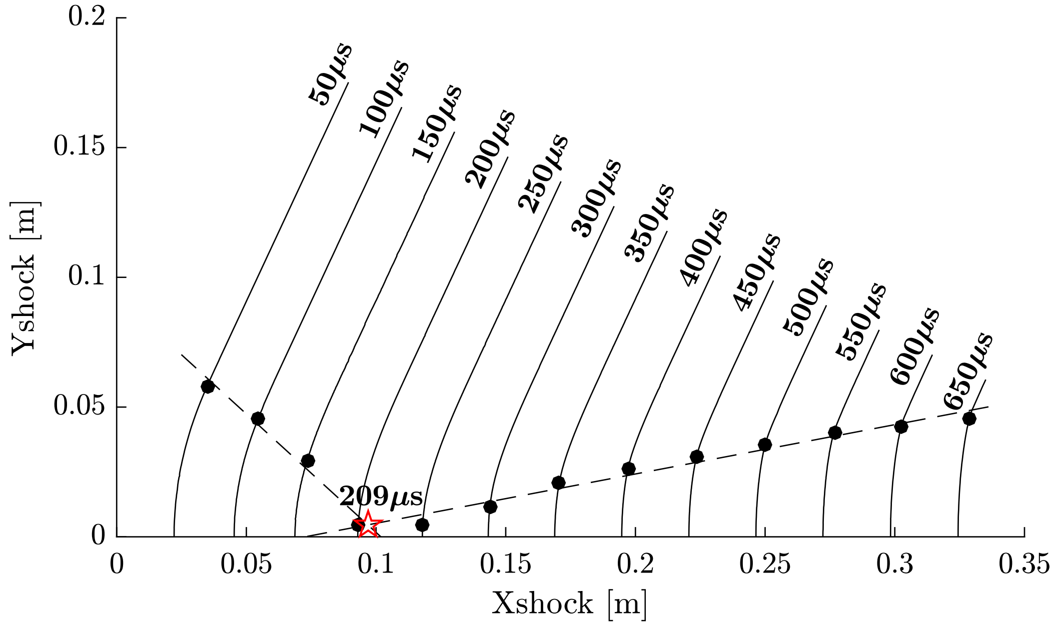

Figure 5.4: Progression of a curved shock wave with an initial Mach number and curvature radius of 1.3 and 160 mm (Wall Convergence Angle: 50 Degrees)

5.2.1.1 Prior to focus

Consider the trajectory of the pressure gradient peak in Figure 5.4. Both before and after the focus, it is essentially linear. The coordinates corresponding to the position of the pressure gradient peak over time were divided into two sets; one representing the positions before focus, and the other representing the positions after focus. A first-degree polynomial was then fitted to the coordinates in each set. This is plotted as the dashed lines in Figure 5.4, and an evaluation of the intersection of these two lines gives an estimation of the position of the focus (marked in Figure 5.4 with the red star, after the shock wave at 200 μs). This analysis was also applied to the variation of the y-coordinate of the pressure gradient peak with time, and the time it takes for the shock wave to reach the focus was thus obtained (in Figure 5.4, this is given by the label above the intersection point).

The time it takes for the shock wave to reach the focus was determined for all the cases summarized in Table 5.1. Its variation with the convergence angle of the channel walls was then plotted for shock waves with different initial curvature radii and Mach numbers in Figure 5.5. Although there is some scatter in these plots, the dotted lines fitted to the distinct sets of data do capture the general trends. From Figure 5.5, it is clear, that when the angle at which the channel walls converge is greater, the time to focus is longer. It is also evident that when the initial curvature radius of the shock wave is larger, and the initial shock Mach number is lower, it takes longer for the shock to reach the focus. This result is in accordance with what one would expect, given that shock waves with larger curvature radii and lower Mach numbers are synonymous with weaker, and hence, slower shocks (this is demonstrated in section 5.2.3).

Intuitively, the rate at which the shock focuses (and consequently, the time to focus) is dependent on the rate at which the shock increases in strength before the focus. The Rate of Change (ROC) of the maximum pressure gradient over time is a convenient measure of the rate at which the shock increases in strength, and hence, of the acceleration of the shock wave. Therefore, the rate at which the maximum pressure gradient changes with time before the focus was determined for various cases. This is shown in Figure 5.6 for the propagation of shock waves, with different initial Mach numbers and curvature radii, in channels with varying wall convergence angles.

In all cases, at some time after the start of the shock propagation, there is an exponential growth in the rate at which the maximum pressure gradient increases, and hence, in the acceleration of the shock wave. Therefore, the earlier this increase occurs, the sooner the shock wave arrives at the focus. In Figure 5.6, it is evident, that shock waves experience this exponential increase earlier, and therefore, arrive at the focus sooner, when the initial Mach number is higher, the initial curvature radius is smaller, and the wall convergence angle of the propagation channel is lower. This corresponds with the results presented in Figure 5.5.

Finally, the slope of the curves in Figure 5.6a is steeper when the initial shock Mach number is higher. Therefore, the shock wave accelerates at a greater rate when the initial Mach number is higher. In contrast, the slopes of the curves in Figure 5.6b and 5.6c are almost indistinguishable. This implies that the initial Mach number of the shock wave has a more significant influence on the rate at which the shock wave accelerates and reaches the focus than the initial curvature radius and wall convergence angle.

5.2.1.2 Post focus

Consider the propagation of the shock wave depicted in Figure 5.1. In this case, the shock wave arrives at the focus at approximately 209 μs. Clearly, at this time, the reflected shocks have not yet developed (Figure 5.1b). It was deduced in section 5.2.1.1, that the intersection of the dashed lines, plotted in Figure 5.4, represents the focus of the shock wave. Accordingly, the line on the left (with the negative slope) in Figure 5.4 corresponds to the trajectory of the shock wave towards the focus, and the line on the right (with the positive slope) corresponds to the trajectory of the shock wave away from the focus. This is true for all the cases in Table 5.1. As discussed in section 5.2.1, the pressure gradient peak behind the shock wave occurs in the region where the curved and straight shock segments meet, and the subsequent

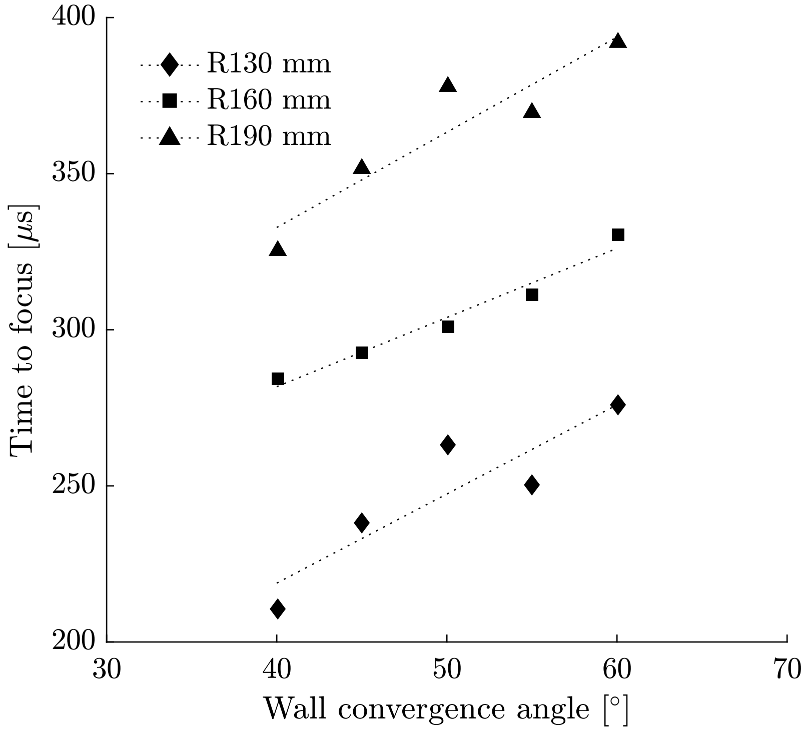

(a) For Mach 1.1 shock waves with different initial curvature radii

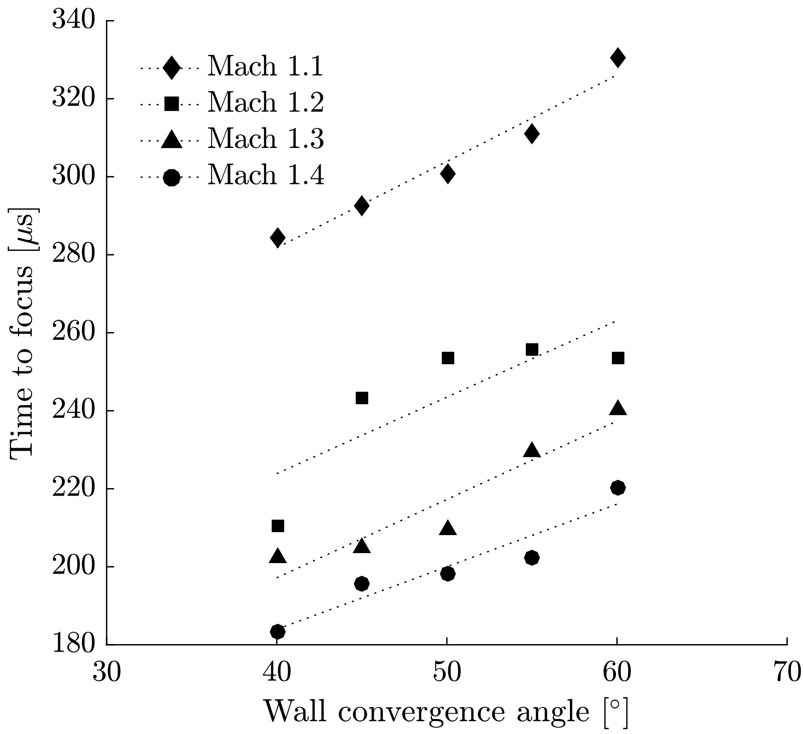

(b) For shock waves with a radius of 160 mm at different Mach numbers

Figure 5.5: Variation of time to focus with wall convergence angle

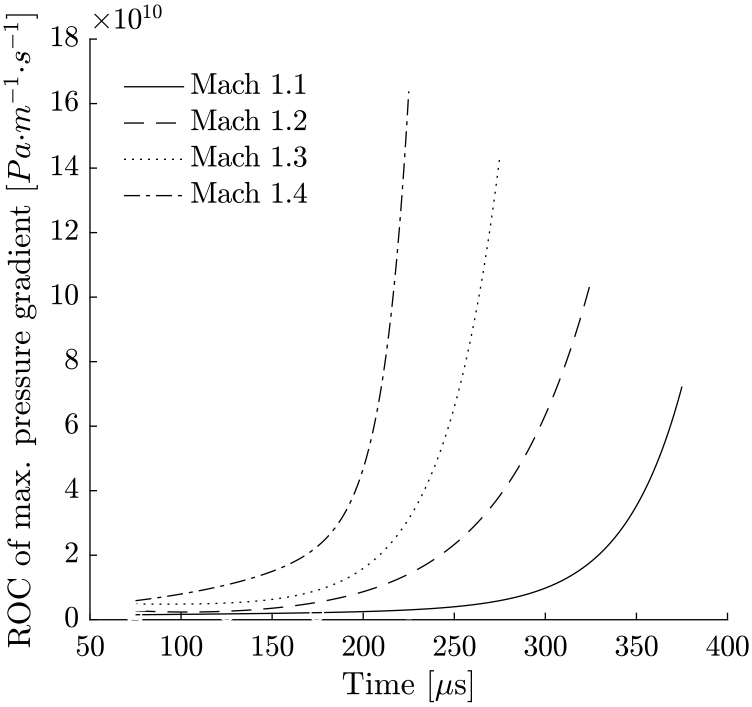

(a) For shock waves with different initial Mach numbers
(Curvature radius: 190 mm; Wall angle: 60 °)

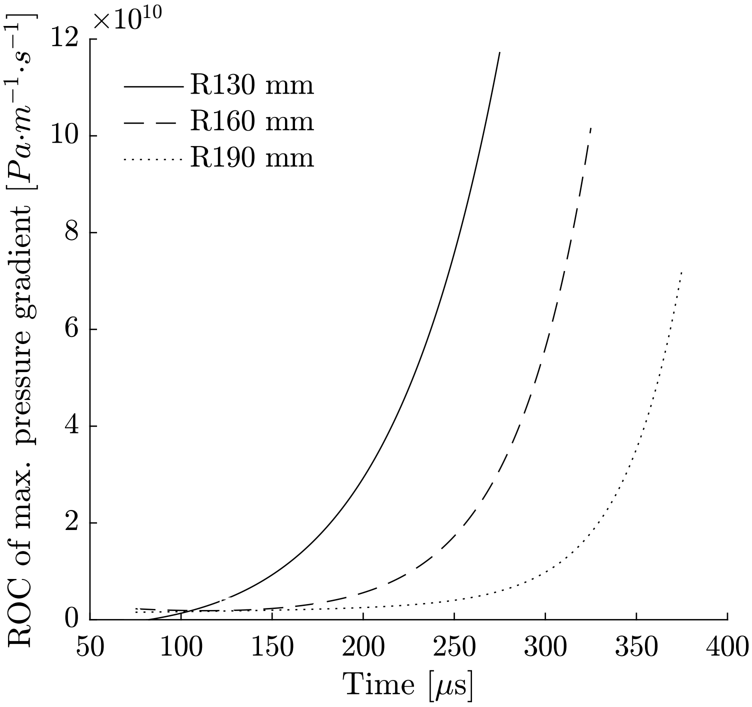

(b) For shock waves with different curvature radii
(Initial Mach number: 1.1; Wall Angle: 60 °)

Figure 5.6: Rate of change of maximum pressure gradient

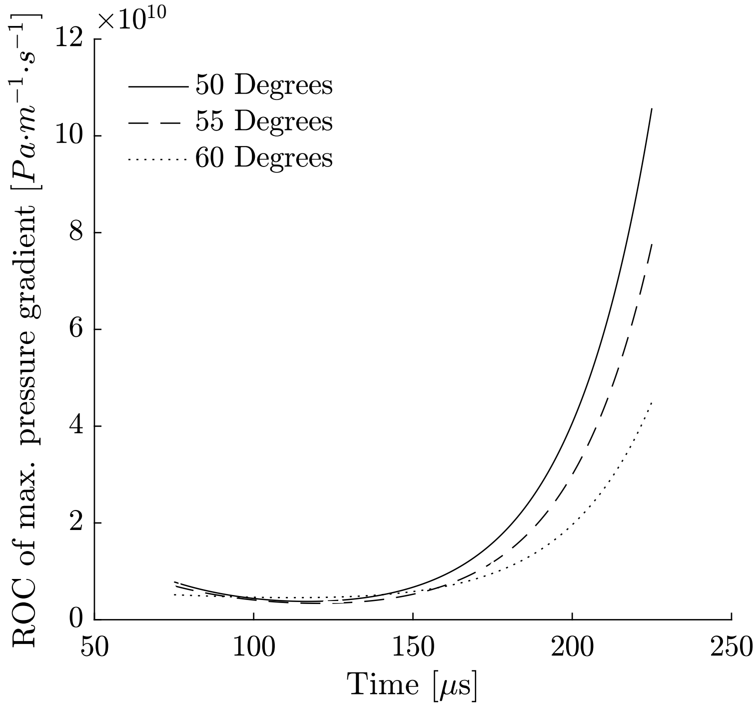

(c) For the propagation of shock waves in channels with different wall angles (Curvature radius: 160 mm; Initial Mach number: 1.2)

Figure 5.6: *(cont.)* Rate of change of maximum pressure gradient

drop in the pressure gradient becomes steeper with time (Figure 5.3). As the drop in the pressure gradient becomes steeper, it suggests a discontinuity in the pressure behind the shock wave, in this region. Since, discontinuities in the thermodynamic properties of a fluid are characteristic of shock waves, it follows that the reflected shocks eventually emerge in the region where the curved and straight shock segments meet. Therefore, the upward sloping line on the right in Figure 5.4, not only describes the trajectory of this region away from the focus, it also represents the development of the trajectory of the triple points of the eventual Mach reflection pair. Thus, the slope of this line tends to that of the triple point trajectory.

The trajectory angle of the triple points (θ_{TP}) was determined for the cases summarized in Table 5.1. In Figure 5.7, the variation of the trajectory angle with the initial curvature radius and wall convergence angle, for shock waves with different initial Mach numbers, was plotted. It is evident that the higher the initial Mach number of the shock wave, the steeper the trajectory angle of the triple points. The trajectory angle is also steeper when the initial curvature radius of the shock wave is larger (Figure 5.7a) and the convergence angle of the channel walls is lower (Figure 5.7b). Additionally, since the slopes of the different lines in the plots in Figure 5.7 appear to be almost identical, it can be inferred, that the rate at which the trajectory angle varies with the initial curvature radius and wall convergence angle is essentially independent of the shock Mach number.

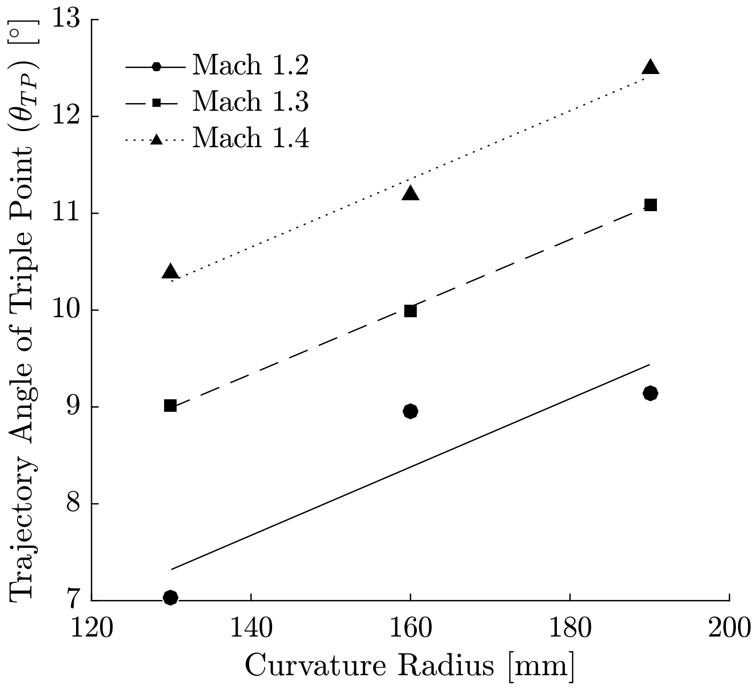

(a) Variation of triple point trajectory with curvature radius
(Wall Angle: 50 °)

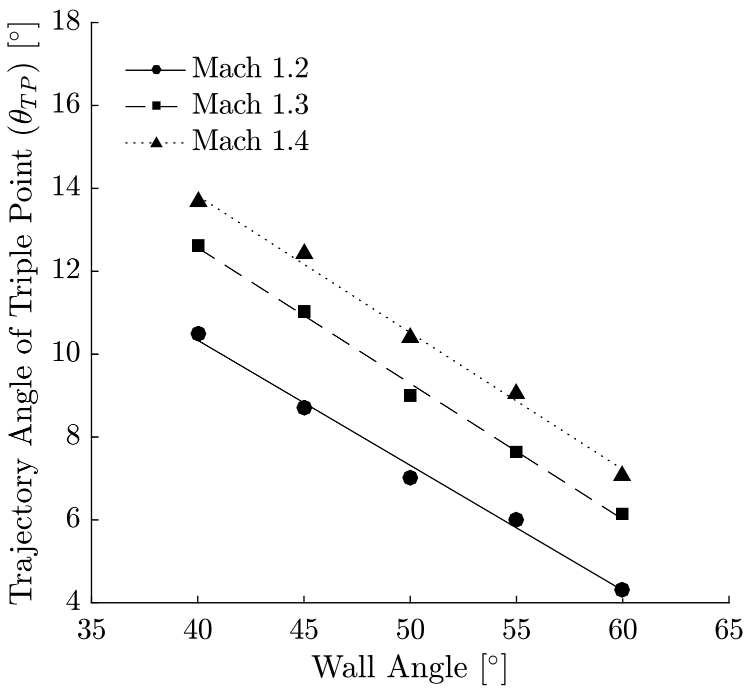

(b) Variation of triple point trajectory with the wall angle
(Initial curvature radius: 130 mm)

Figure 5.7: Variation of the trajectory angle of the triple points for shock waves with different initial Mach numbers

When the trajectory angle of the triple points is greater, the triple points intersect the walls of the propagation channel earlier. Hence, this is the case for shock waves with higher initial Mach numbers and curvature radii, and channels with lower wall convergence angles. The ramifications of this on the development of the reflected shocks, within the duration of the shock propagation, is discussed in section 5.2.3.

5.2.2 Evolution of shock front profile

It was discussed in section 5.1, that during the course of the shock propagation, the shape of the curved segment is distorted. The extent of this distortion can be ascertained by evaluating the temporal variation of the overall shock curvature. Figure 5.8 illustrates how the overall shock curvature, at any given time, was determined.

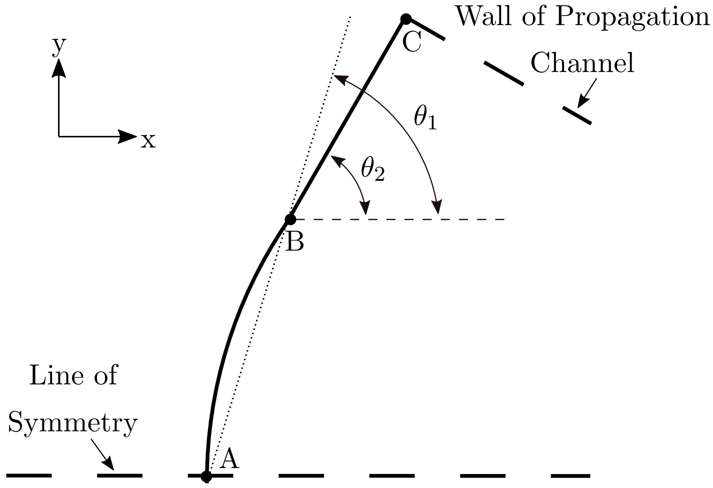

Figure 5.8: Determination of overall shock curvature.

Points A, B and C correspond to the coordinates of the shock wave at the line of symmetry, the intersection of the curved and straight shock segments, and the wall of the propagation channel, respectively. Thus, the portion of the shock wave in-between points A and B corresponds to the curved segment, while the portion in-between points B and C corresponds to the straight segment. The coordinates of points A and C were easily obtained from the set of shock coordinates extracted in section 5.1, by identifying the points with the minimum and maximum y-coordinate, respectively. It has been deduced (section 5.2.1) that the shock locus behind which the pressure gradient peak occurs corresponds to the region where the curved and straight shock segments meet. Thus, the coordinates of point B were considered to be those of this shock locus. The slope of a straight line extending from point A to B (θ_1), and another extending from point B to C (θ_2) was then determined. The overall curvature of the shock wave (κ) was defined as,

$$\kappa = \theta_1 - \theta_2 \tag{5.1}$$

According to this definition, the overall curvature of the shock wave (κ) is an implicit measure of the overall change of direction of the curved segment of the shock wave relative to the straight segment. It is important to recognize that the slope θ_1 is not the actual slope of the shock wave between points A and B. This portion of the shock wave is curved, and therefore, the slope changes continuously in this region. Although the curvature here is not a precise measurement, a temporal profile of this quantity does provide an indication of the general distortion of the shock wave over time; As the x-coordinates of points A and B move closer together, the slope θ_1 increases, and thus, the overall curvature increases. From Figure 5.8, it is evident that as the overall curvature increases, the curved portion of the shock front flattens and tends towards a straight segment.

The temporal variation of the overall shock curvature was determined for the cases summarized in Table 5.1. This is shown in Figure 5.9a for the propagation of shock waves in channels with different wall convergence angles. Initially, there is a sharp increase in the overall curvature of the shock wave. For the remainder of the shock's progression, this increase is increasingly gradual, to the extent that after the initial spike, the curvature appears to be essentially constant. This implies that the shape of the curved shock segment is distorted and flattened most significantly early on during the shock's progression. This occurs rapidly and any further distortion is negligible in comparison.

As demonstrated in Figure 5.9a, when the angle at which the channel walls converge is higher, the overall curvature of the shock wave is greater. This is because the initial curvature of the shock wave (at the start of its propagation) is greater when the convergence angle of the channel walls is higher. Taking into consideration the geometry described in section 4.1.1 which defines the profile of the initial shock wave, this result is intuitive.

To gain insight into the mechanism responsible for the distortion of the shock front, consider Figure 5.9b which shows the variation of the overall shock curvature with the maximum pressure gradient. It is immediately apparent that the profile of these curves is analogous to those in Figure 5.9a. Thus, the increase in the curvature of the shock wave is a direct result of the increase in the maximum pressure gradient. Since there is a sharp increase in the maximum pressure gradient as the shock wave converges to the focus (Figure 5.3 and 5.6c), there is a corresponding increase in the overall curvature of the shock wave. Hence, it is as the shock wave converges to the focus that the shape of the curved portion of the shock front is significantly distorted and straightened.

It should be noted that there was some scatter in the data generated for the plots presented in Figure 5.9, and that the curves shown here were those that best captured the general trends. Therefore, these plots should not be used to obtain precise values, but rather their function is to illustrate the typical pattern associated with the distortion of the shock front.

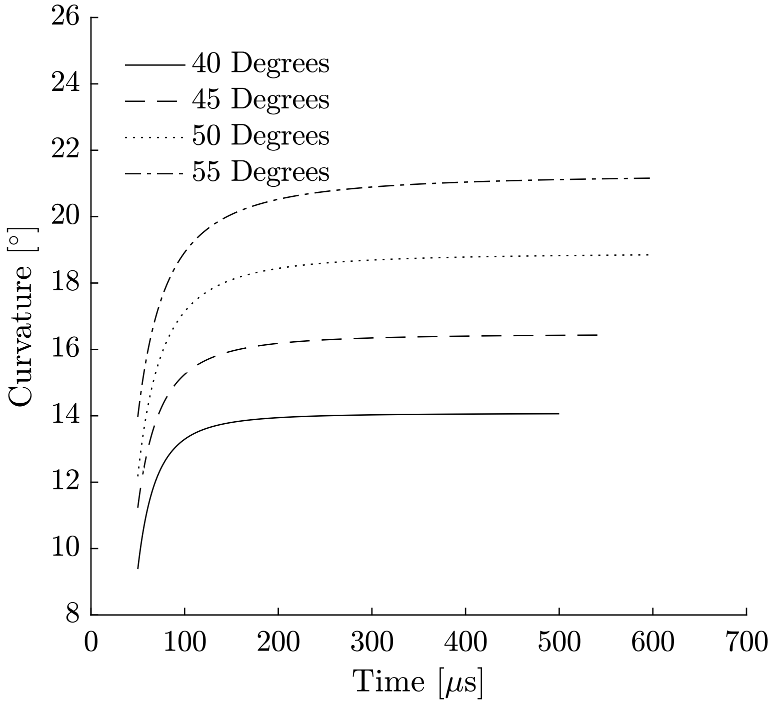

(a) Temporal variation of the overall shock curvature

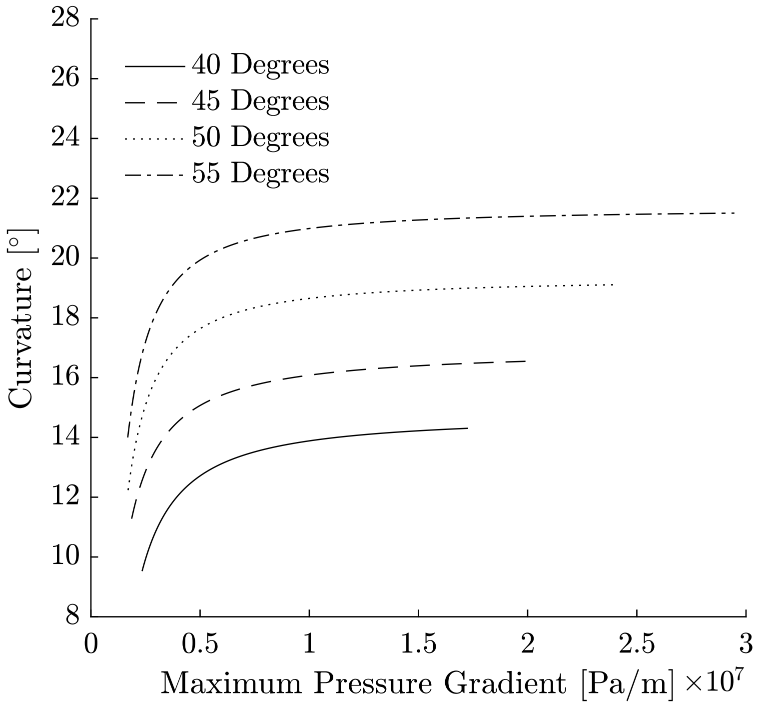

(b) Variation of overall shock curvature with the max. pressure gradient

Figure 5.9: Variation of the overall shock curvature for a shock wave with an initial Mach number and curvature radius of 1.4 and 130 mm

5.2.3 Transition

In Figure 5.10, the influence of the convergence angle of the channel walls, the initial shock Mach number, and the curvature radius, on the temporal variation of the pressure gradient distribution behind the shock wave is illustrated. It was established in section 5.2.1.2, that the position behind the shock wave, where the pressure gradient peak and the subsequent drop in pressure gradient occurs, corresponds to where the reflected shocks eventually emerge. Thus, at any given time, the slope of the pressure gradient distribution at the drop is an indication of the degree to which the reflected shock has developed. Furthermore, the rate at which this slope becomes steeper over time indicates the rate at which the reflected shocks develop. Therefore, a comparison, at corresponding times, of the slope of the curves of the various cases in each plot allows the influence of the critical parameters on the rate at which the reflected shocks develop to be deduced.

Initially, the slope at the pressure gradient drop is steeper when the wall convergence angle is lower (Figure 5.10a). This is because shock waves propagating in channels with lower wall angles converge to the focus at a faster rate. However, at later times during the shock's progression, the slope at the pressure gradient drop is steeper when the wall convergence angle is higher. It is possible that the reason for this is that the strength of the shock wave (and accordingly, the magnitude of the maximum pressure gradient) when it arrives at the focus is greater when the wall convergence angle is higher. Since the increase in the strength of the shock wave, as it moves away from the focus is gradual relative to the increase in its strength as it focuses, shock waves propagating in channels with higher wall convergence angles exceed in strength shock waves in channels with lower wall angles. Therefore, the rate at which the reflected shocks develop is greater when the wall convergence angle is higher. Hence, the reflected shocks emerge on the shock front earlier than when the wall angle is lower.

In Figure 5.10b and Figure 5.10c, it is evident that when the initial Mach number of the shock wave is higher, and the curvature radius is smaller, the slope at the pressure gradient drop becomes steeper at a greater rate. This is especially apparent at 200 μs in Figure 5.10b, and at 300 μs in Figure 5.10c. From this it can be inferred, that a reflected shock emerges on the shock front sooner when the initial Mach number of the shock wave is higher, and the curvature radius is smaller.

In order to gain insight into the effect of the critical parameters on whether the profile of the shock wave transitions within the duration of its propagation, the temporal evolution of the shock profile, for all the cases summarized in Table 5.1, was evaluated. A shock wave was considered to have transitioned, if reflected shocks of comparable strength to the primary

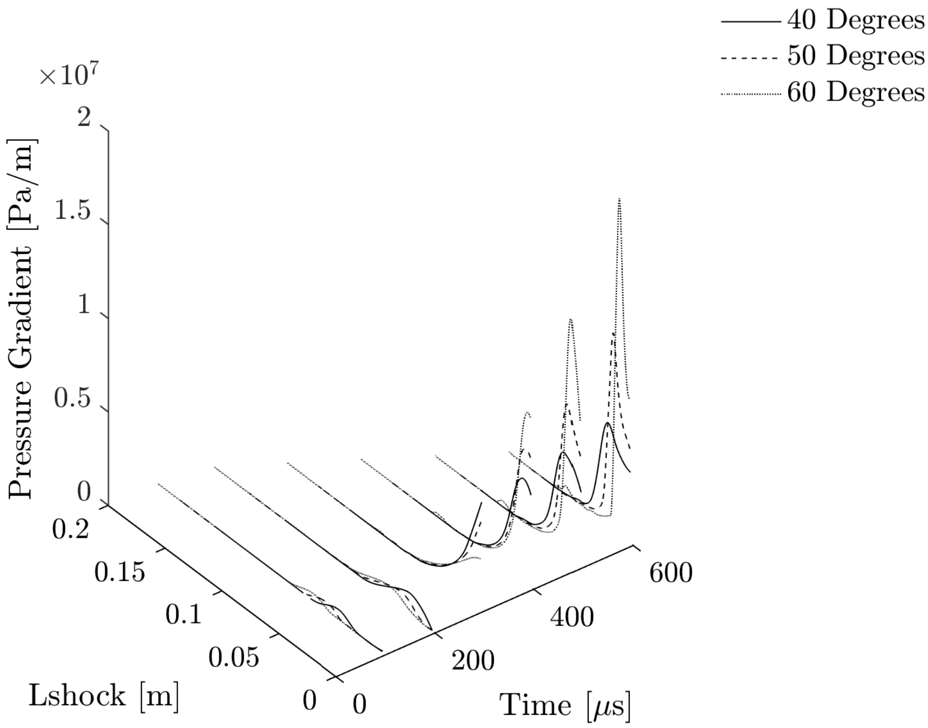

(a) Influence of wall convergence angle

(Initial Mach number: 1.1; Curvature radius: 160 mm)

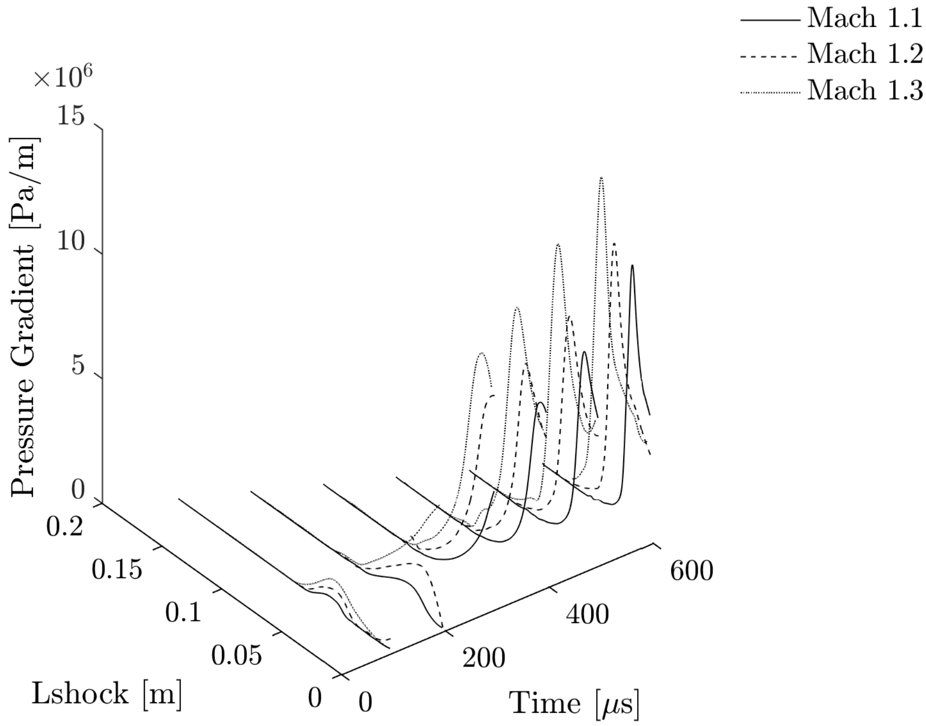

(b) Influence of initial shock Mach number

(Curvature radius: 160 mm; Wall Angle: 50 °)

Figure 5.10: Temporal variation of the pressure gradient distribution behind the shock wave for different wall angles, shock Mach numbers, and curvature radii

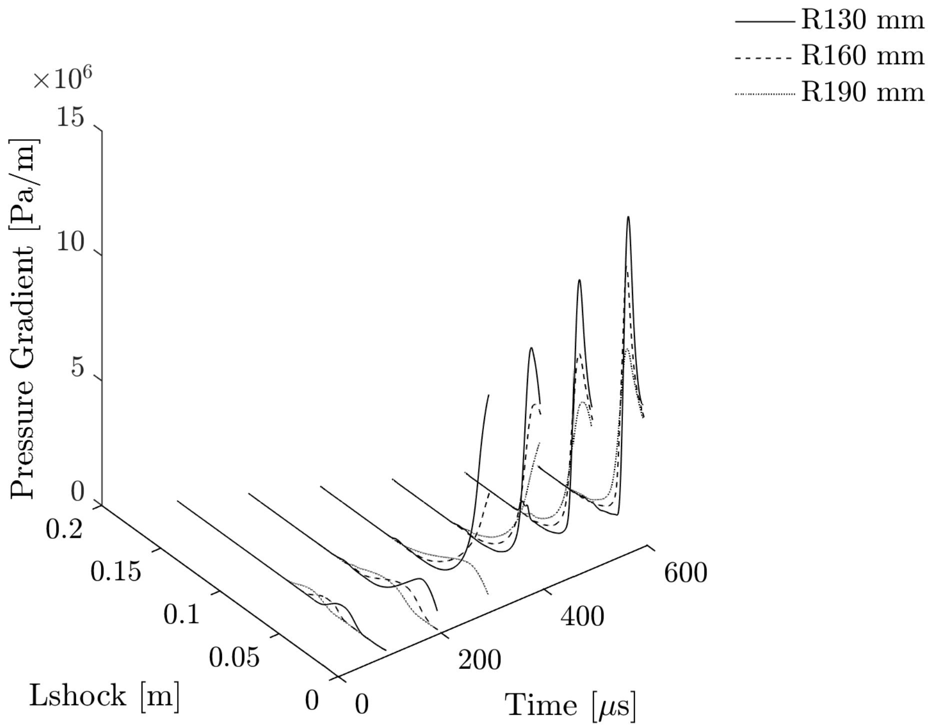

(c) Influence of curvature radius (Initial Mach number: 1.1; Wall Angle:50 °)

Figure 5.10: *(cont.)* Temporal variation of the pressure gradient distribution behind the shock wave for different wall angles, shock Mach numbers, and curvature radii

shock front had emerged before the region where the curved and straight shock segments meet (representative of the locus of the eventual triple points) intersected the walls of the propagation channel. In Figure 5.11 - 5.13, pressure contours depicting the progression of the shock wave for different cases are shown, to illustrate how the various cases were assessed.

In Figure 5.11, consider the shock wave at 550 μs, just prior to the instant the triple points meet the walls of the propagation channel (Figure 5.11f). Although the compressions behind the shock wave have begun to coalesce into the start of reflected shocks, this has not occurred to the same extent as the compressions comprising the primary shock wave. Therefore, in this case, it was considered that the shock wave had not yet transitioned before its triple points interacted with the channel walls. In contrast, in Figure 5.12, even though the reflected shocks emerge only just before the triple points intersect the channel walls (Figure 5.12f), the compressions have coalesced to a similar extent as those defining the primary shock wave. Thus, for this case, the shock wave was determined to have transitioned. In Figure 5.13, it is immediately clear that reflected shocks have emerged on the shock front, long before the triple points meet the channel walls. Therefore, in this case, the shock wave has undoubtedly transitioned.

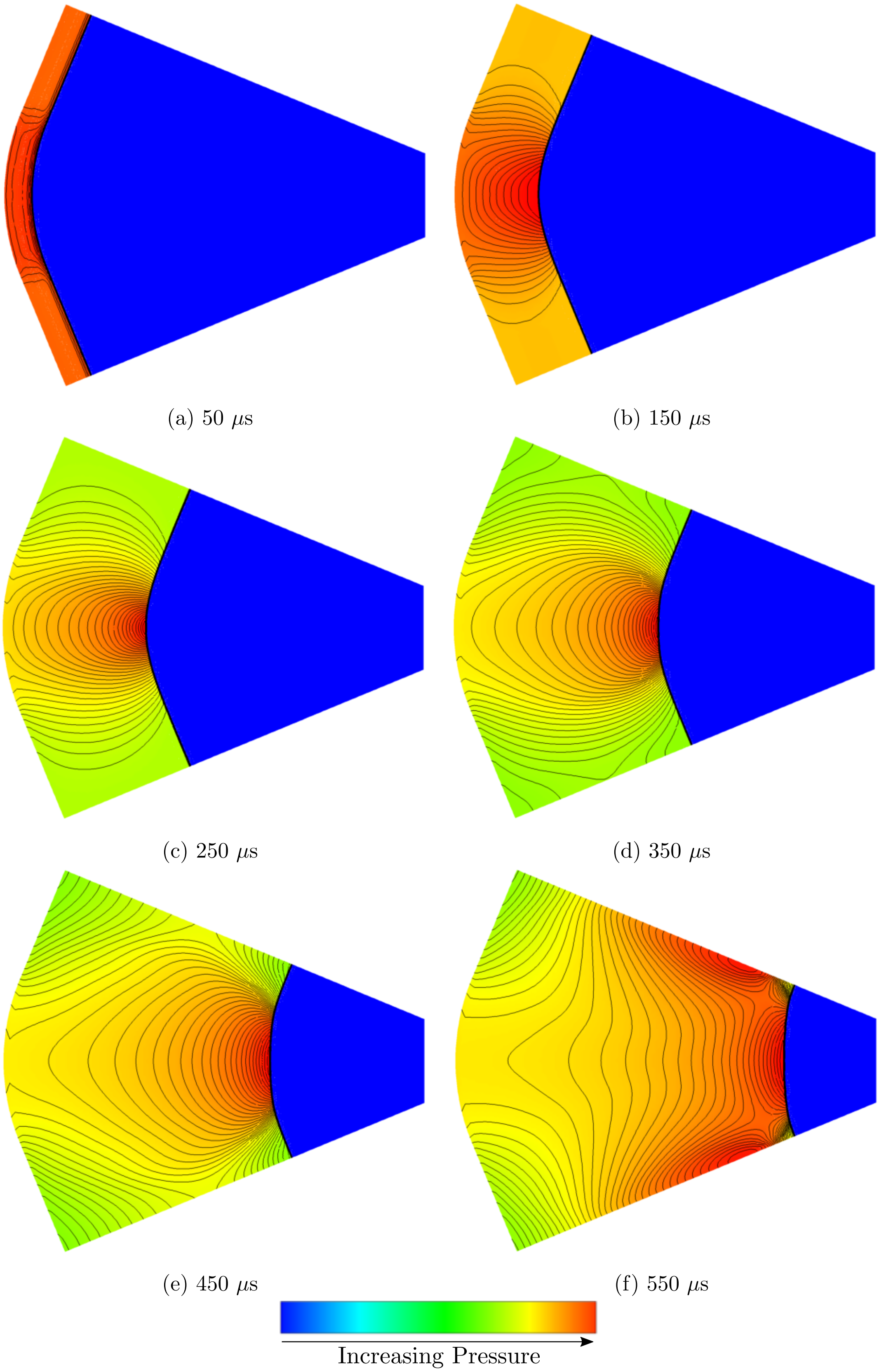

Figure 5.11: Propagation of a shock wave in a channel converging at 45 degrees. The shock wave has an initial Mach number and curvature radius of 1.4 and 190 mm

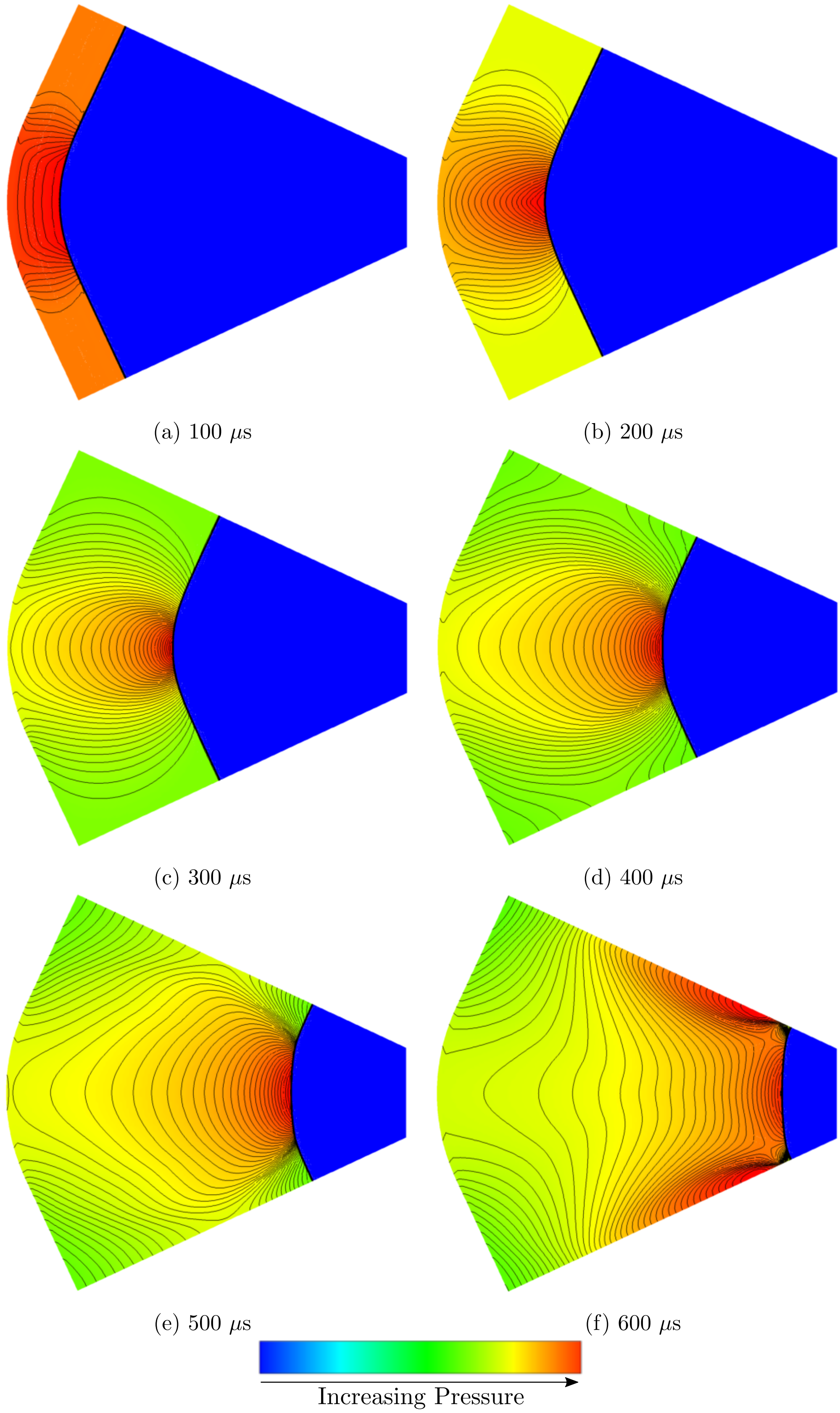

Figure 5.12: Propagation of a shock wave in a channel converging at 50 degrees. The shock wave has an initial Mach number and curvature radius of 1.4 and 190 mm

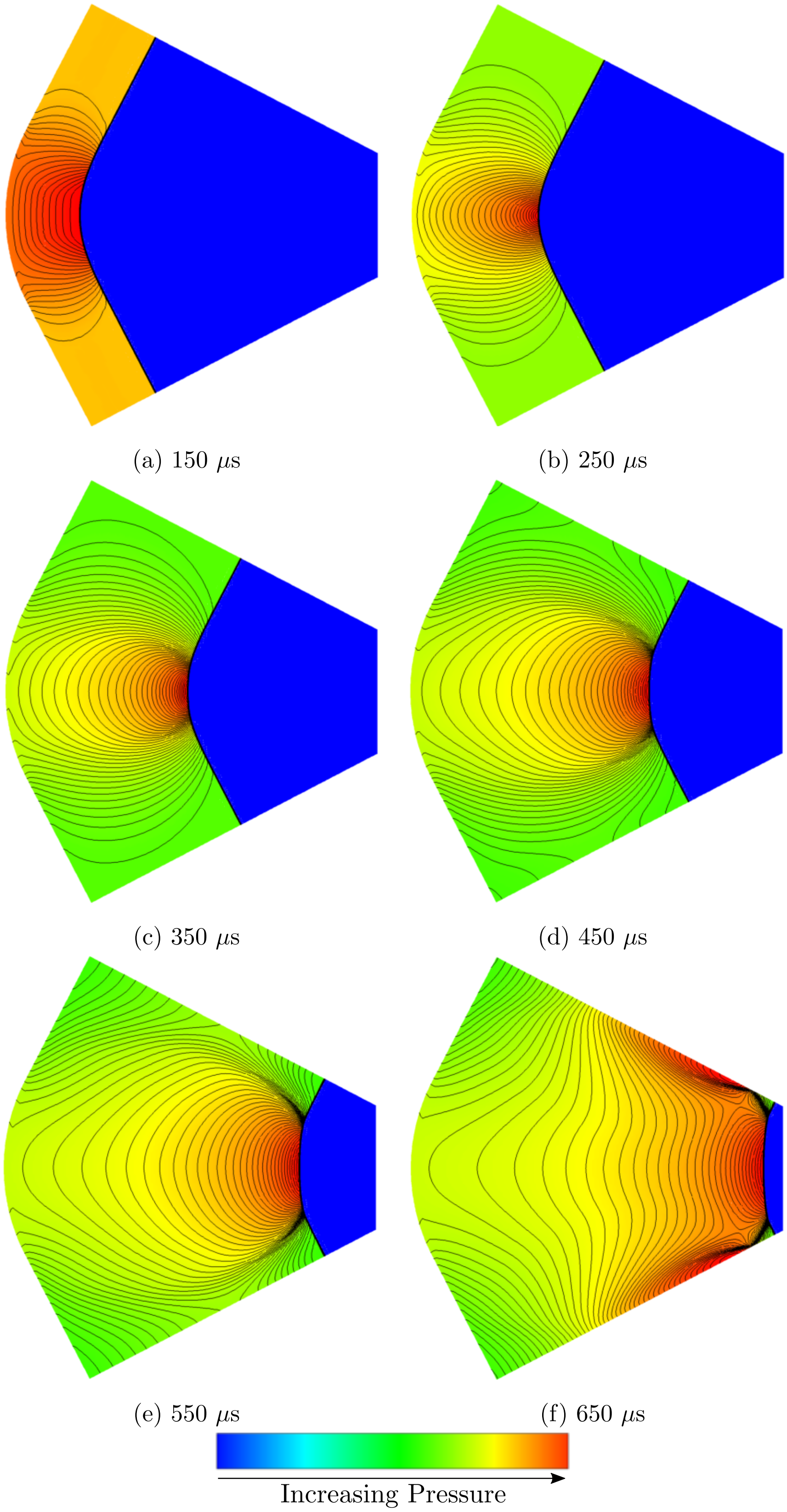

Figure 5.13: Propagation of a shock wave in a channel converging at 55 degrees. The shock wave has an initial Mach number and curvature radius of 1.4 and 190 mm

The transition classification of the various cases that were evaluated is presented in Figure 5.14, for shock waves with initial curvature radii of 130 mm (Figure 5.14a), 160 mm (Figure 5.14b) and 190 mm (Figure 5.14c). For each case, if the shock wave was determined to have transitioned, it was classified as MR (filled circles in the plots in Figure 5.14), implying that Mach reflections did emerge during its progression. If the shock wave was determined to have not transitioned, it was classified as No MR (crosses in the plots in Figure 5.14), implying that Mach reflections did not emerge during its progression. In the plots in Figure 5.14, each distinct case can be identified by the initial Mach number of the shock wave (y-axis) and the wall convergence angle of the propagation channel (x-axis).

For all the cases presented in Figure 5.14a, transition occurred. However, when the initial curvature radius was greater than 130 mm, as in Figure 5.14b and Figure 5.14c, this was not the case. In Figure 5.14b, where the initial curvature radius of the shock wave was 160 mm, when the convergence angle of the propagation channel was less than 45 degrees, and the shock Mach numbers was greater than 1.2, transition did not occur. Similarly, when the initial curvature radius is 190 mm (Figure 5.14c), for wall angles less than 50 degrees and shock Mach numbers greater than 1.2, and for wall angles less than 45 degrees and shock Mach number greater than 1.1, transition does not occur.

Although qualitative, the results of this evaluation do provide an indication of the influence of the critical parameters on transition. The likelihood of transition occurring during the shock's progression decreases when the initial Mach number and curvature radius of the shock wave is higher, and the convergence angle of the propagation channel is lower. This agrees with the results in section 5.2.1.2, which showed that for the corresponding conditions, the trajectory angle of the triple points is greater. As was discussed there, when the trajectory angle of the triple points is greater, the triple points meet the walls of the channel earlier. Since the triple points intersect the channel walls earlier, there is less time for reflected shocks to develop before this interaction occurs, and thus, the possibility of transition occurring is reduced. This was exactly the case in Figure 5.11. Another aspect to consider is that when the initial curvature radius of the shock wave is larger and the wall convergence angle is lower, it takes longer for reflected shocks to develop. This was demonstrated in Figure 5.10a and Figure 5.10c. Consequently, for these conditions, the likelihood of transition occurring is reduced even further.

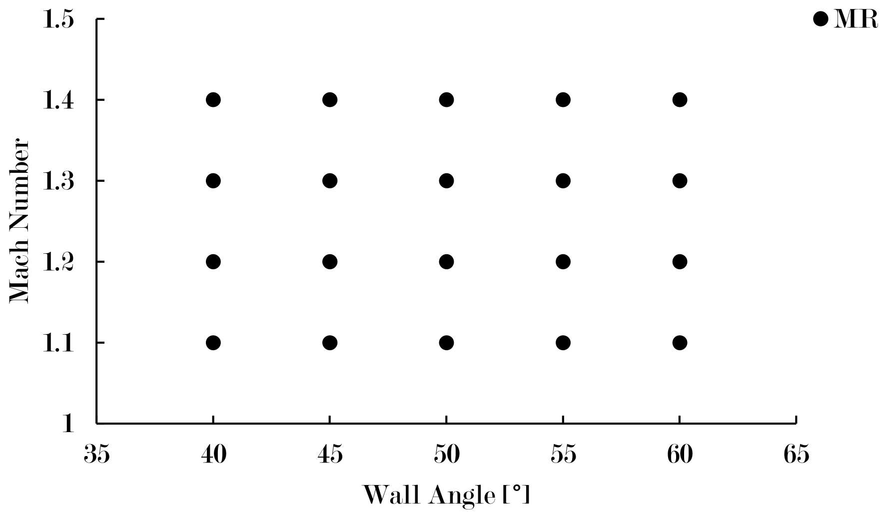

(a) For shock waves with an initial curvature radius of 130 mm

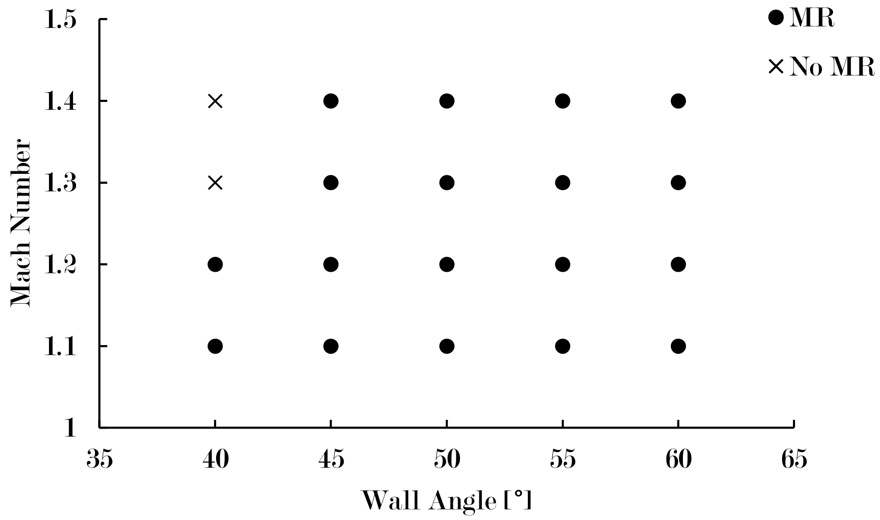

(b) For shock waves with an initial curvature radius of 160 mm

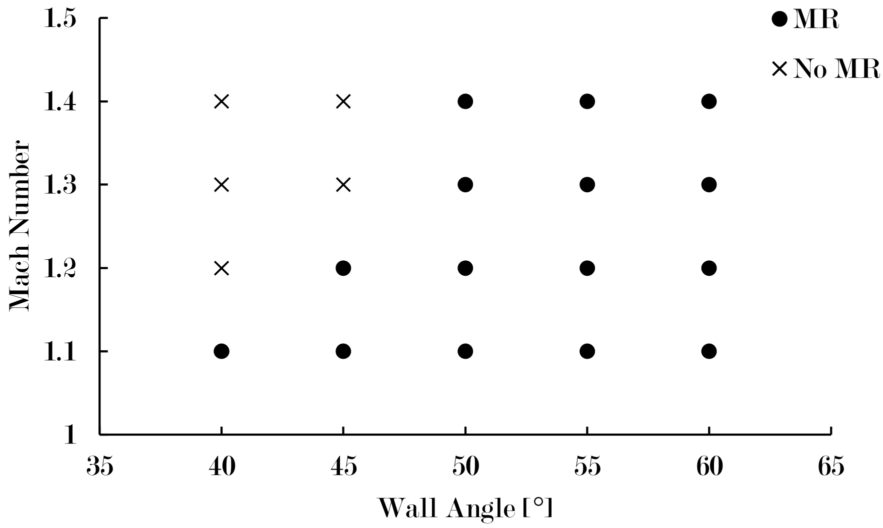

(c) For shock waves with an initial curvature radius of 190 mm

Figure 5.14: Transition classification

6 Experimental Results

6.1 Slit profiles

In the experimental component of the investigation, shock waves with various profiles were evaluated. The profiles of the shock waves to be studied had to be specified in advance of the testing so that corresponding profile and propagation plates could be manufactured. These plates were used in conjunction with the existing facility described in section 3.2 to generate shock waves with the required profiles. As shown in Figure 6.1, the distance between the back face of the slit and the point at which the walls of the propagation chamber converge, as well as the convergence angle of the walls, are fixed by the design of the facility. Considering these constraints and that the shape of the generated shock wave corresponds to the slit profile, shock waves with different profiles were achieved by varying the curvature radius of the slit. Finally, the slit had to fit within the cross-sectional area at the shock tube exit. Therefore, its width and height were limited by the width and height of the shock tube exit.

A preliminary numerical investigation was conducted to determine what shock profiles to evaluate in the experiments. Since high-speed images of the shock propagation would be obtained from the tests, the primary consideration was what stage of the shock propagation occurred within the facility's viewing window. It was found that for shock Mach numbers within the range achievable by the shock tube (calibration data from previous tests with the LSDST gauged this to be between 1.1 - 1.5), this was primarily dependent on the curvature radius of the shock wave, and not the Mach number. In Figure 6.2 and 6.3, density contours showing the propagation of two shock waves with significantly different curvature radii are presented. This demonstrates the effect of the curvature radius of the shock wave on what stage of the propagation occurs within the window region, and hence, on what would be captured in the high-speed images during the experimental tests.

The dashed circle drawn on each image in Figure 6.2 and 6.3 represents the outline of the window frame. This enabled the part of the shock progression visible in the facility's window

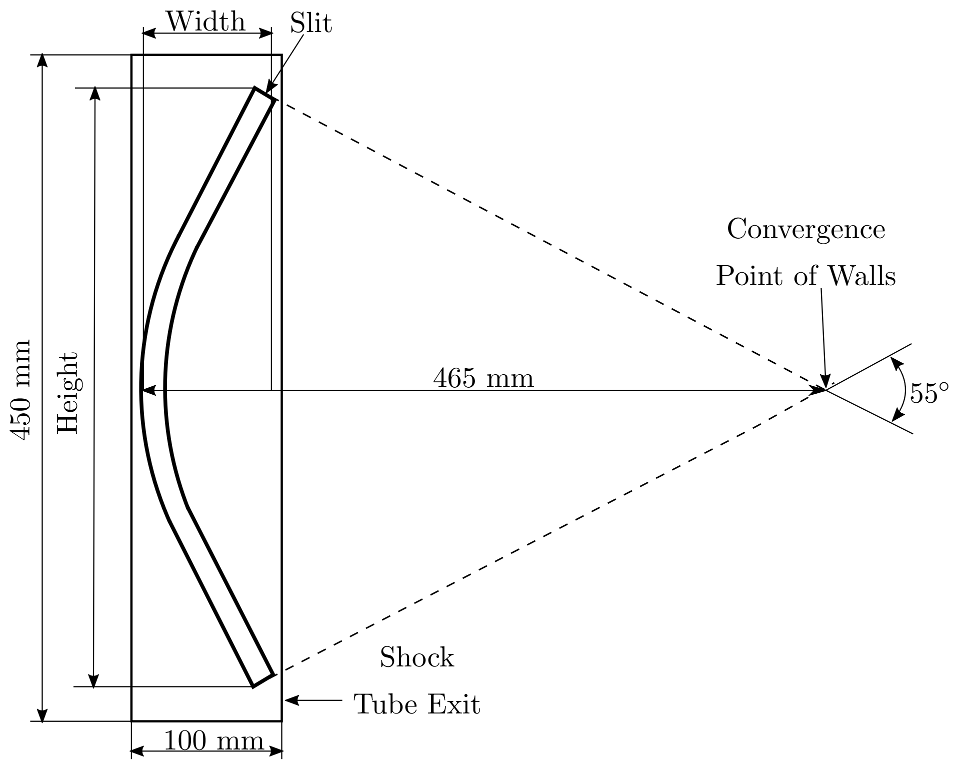

Figure 6.1: Constraints imposed by the existing facility on possible slit profiles

to be assessed. The shock wave moves from left to right and is shown from the moment it enters the window region and becomes visible (Figure 6.2a and Figure 6.3a).

In Figure 6.2, the shock wave has an initial curvature radius of 130 mm. By the time the shock enters the viewing window, reflected shocks have already emerged on the shock front and shear layers are present. As the shock progresses within the window region, the reflected shocks develop further, the height of the Mach stem increases, and the reflected shocks eventually intersect the channel walls and are reflected (Figure 6.2e).

On the other hand, there is no evidence of kinks or reflected shocks on the shock front when the shock wave in Figure 6.3, which had an initial curvature radius of 250 mm, enters the viewing window. In this case, as the shock progresses within the window region, compressions gradually coalesce in the region between the curved and straight shock segments and kinks are formed on the shock front (Figure 6.3e). In Figure 6.3f, which depicts the shock wave just prior to the interaction of the eventual triple points with the channel walls, the beginning of reflected shocks is apparent, immediately behind the shock front.

From the numerical investigation, the impact of the constraints imposed by the facility on possible shock Mach numbers and profiles was ascertained. It would not be possible to capture, with only one slit shape, the evolution of the shock profile from the state shown in Figure 6.3a to the state shown in Figure 6.2e. As demonstrated in Figure 6.2 and 6.3, either

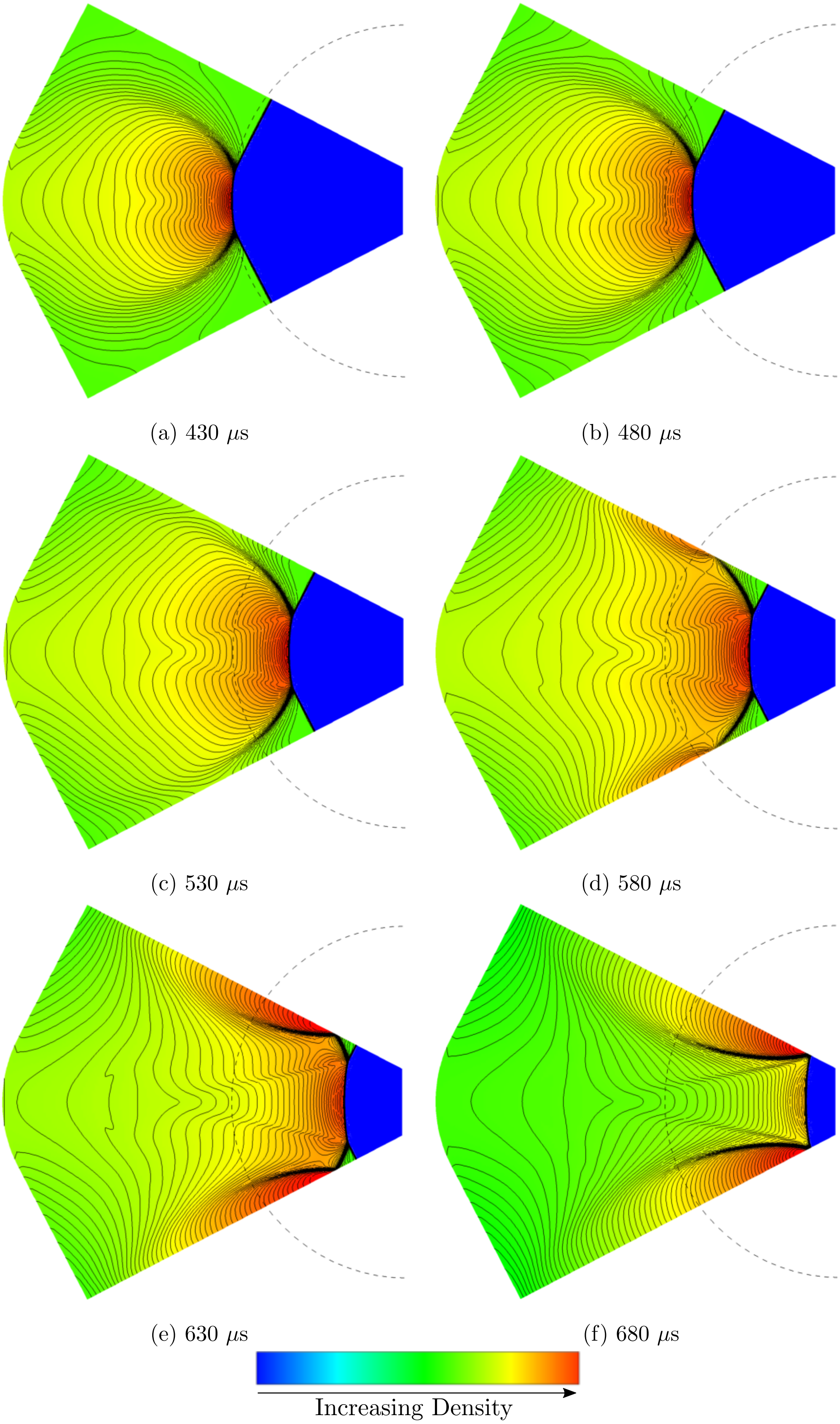

(a) 430 μs (b) 480 μs

(c) 530 μs (d) 580 μs

(e) 630 μs (f) 680 μs

Figure 6.2: Propagation of a shock wave with an initial curvature radius and Mach number of 130 mm and 1.3. The dashed circles represent the facility's window frame.

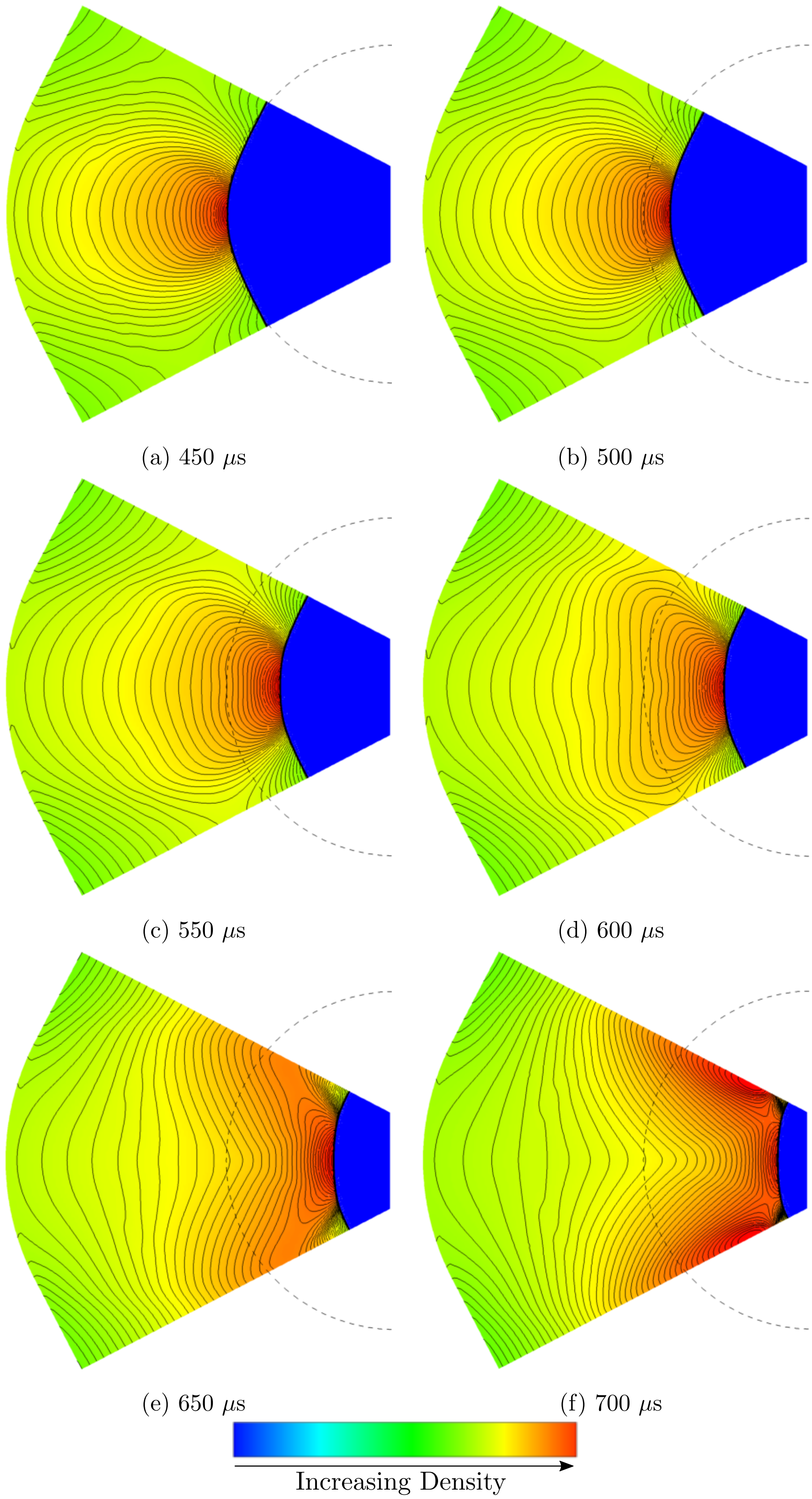

Figure 6.3: Propagation of a shock wave with an initial curvature radius and Mach number of 250 mm and 1.3. The dashed circles represent the facility's window frame.

the initial development of the kinks and reflected shocks could be captured, by generating a shock wave with a larger initial curvature radius. Alternatively, the subsequent growth and development of the reflected shocks and shear layers could be captured, by generating a shock wave with a smaller curvature radius. Based on these results, two distinct slit profiles were specified so that high-speed images of the complete evolution of the shock profile could be obtained over the range of experiments. Details of these slits are given in Table 6.1, while engineering drawings for the corresponding profile and side propagation plates can be found in Appendix B. In Table 6.1, the radius and length measurements correspond to the inner face of the slit.

Table 6.1: Details of the slit profiles specified for the experimental tests

	Wall convergence angle [°]	**Radius of cylindrical segment [mm]**	**Length of straight segment [mm]**	**Height [mm]**	**Width [mm]**
Slit 1	55	145	141	398	96
Slit 2	55	215	109	405	89

6.2 Results

Two sets of experiments were conducted for shock waves with various Mach numbers. In each set of tests, the facility was assembled with the profile and side propagation plates corresponding to Slit 1 and Slit 2, in Table 6.1, respectively. A summary of the tests that were performed is given in Table 6.2. To ensure the integrity of the shock profile, it was imperative that any fragments of diaphragm that may have been trapped in the slit or shock tube were removed in-between each test. This was because the shock wave would interact with these fragments and when it exited the slit, undesired disturbances would be present on the shock front. For each test, high-speed images of the shock progression were captured using schlieren flow visualization, with the knife edge oriented horizontally. The camera was triggered 300 μs after the shock wave had passed the second pressure transducer, embedded in the wall of the shock tube. Images were then taken at a frame rate of 42 000 fps, which corresponded to one frame every 24 μs.

Schlieren images obtained from the experiments with Slit 1 and Slit 2 are presented in Figure 6.4 and 6.5, and Figure 6.6 and 6.7, respectively. The results shown are for the shock Mach numbers at the ends of the range tested in each set of experiments. This facilitates an evaluation of the influence of the shock Mach number on the evolution of the shock profile.

Table 6.2: Summary of experimental tests that were conducted

Test No.	Curvature Radius of Slit [mm]	Diaphragm Thickness [µm]	Burst Pressure [kPa]	Mach Number of Shock Wave
1	215	100	290	1.34
2	215	25	70	1.15
3	215	50	160	1.27
4	145	25	90	1.19
5	145	100	300	1.33
6	145	50	160	1.27

Such an evaluation is possible because the scale of the images was consistent across all tests. For each frame, the time refers to the time that has passed since the shock wave exited the slit. The Mach number of the planar shock wave generated in the shock tube was determined from the oscilloscope reading, and the distance between the second pressure transducer and the slit exit is known. Using this, the time delay and the fact that a frame was taken every 24 μs, the time corresponding to each frame was obtained.

6.2.1 Slit 1

The results for an initial shock Mach number of 1.19 and 1.33 are shown in Figure 6.4 and 6.5, respectively. For these tests, the required shock profile was generated by using the existing facility in conjunction with Slit 1 in Table 6.1. It was assumed that when the shock wave passes through the slit, it assumes the curvature radius of the inner face of the slit, which in this case was 145 mm.

The shock wave moves from left to right. In Figure 6.4a and 6.5a, the shock wave is depicted just after it passes into the region where the viewing window is located. At this stage of the shock propagation, two kinks and the initial onset of reflected shocks are evident on the shock front. As the shock progresses, the reflected shocks grow and propagate further behind the shock front. In addition, the height of the Mach stem increases. This implies that the triple points of the Mach-reflection pair follow a divergent trajectory, away from the axis of symmetry. Finally, in Figure 6.4c - 6.4e, and in Figure 6.5b - 6.5e, shear layers are clearly apparent.

The most discernible difference between the two cases is that the height of the Mach stem of the shock wave with the higher initial Mach number (Figure 6.5) increases to a greater

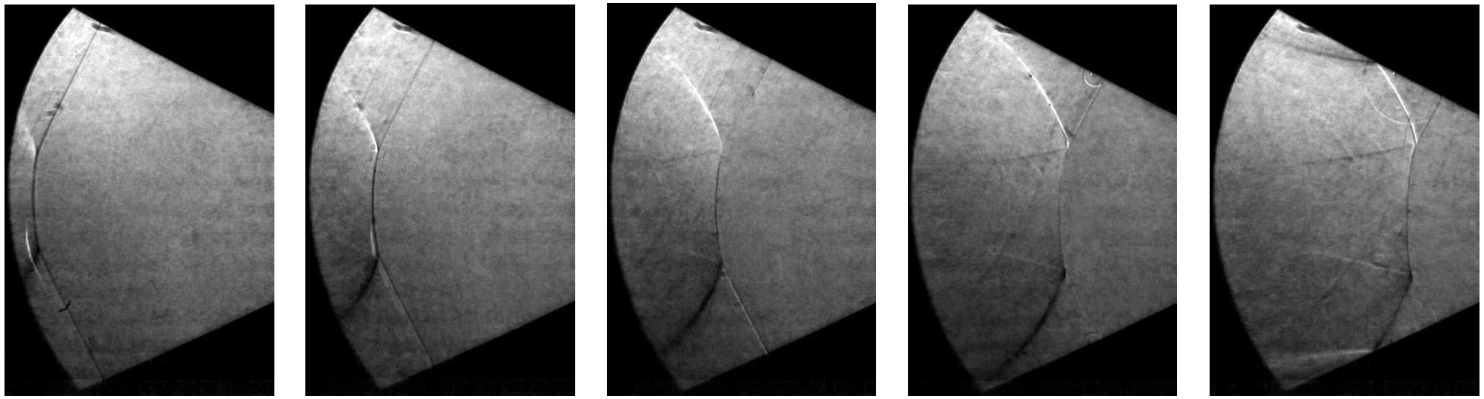

(a) 497 μs (b) 544 μs (c) 592 μs (d) 640 μs (e) 687 μs

Figure 6.4: Schlieren images of the propagation of a shock wave with an initial curvature radius and Mach number of 145 mm and 1.19. The time is measured with respect to the time that the shock wave passed through the slit.

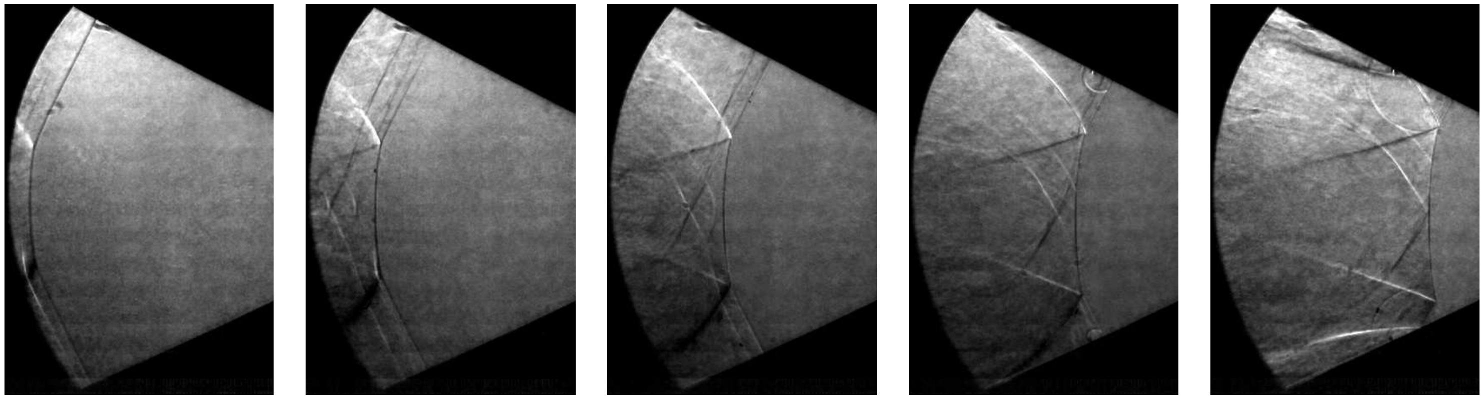

(a) 430 μs (b) 478 μs (c) 526 μs (d) 573 μs (e) 621 μs

Figure 6.5: Schlieren images of the propagation of a shock wave with an initial curvature radius and Mach number of 145 mm and 1.33. The time is measured with respect to the time that the shock wave passed through the slit.

extent. This suggests that for higher shock Mach numbers, the triple points propagate at a steeper trajectory angle. However, this would need to be confirmed with a quantitative analysis. Additionally, the reflected shocks and shear layers appear to be stronger than for the lower shock Mach number (Figure 6.4).

6.2.2 Slit 2

The results for an initial shock Mach number of 1.15 and 1.34 are shown in Figure 6.6 and 6.7, respectively. For these tests, the required shock profile was generated by using the existing facility in conjunction with Slit 2 in Table 6.1. As for the previous set of tests, over here too, it was assumed that when the shock wave passes through the slit, it assumes the curvature radius of the inner face of the slit, which in this case was 215 mm.

The shock wave moves from left to right and the first frame in Figure 6.6 and 6.7 depicts the shock wave just after it has passed into the region where the viewing window is located. For this slit, when the shock wave enters the window region, no disturbances can be distinguished on the shock front. As the shock progresses, the compressions behind the shock front gradually coalesce in the region in-between the curved and straight shock segments. This is particularly apparent in Figure 6.7. Eventually, the compressions steepen into reflected shocks immediately behind the shock front. As shown in Figure 6.6e and 6.7e, this occurs just before the triple points intersect the channel walls, and the shock wave passes out of the view of the window.

The most obvious distinction between these two results is that for the shock wave with the higher initial Mach number (Figure 6.7), the triple points of the Mach-reflection pair intersect the walls sooner. Once again, this implies that the triple points follow a steeper trajectory when the shock Mach number is higher. This result agrees with the predictions of the CFD discussed in section 5.2.1.2.

6.2.3 Comment on experiment results

In Figure 6.5b and 6.7b, an additional wave is visible at some distance behind the primary shock front. As the primary shock wave propagates through the chamber, this wave follows behind and eventually catches up to it.

In order to gain insight into the source of this secondary wave, a brief numerical simulation was performed so that the propagation of the shock wave from the shock tube, through the slit and into the propagation chamber could be evaluated. A 3-dimensional model comprising

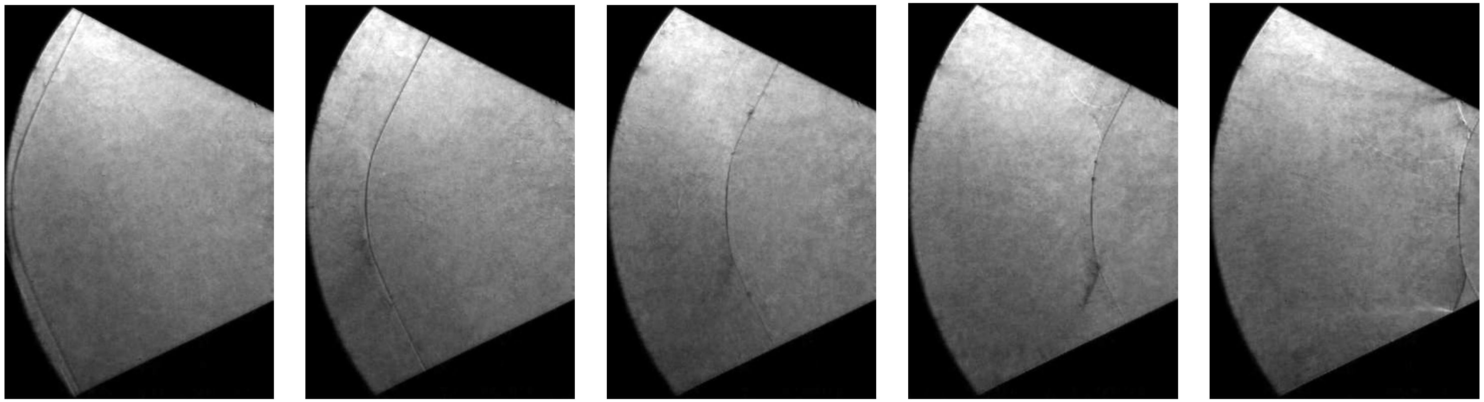

(a) 488 μs (b) 559 μs (c) 630 μs (d) 702 μs (e) 773 μs

Figure 6.6: Schlieren images of the propagation of a shock wave with an initial curvature radius and Mach number of 215 mm and 1.15. The time is measured with respect to the time that the shock wave passed through the slit.

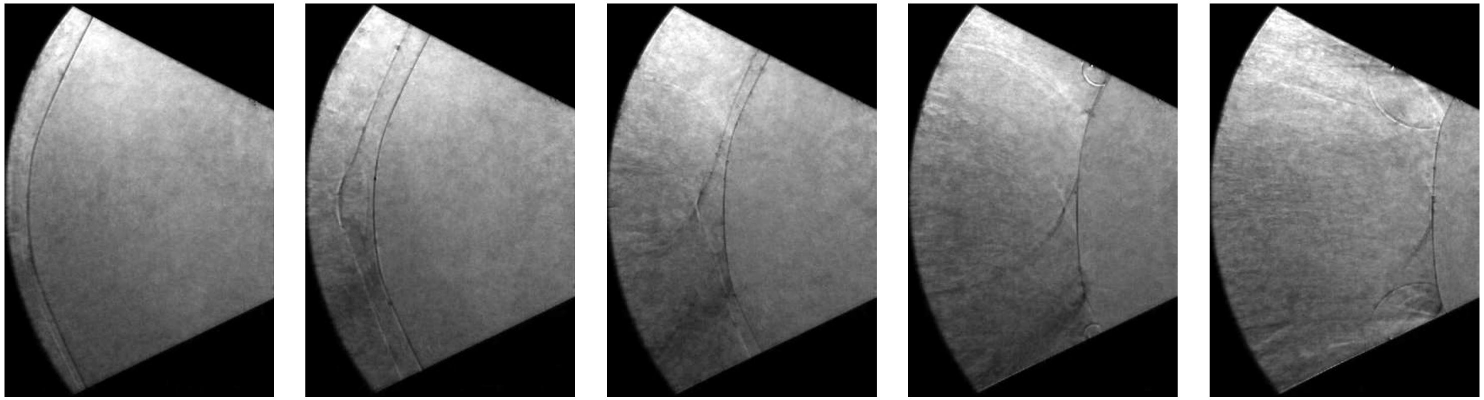

(a) 434 μs (b) 481 μs (c) 529 μs (d) 577 μs (e) 624 μs

Figure 6.7: Schlieren images of the propagation of a shock wave with an initial curvature radius and Mach number of 215 mm and 1.34. The time is measured with respect to the time that the shock wave passed through the slit.

a short section, 150 mm in length, at the end of the shock tube, the slit, and the propagation chamber, was created. A basic mesh was generated to reduce the computation time and the propagation of the shock wave was analysed using the settings described in section 4.1.3. The results obtained from this simulation are shown in Figure 6.8.

The pressure contours in Figure 6.8 illustrate the generation and subsequent propagation of a shock wave with a curvature radius of 215 mm, when a planar shock wave with a Mach number of 1.15 is passed through the slit at the end of the shock tube. After the shock wave exits the slit, it is reflected by the back wall of the propagation chamber. This initiates a system of transverse waves that progressively decay as the reflected shock is reflected back and forth, in-between the side walls of the propagation chamber. As the shock wave propagates within the chamber, it increases in strength and as a result, there is a corresponding increase in the acoustic velocity of the air behind the shock wave. Therefore, the system of transverse waves that follow behind the primary shock wave, eventually catch up to it. This is evident in Figure 6.8d - 6.8f. From these results, it can be deduced that the secondary wave visible in the schlieren images from the experiments must be one of these transverse waves.

6.3 Comparison with CFD

In this section, the results from the experiments and corresponding numerical simulations are compared.

To facilitate a direct comparison of the shock propagation in the experiment and CFD, a composite image of its progression was generated for each experimental and numerical test. For an experimental test, this was achieved by superimposing successive frames over each other. The resulting image that was obtained in this way for experiment test 4 and test 2 is shown in Figure 6.9a and 6.10a, respectively. Since schlieren images capture density gradients in the fluid and the knife edge was oriented horizontally in the experiments, contours of the density gradient in the y-direction were generated for the corresponding CFD at the same times that the frames in the experiment were taken. The composite image of the shock progression in the CFD was then obtained by superimposing successive density contours over one another. This is shown for the numerical simulations corresponding to experiment test 4 and test 2 in Figure 6.9b and 6.10b, respectively. In Figure 6.9b and 6.10b, the portion of the propagation chamber before the viewing window has been removed from the resulting image.

In Figure 6.9 and 6.10, the shock wave moves from left to right. For both tests, there is agreement between the experiment and CFD with respect to the general evolution of the

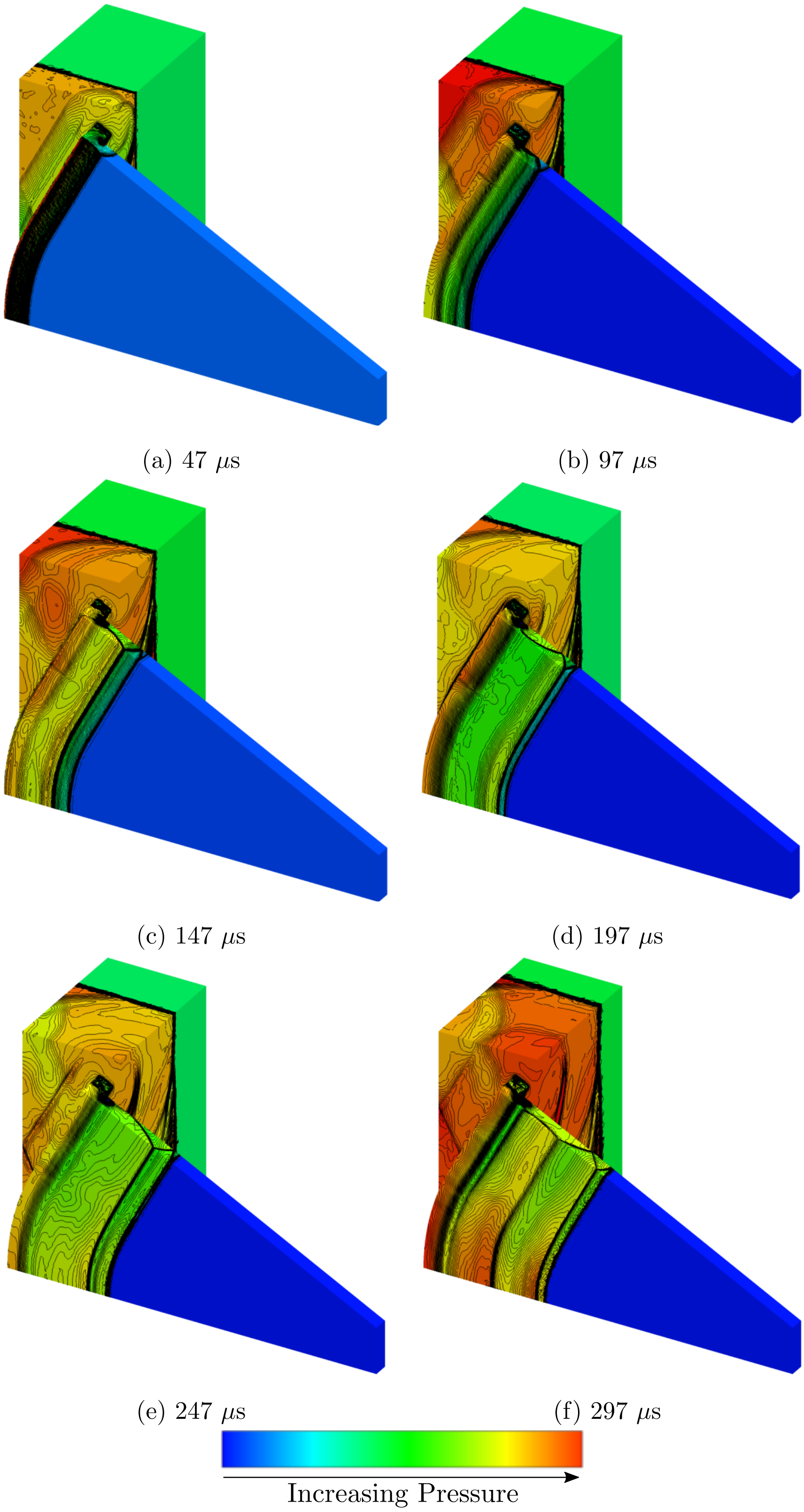

(a) 47 μs

(b) 97 μs

(c) 147 μs

(d) 197 μs

(e) 247 μs

(f) 297 μs

Figure 6.8: 3D pressure contours of the generation and subsequent propagation of a shock wave with an initial Mach number and curvature radius of 1.15 and 215 mm. The time is measured with respect to the time that the shock wave passed through the slit.

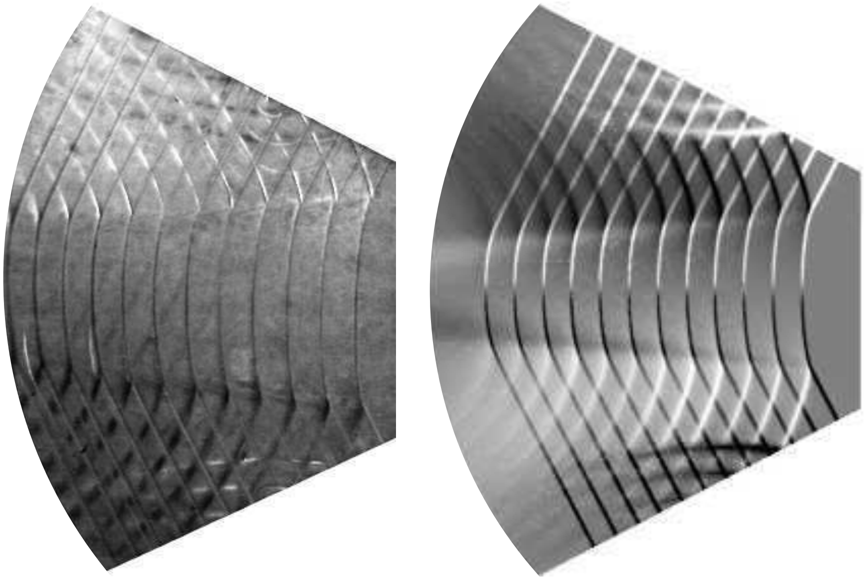

(a) Successive schlieren images from the experiment

(b) Successive density-gradient contours for the corresponding CFD

Figure 6.9: Composite image of the progression of a shock wave with an initial curvature radius and Mach number of 145 mm and 1.19

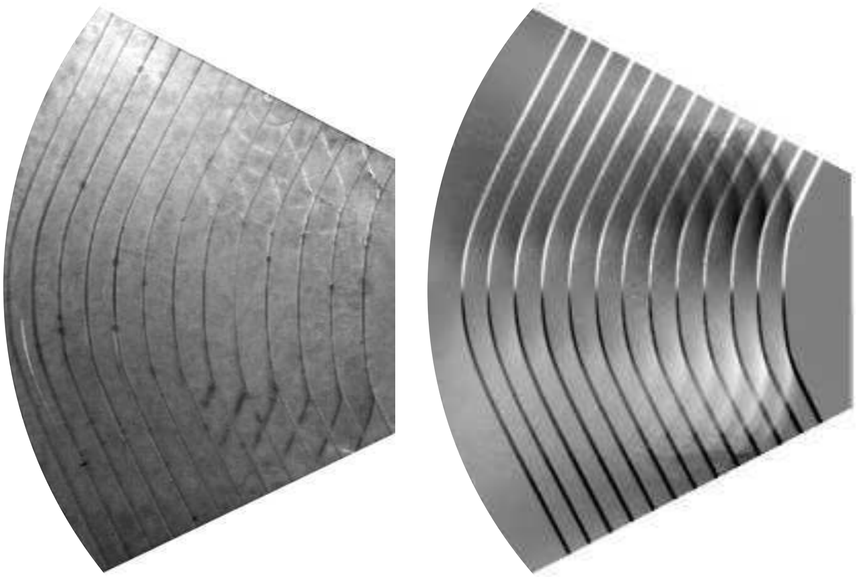

(a) Successive schlieren images from the experiment

(b) Successive density-gradient contours for the corresponding CFD

Figure 6.10: Composite image of the progression of a shock wave with an initial curvature radius and Mach number of 215 mm and 1.15

shock profile. Specifically, for the case demonstrated in Figure 6.9, in both the experiment and CFD, when the shock wave enters the viewing window, kinks are present on the shock front and the reflected shocks develop as it progresses within the window region. Similarly, in Figure 6.10, in both the experiment and CFD, when the shock wave enters the viewing window, the shock front is smooth and continuous and as the shock propagates within the window region, compressions gradually steepen into reflected shocks.

However, certain disparities are conspicuous. Firstly, considering the first position of the shock wave, just after it has entered the viewing window, it is apparent that the distance of the shock from the start of the window is greater in the CFD than in the experiment. In section 5.2.1.1, it was shown that when the initial curvature radius of the shock wave is smaller, as it propagates, it increases in strength to a greater extent than a shock with a larger curvature radius. This implies that shock waves with larger curvature radii would propagate at a slower velocity. It was assumed that the shock waves generated in the experiment take on the curvature radius of the inner face of the slit. It is possible that the curvature radius of the shock wave generated is actually larger than this and therefore, it moves slower and does not propagate as far as was expected. Hence, the position of the first shock wave in Figure 6.9 and 6.10 is further ahead in the CFD than in the experiment.

Although the entire length of the propagation chamber is shown in the composite CFD images, this is not the case in the images corresponding to the experiments. This was due to the limited resolution attainable given the specified camera settings. Therefore, since the right end of the propagation chamber is not shown in the experimental images, the last position of the shock wave in the CFD and the experiment cannot be compared.

Lastly, the distance between successive shock positions seems to be increasing in the experiment, whereas it is approximately constant in the CFD. This was investigated further by comparing the positions of the shock wave in the CFD and experiment, at corresponding times. This is shown in Figure 6.11 and 6.12 for the tests conducted with the two different slit profiles. In the plots in Figure 6.11 and 6.12, the position of the shock wave in the CFD and in the experiment is represented by the solid lines and filled circles, respectively. In the CFD, the position of the shock wave, at each time, was found using the method described in section 4.2. For the experiments, the position of the shock wave in each frame was obtained by taking several points along the length of the shock front. In order to evaluate the corresponding position of the shock wave in the experiment and CFD, the pixel coordinates of the shock wave in the experiment had to be transformed into real coordinates, with respect to a datum common with the CFD. This was achieved using the method detailed in Appendix E and the center of the inner face of the slit was chosen as the common datum.

Considering the temporal change in the position of the shock wave in the experiment relative to that in the CFD, it is clear that although the shock wave in the experiment is initially behind the shock wave in the CFD, it eventually catches and overtakes it. This result supports the previous observation that the distance between successive shock positions in the

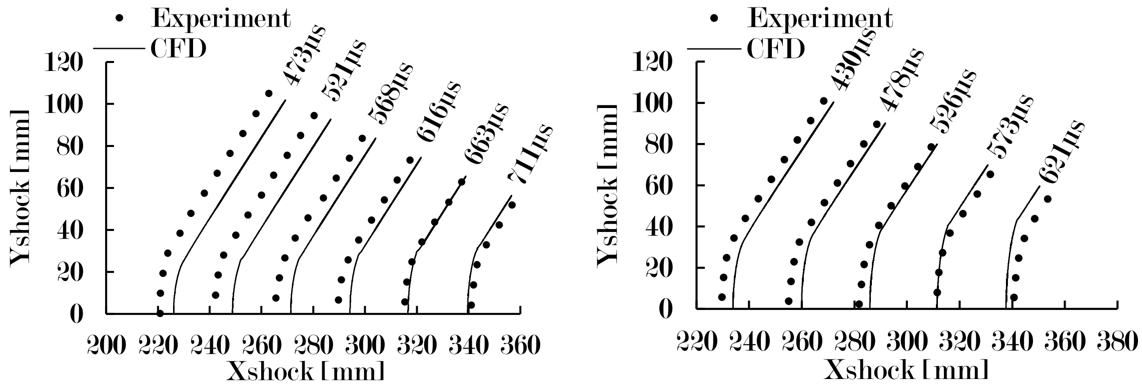

(a) Initial Mach number: 1.19

(b) Initial Mach number: 1.33

Figure 6.11: Comparison, at corresponding times, of the shock positions in the experiment and CFD. The shock wave has an initial curvature radius of 145 mm.

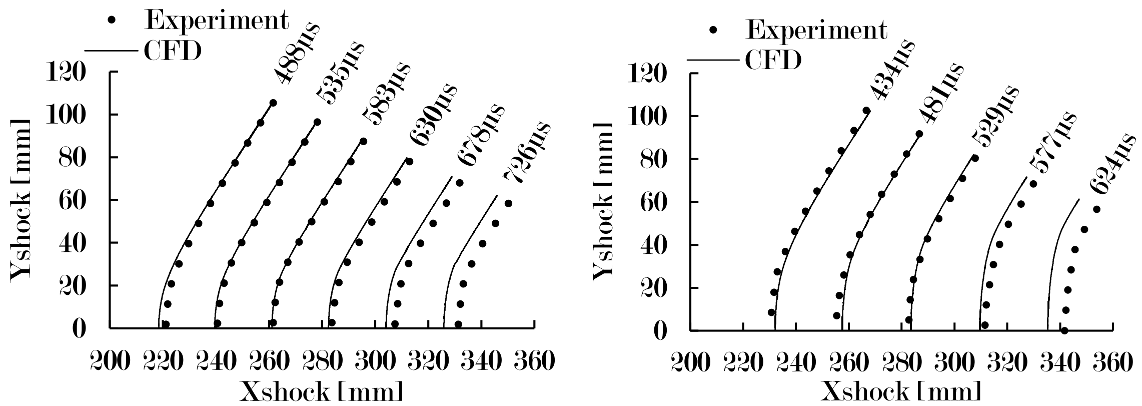

(a) Initial Mach number: 1.15

(b) Initial Mach number: 1.34

Figure 6.12: Comparison, at corresponding times, of the shock positions in the experiment and CFD. The shock wave has an initial curvature radius of 215 mm.

experiment is increasing over time. This suggests that the shock wave in the experiments is accelerating.

To ascertain whether this is indeed the case, the temporal variation of the Mach number of the shock wave in the experiments was compared to that predicted by the CFD. This is shown for all the tests that were carried out with slit 1 and slit 2, in Figure 6.13a and 6.13b, respectively. At each time, the velocity of the shock wave was determined from its position at the axis of symmetry. The method used to calculate the velocity of the shock wave is described in Appendix E. The plots in Figure 6.13 verify that the shock wave in the experiments is accelerating, since its Mach number increases over time. In comparison, the variation of the Mach number of the shock wave corresponding to the CFD is essentially negligible. The reason for this discrepancy becomes clear upon consideration of the results of the 3D numerical simulation presented in Figure 6.8. Clearly, as successive transverse waves catch up to the primary shock front, it is reinforced, causing it to become stronger over time and accelerate.

The impact of the transverse waves on the primary shock front was not observed in previous experiments with the facility. However, in those experiments, the profile of the shock waves generated, comprised a cylindrical arc with a radius of 450 mm. In the current tests, shock waves with a curvature radius of 145 mm and 215 mm were generated. The results of the numerical component of this investigation showed that when the curvature radius of the shock wave is smaller, there is a greater increase in its strength over time. Accordingly, the acoustic velocity of the air behind the shock is greater. Therefore, since the shock waves in the previous experiments had a curvature radius more than two times the curvature radius of the shocks in the current experiments, it is possible that the transverse waves did not catch up to the primary shock front because the acoustic velocity behind the shock was small enough.

Various numerical simulations corresponding to experimental test 4 were performed for shock waves with initial Mach numbers ranging from 1.19 - 1.33. In each case, the temporal variation of the shock Mach number was determined and compared with the Mach number of the shock wave in the experiment. This is illustrated in Figure 6.14. It is evident that at successive times, the Mach number of the shock wave in the experiments correlates with a different CFD line. For each experimental data point in Figure 6.14, the Mach number of the shock wave on the corresponding CFD line was obtained and a line was fitted through the resulting set of points. This is the dashed line shown in Figure 6.14. There is excellent agreement between this simulated Mach number and the shock Mach numbers obtained from the experiment. In addition, this provides insight into the acceleration of the shock wave over time, which as can be seen, is approximately constant.

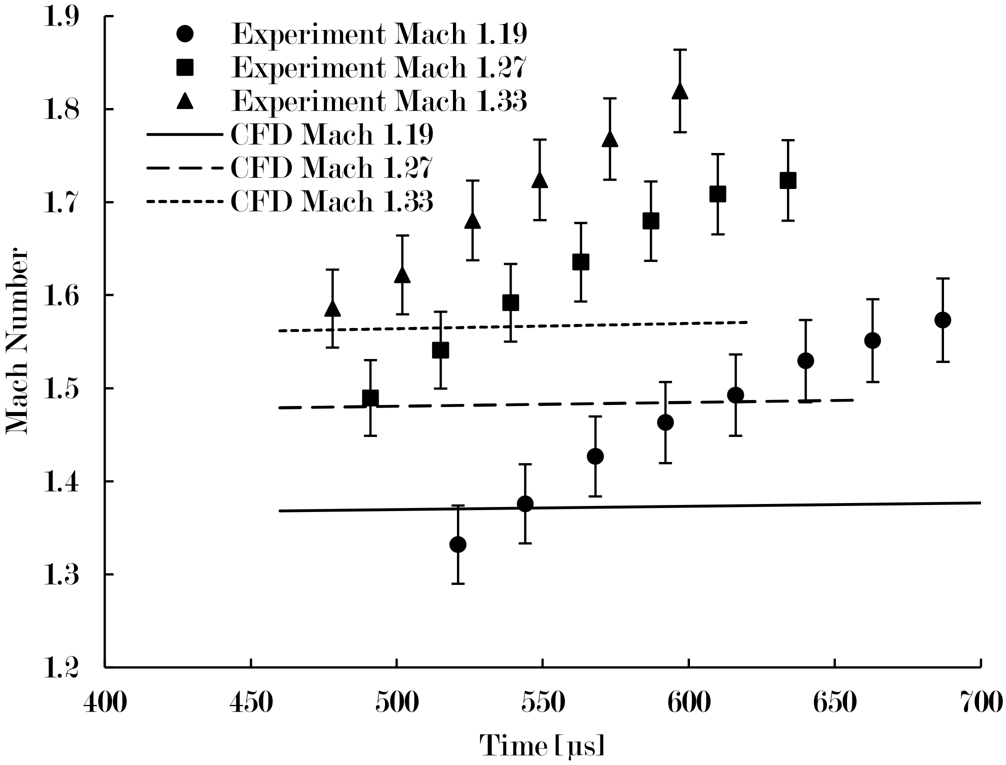

(a) Curvature radius: 145 mm

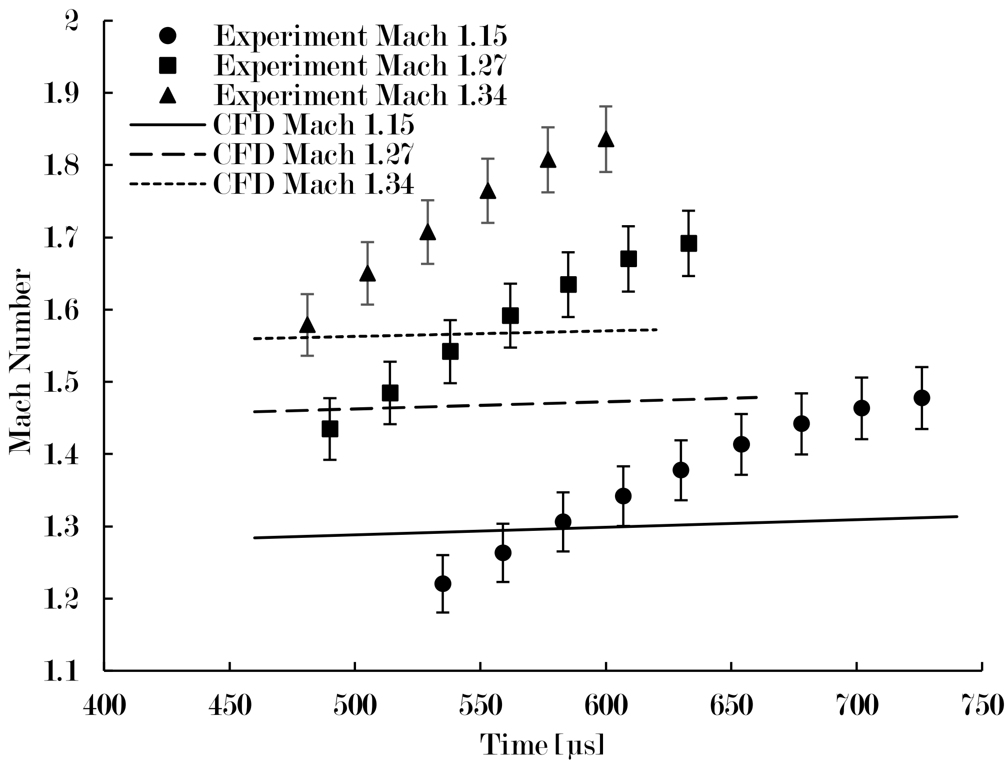

(b) Curvature radius: 215 mm

Figure 6.13: Comparison of the temporal variation of the shock Mach number in the experiment with the CFD, for shock waves with different initial curvature radii.

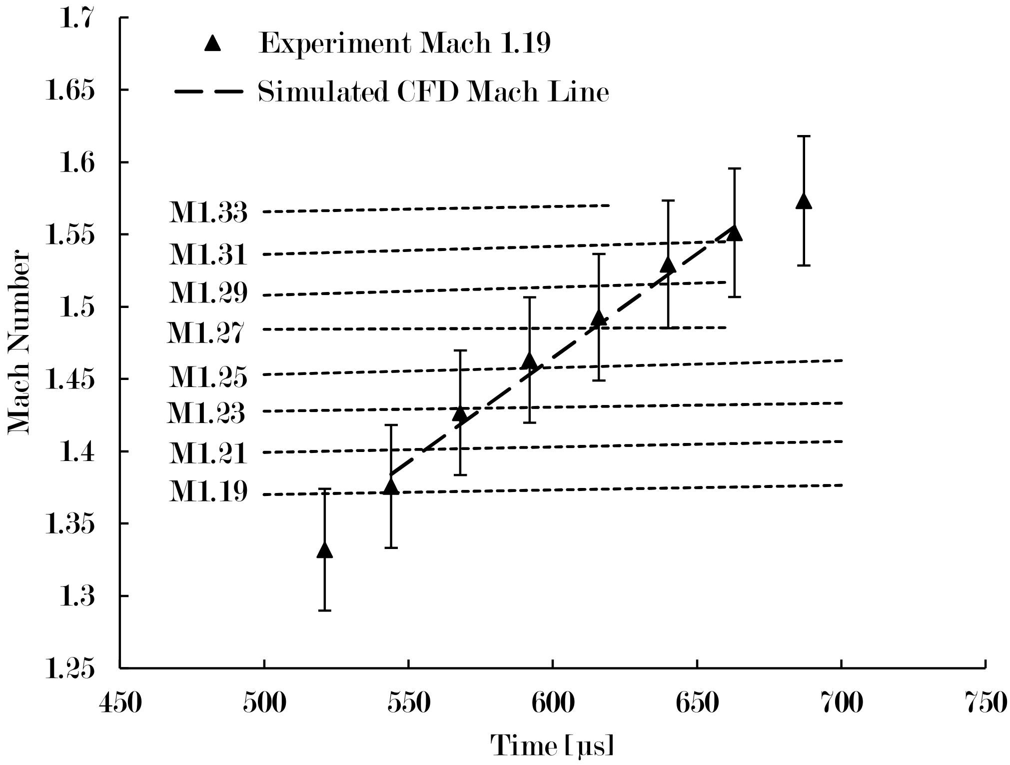

Figure 6.14: Comparison of the temporal variation of the shock Mach number in the experiment with the simulated CFD Mach number. The shock waves have an initial curvature radius of 145 mm.

7 Conclusions

The propagation in a converging channel, of shock waves with initial profiles comprising a cylindrical arc in-between two straight segments was evaluated through various numerical simulations and experimental tests. A summary of the conclusions obtained from the results of these investigations follows.

7.1 Numerical results

The characteristic features of the change in the shock profile over the duration of its propagation were described. In general, the curved segment of the shock front is distorted and flattened as the shock wave converges to its focus. As the shock propagates away from the focus, two kinks develop on the shock front, from which reflected shocks emerge. This results in a configuration resembling a symmetrical pair of Mach reflections. The triple points of the Mach-reflection pair were found to follow a divergent trajectory, away from the axis of symmetry.

The physical mechanism responsible for the development of the reflected shocks was elucidated by an evaluation of the temporal variation of the pressure distribution behind the shock wave. This showed that the pressure behind the curved shock segment increases over time, while the pressure behind the straight segments are essentially constant. Compressions propagate along the shock front towards the straight shock segments to correct this pressure imbalance. As the pressure behind the curved shock segment increases, subsequent compressions propagate at a greater velocity and eventually, they coalesce into reflected shocks.

As a result of the increase in the pressure behind the curved shock segment with time, this portion of the shock front is distorted and flattened. When the angle at which the channel walls converge is higher, the curvature of the shock wave at the start of its propagation and consequently, the overall distortion of the curved shock segment, is greater.

The initial Mach number and curvature radius of the shock wave, as well as the wall angle of the converging channel was varied in the numerical simulations. This enabled the influence of these parameters on the characteristic aspects of the evolution of the shock profile to be identified. It was found that,

- When the wall convergence angle is lower, the initial curvature radius is smaller and the shock Mach number is higher, the shock wave arrives at its focus sooner. The reason for this was that under these conditions, the rate at which the shock increases in strength, and hence accelerates, is greater.
- When the wall convergence angle is lower, the initial curvature radius is larger, and the shock Mach number is higher, the trajectory angle of the triple points is greater. As a result, the triple points intersect the walls of the channel earlier. The implication of this is that the likelihood of reflected shocks developing within the duration of the shock's propagation in the channel is reduced. This effect is further exacerbated in cases where the wall convergence angle is lower and the initial curvature radius is larger by the fact that, under these conditions, the rate at which the reflected shocks are formed is slower and therefore, the triple points intersect the channel walls before the reflected shocks can completely develop.

7.2 Experimental results

Two profile plates with distinct slits were manufactured and these were used in conjunction with the existing facility, to produce shock waves with an initial curvature radius of 145 mm and 215 mm. Various experimental tests were conducted with each slit for shock Mach numbers ranging from 1.15 - 1.34. In the schlieren images obtained from experiments with these two slits, the complete evolution of the shock front, from a smooth, continuous profile to a symmetrical pair of Mach reflections was captured.

As the shock wave propagates in the converging channel, the height of the Mach stem increases. A qualitative evaluation of the results at different shock Mach numbers showed that when the initial Mach number of the shock wave is higher, the increase in the height of the Mach stem with time is greater. This result agrees with the CFD, in which it was found that for higher shock Mach numbers, the trajectory angle of the triple points is greater.

For all the tests, the general evolution of the shock wave profile was the same in the experiments and corresponding numerical simulations. However, in the experiments, the distance between successive shock positions increased over time, whereas in the CFD, it did not. Furthermore, when the shock wave first became visible in the facility's viewing window, it had not progressed as far as had been predicted by the CFD. It was deduced from this that the initial curvature radius of the shock wave produced by the facility was larger than assumed.

In the images obtained from the various tests that were carried out, a secondary wave can be seen some distance behind the primary shock wave. This was identified as one of the transverse waves that are generated, from the initial reflection of the shock wave by the side wall of the propagation chamber, upon exiting the slit. As the shock progresses, the secondary wave follows and eventually catches up to the primary shock front. The impact of this was demonstrated with a comparison of the temporal variation of the Mach number of the shock wave in the experiment to that in the CFD. The Mach number of the shock wave in the CFD was approximately constant, while in the experiments, the shock accelerates as a result of being reinforced by the transverse waves.

8 Recommendations

In this research, the changes in profile that a curved shock wave experiences when it propagates in a converging channel were evaluated. Only shock waves with one type of profile were investigated; this being shock waves with initial profiles comprising a cylindrical arc placed in-between two straight segments. Furthermore, a significant mismatch was found between the experimental and numerical results. Therefore, there exists scope for improvement and further analysis. This includes:

- In the numerical component of the investigation, it was found that the interaction of the curved and straight shock segments resulted in the development of reflected shocks on the shock front, in the region where these two segments meet. The development of reflected shocks has also been observed on a shock wave with an initially parabolic front, generated from a collapsing parabolic wall. Extending the current analysis to these waves, which in addition to propagating uniquely, comprise a different and singular shape, would supplement the conclusions obtained here. Furthermore, it would provide further insight into the phenomenon of the development of Mach reflections on an initially continuous shock front.
- The propagation of the shock wave in the experiments was captured with schlieren images. Therefore, subsequent comparisons with corresponding numerical simulations was limited to the information that could be obtained from these images. In the CFD component of the investigation, the various aspects involved in the evolution of the shock profile was evaluated by examining how the pressure immediately behind the shock wave changes with time. It is possible to exchange one of the window plates of the facility with another plate, in which pressure transducers are embedded along a line coincident with the propagation chamber's axis of symmetry. This would enable pressure measurements to be taken during the experiments, from which critical results gleaned from the CFD could be validated.
- In the images obtained from the experiments, a secondary wave that followed behind the primary shock was observed. Over time, this secondary wave caught up to the

primary shock front and caused it to accelerate. When the shock wave exits the slit, it is reflected in-between the side walls of the propagation chamber. This results in a system of transverse waves that follow behind the primary shock front. The secondary wave seen in the experimental images is one of these transverse waves. To achieve optimal agreement between the experiment and CFD, the facility needs to be modified to mitigate and ideally eliminate the impact of these transverse waves on the primary shock. In the current layout, after the shock wave passes through the slit, it is turned through a ninety-degree corner. This results in the formation of a high-pressure region at the outer corner. During the preliminary design of the facility, the shape of this corner was evaluated. It was found that when the outer corner was rounded, this high-pressure region was diminished. It is possible that this modification would have the effect desired here. This is due to the fact that it could decrease the likelihood of the transverse waves catching up to the primary shock. Therefore, it should be investigated in this respect.

References

Anderson, J. (2003). *Modern compressible flow: with Historical perspective* (3rd). New York, NY: McGraw-Hill.

Ben-Dor, G. (2007). *Shock wave reflection phenomena* (2nd). Berlin, Germany: Springer.

Chisnell, R. (1957). The Motion of a Shock Wave in a Channel, with Applications to Cylindrical and Spherical Shock Waves. *Journal of Fluid Mechanics*, *2*(3), 286–298. doi:10.1017/S0022112057000130

Glass, I. I. & Sharma, S. P. (1976). Production of Diamonds from Graphite Using Explosive-Driven Implosions. *AIAA Journal*, *14*(3), 402–404. doi:10.2514/3.61376

Gray, B. J. (2014). *On the propagation and reflection of curved shock waves* (PhD Thesis, University of the Witwatersrand, Johannesburg, South Africa).

Grönig, H. (1986). Shock wave focusing phenomena. In D. Bershader & R. Hanson (Eds.), *Proceedings of the fifteenth international symposium on shock waves and shock tubes* (pp. 43–56). Berkeley, CA: Stanford University Press.

Kleine, H. (2001). Measurement techniques and diagnostics. In G. Ben-Dor, O. Igra & T. Elperin (Eds.), *Handbook of shock waves* (Chap. 5.1, pp. 683–740). San Diego, CA: Academic Press.

Lax, P. (1954). Weak Solutions of Nonlinear Hyperbolic Equations and their Numerical Computation. *Communications on Pure and Applied Mathematics*, *7*(1), 159–193. doi:10.1002/cpa.3160070112

Liepmann, H. & Roshko, A. (2001). *Elements of gas dynamics*. Mineola, NY: Dover Publications.

Ndebele, B. B. (2017). *The Diffraction , reflection and propagation of cylindrical shock wave segments* (PhD Thesis, University of the Witwatersrand, Johannesburg, South Africa).

Nishida, M. (2001). Shock tubes and tunnels: Facilities, instrumentation, and techniques. In G. Ben-Dor, O. Igra & T. Elperin (Eds.), *Handbook of shock waves* (Chap. 4.1, pp. 553–585). San Diego, CA: Academic Press.

Payne, R. (1957). A Numerical Method for a Converging Cylindrical Shock. *Journal of Fluid Mechanics*, *2*(2), 185–200. doi:10.1017/S0022112057000063

Perry, R. & Kantrowitz, A. (1951). The Production and Stability of Converging Shock Waves. *Journal of Applied Physics*, *22*(7), 878–886. doi:10.1063/1.1700067

Settles, G. (2001). *Schlieren and shadowgraph techniques: Visualizing phenomena in transparent media*. Berlin, Germany: Springer.

Skews, B., Gray, B. & Paton, R. (2015). Experimental Production of Two-Dimensional Shock Waves of Arbitrary Profile. *Shock Waves*, *25*(1), 1–10. doi:10.1007/s00193-014-0541-4

Skews, B. & Kleine, H. (2007). Flow Features Resulting from Shock Wave Impact on a Cylindrical Cavity. *Journal of Fluid Mechanics*, *580*, 481–493. doi:10.1017/S0022112007005757

Skews, B., Komljenovic, I. & Sprich, T. (2008). Generation of unsteady flows from rapidly moving boundaries. In *6th international conference on heat transfer, fluid mechanics and thermodynamics* (July). Pretoria, South Africa: HEFAT 2008, ISBN 978-1-86854-691-6.

Sod, G. (1977). A Numerical Study of a Converging Cylindrical Shock. *Journal of Fluid Mechanics*, *83*(4), 785–794. doi:10.1017/S0022112077001463

Takayama, K. & Saito, T. (2004). Shock Wave/Geophysical and Medical Applications. *Annual Review of Fluid Mechanics*, *36*(1), 347–379. doi:10.1146/annurev.fluid.36.050802.121954

Whitham, G. B. (1957). A New Approach to Problems of Shock Dynamics Part I Two-dimensional Problems. *Journal of Fluid Mechanics*, *2*(2), 145–171. doi:10.1017/S002211205700004X

Appendix A Instructions for Assembling and Disassembling the Apparatus

The general procedure for assembling and disassembling the facility used to achieve shock waves with the various required profiles follows. During these processes (assembly or disassembly), the utmost care must be taken to ensure the facility's windows are not scratched or damaged in any manner.

A.1 Assembling the Facility

1. Prepare two large tables. On one table (which will be referred to as the parts table), lay out the facility's component plates. Position the other table (which will be referred to as the assembly table) near the exit of the shock tube.
2. Position the overhead gantry so that the facility can be moved from the assembly table to the shock tube exit.
3. Line both sides of the side, top and bottom propagation plates, as well as the flange at the exit of the shock tube with paper gasket, 0.4 mm thick. Use double sided tape to adhere the gasket to the plates. Ensure that the gasket does not protrude at edges that will be exposed to the flow.
4. Clean the windows with acetone and a microfibre cloth.
5. Place the large outer plate with its inner face facing upwards on four blocks. The plate must be positioned such that none of the bolt holes are impeded by the blocks.
6. Place the side, top and bottom propagation plates on top of the outer plate. Ensure that all bolt holes are aligned. Insert dowel pins in the provided holes to facilitate the alignment of these plates.

7. Once the propagation plates have been aligned with each other and the outer plate, use six M6 bolts to secure the top and bottom propagation plates to the side propagation plate.

8. Position the profile plate on top of the side propagation plate. Ensure that all bolt holes are aligned and that the back face of the slit is aligned with its corresponding face on the side propagation plate. If these faces do not lie flush with each other, the integrity of the shock wave profile will be compromised.

9. Insert two dowel pins in their corresponding holes in the profile plate. When the facility is transferred from the assembly table to the shock tube exit, these dowels are crucial for maintaining alignment between the profile plate and the rest of the facility.

10. Coat an O-ring cord, 4 mm in diameter and 604 mm in length, with grease, and insert it into the groove in the side of the profile plate.

11. Position the short outer plate adjacent to the profile plate.

12. After ensuring that all the bolt holes are aligned, clamp the plates together with seven M14 bolts.

13. Connect the hook of the overhead gantry to the tab on the large outer plate, and carefully raise the facility above the table and transfer it to the exit of the shock tube.

14. Secure the facility to the flange at the shock tube exit with seven M14 bolts. Ensure that all bolts have been torqued sufficiently.

15. Disconnect the hook of the overhead gantry from the tab on the large outer plate and raise the chain so that it is clear of the facility.

A.2 Disassembling the facility

1. Prepare two large tables. Position one table (which will be referred to as the disassembly table) near the exit of the shock tube. As the facility is disassembled, the plates will be laid out on the other table (which will be referred to as the parts table).

2. Position the overhead gantry so that the facility can be moved from the shock tube exit to the disassembly table.

3. Connect the hook of the overhead gantry to the tab on the large outer plate and raise the chain until it is just taut.

4. Loosen and remove the seven bolts securing the facility to the flange at the exit of the shock tube. Insert four temporary bolts through each corner of the profile plate to clamp the profile plate to the facility.

5. Carefully transfer the facility to the disassembly table and lower it onto four blocks on the table. The facility should be lowered with the large outer plate facing upwards. Ensure that access to the bolts is not impeded by the blocks.

6. Disconnect the hook of the overhead gantry from the tab on the large outer plate and raise the chain so that it is clear of the facility.

7. Remove the seven bolts which clamp the plates together, as well as the four temporary bolts that were used in step four.

8. Move the large outer plate to the parts table.

9. Remove the two dowel pins which were used to align the profile and side propagation plate.

10. Clamp the facility together with at least six temporary bolts and connect the hook of the overhead gantry to the tab on the short outer plate. Carefully turn the facility over so that it is now positioned on the disassembly table with the short outer plate facing upwards.

11. Remove the temporary bolts used in step ten and move the short outer plate to the parts table.

12. Remove the O-ring cord from the groove in the side of the profile plate.

13. Move the profile plate to the parts table.

14. Loosen and remove the six M6 bolts securing the top and bottom propagation plates to the side propagation plate.

15. Move the side, top and bottom propagation plates to the parts table.

Appendix B Engineering Drawings

In the experimental component of this investigation, shock waves with two distinct profiles were generated using the facility described in section 3.2. This necessitated the manufacture of a unique side propagation plate and profile plate corresponding to each profile. In this appendix, the engineering drawings that were produced for the parts that had to be manufactured are provided. This includes:

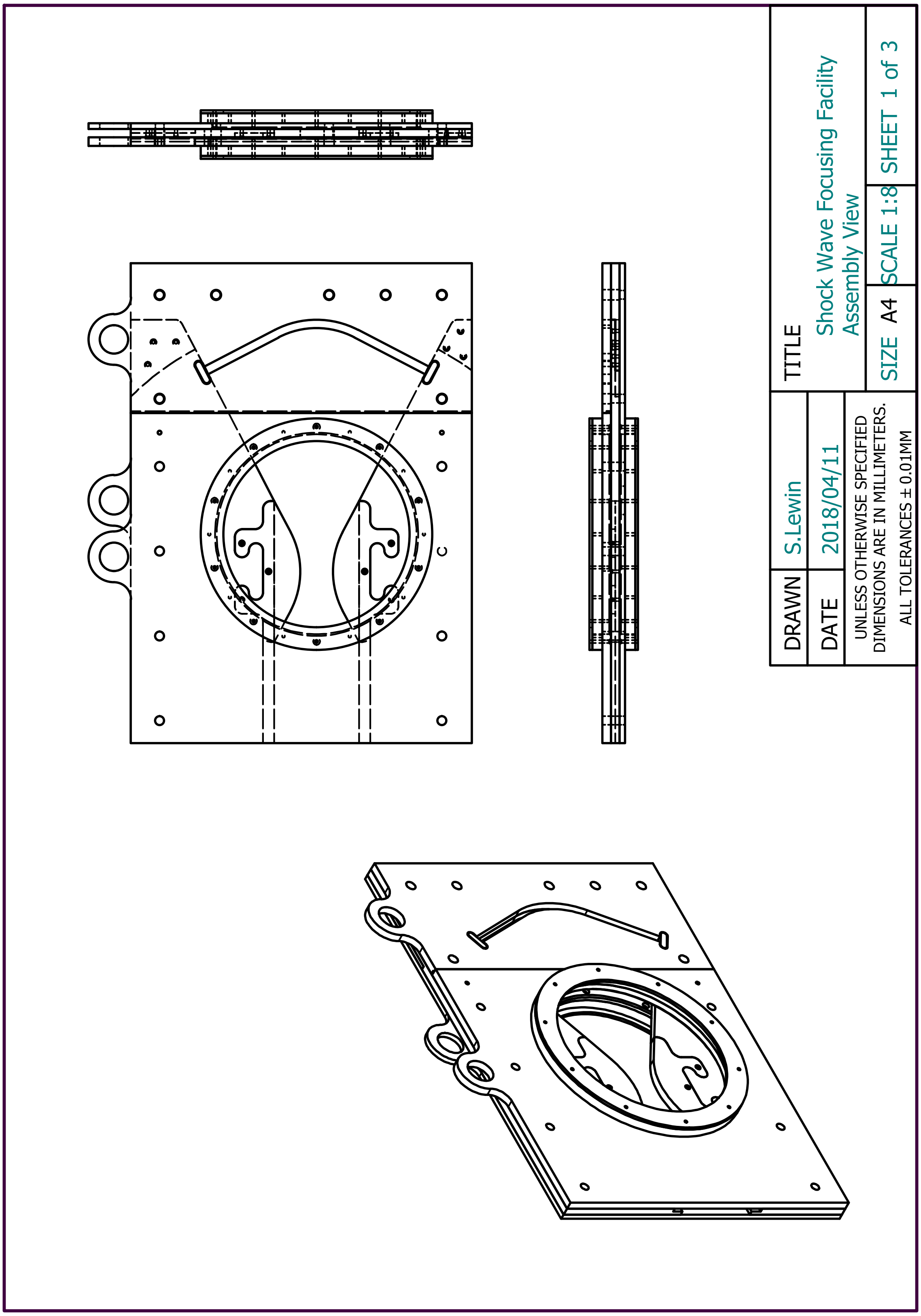

Figure B.1: Assembly view of experimental facility

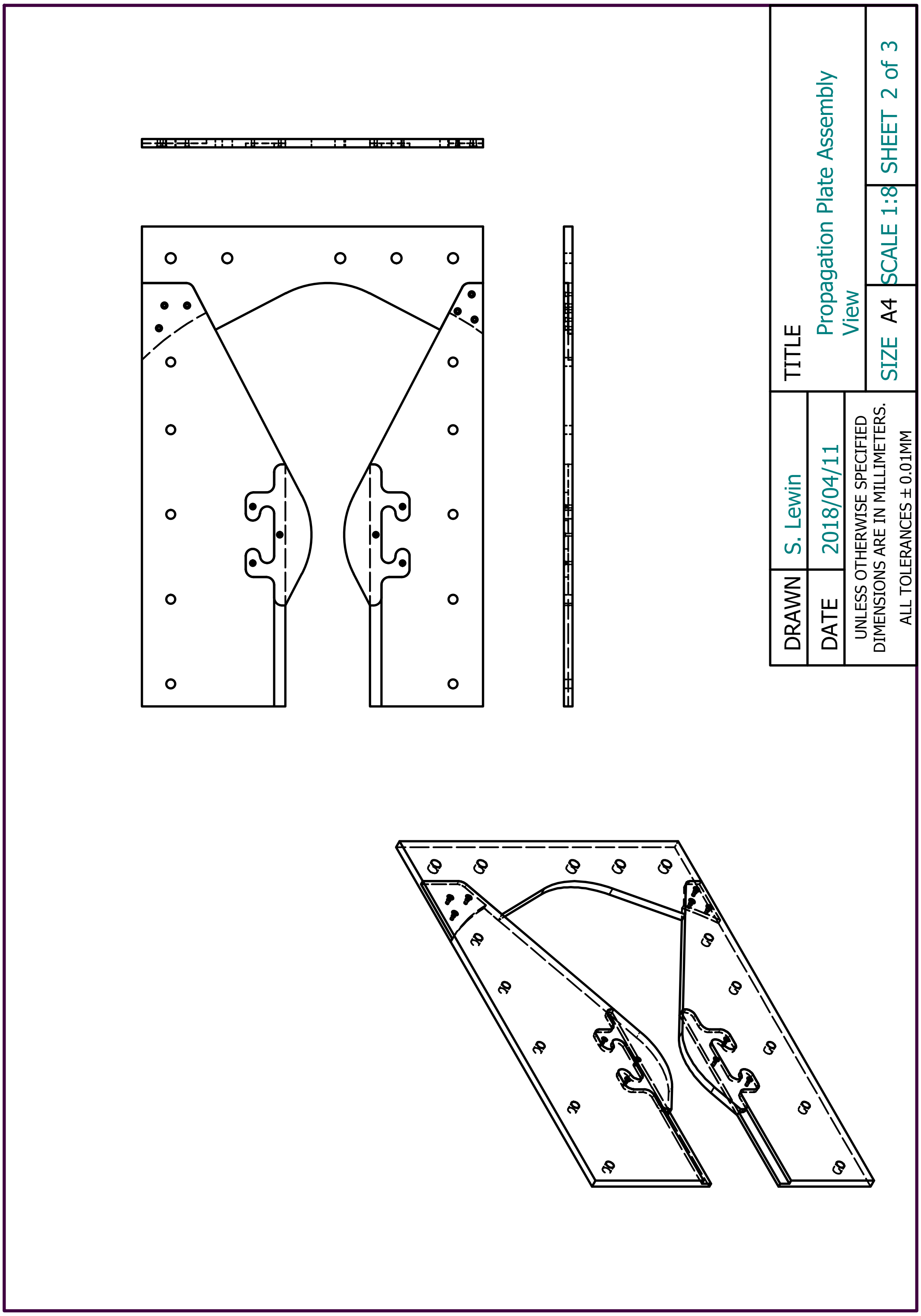

Figure B.2: Assembly view of propagation plate

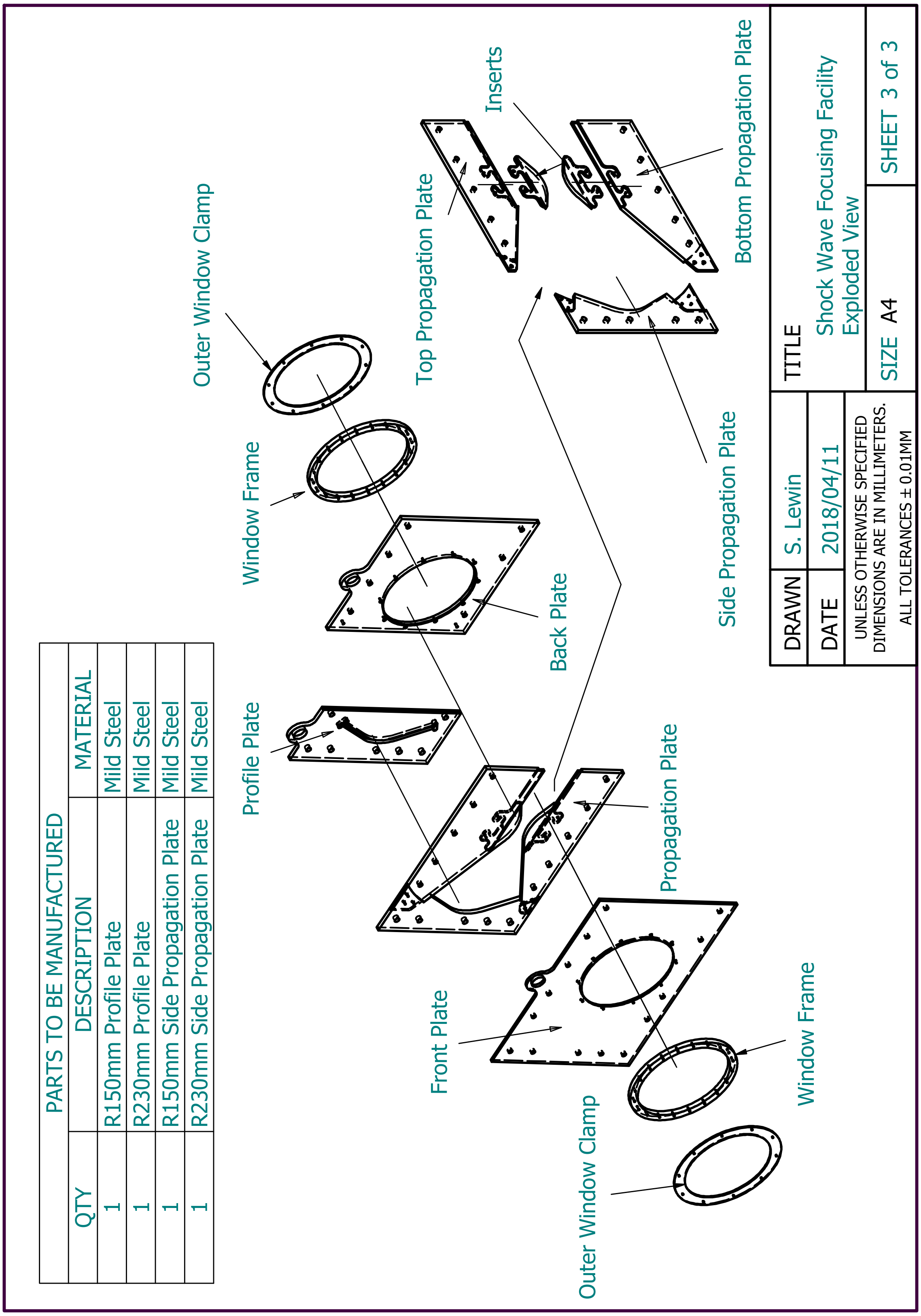

Figure B.3: Exploded view of experimental facility

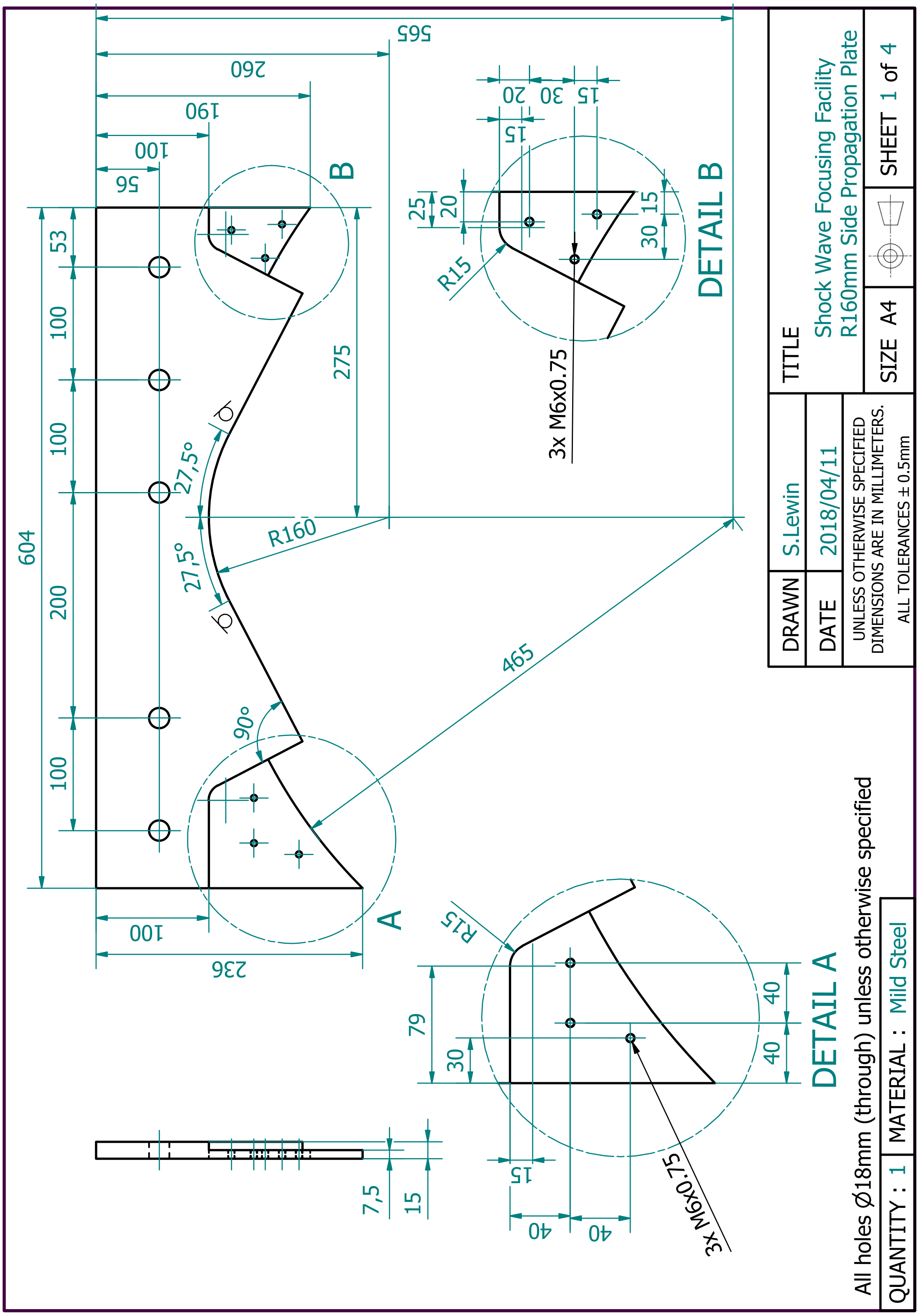

Figure B.4: Engineering drawing of side propagation plate for a shock wave with an initial curvature radius of 145 mm

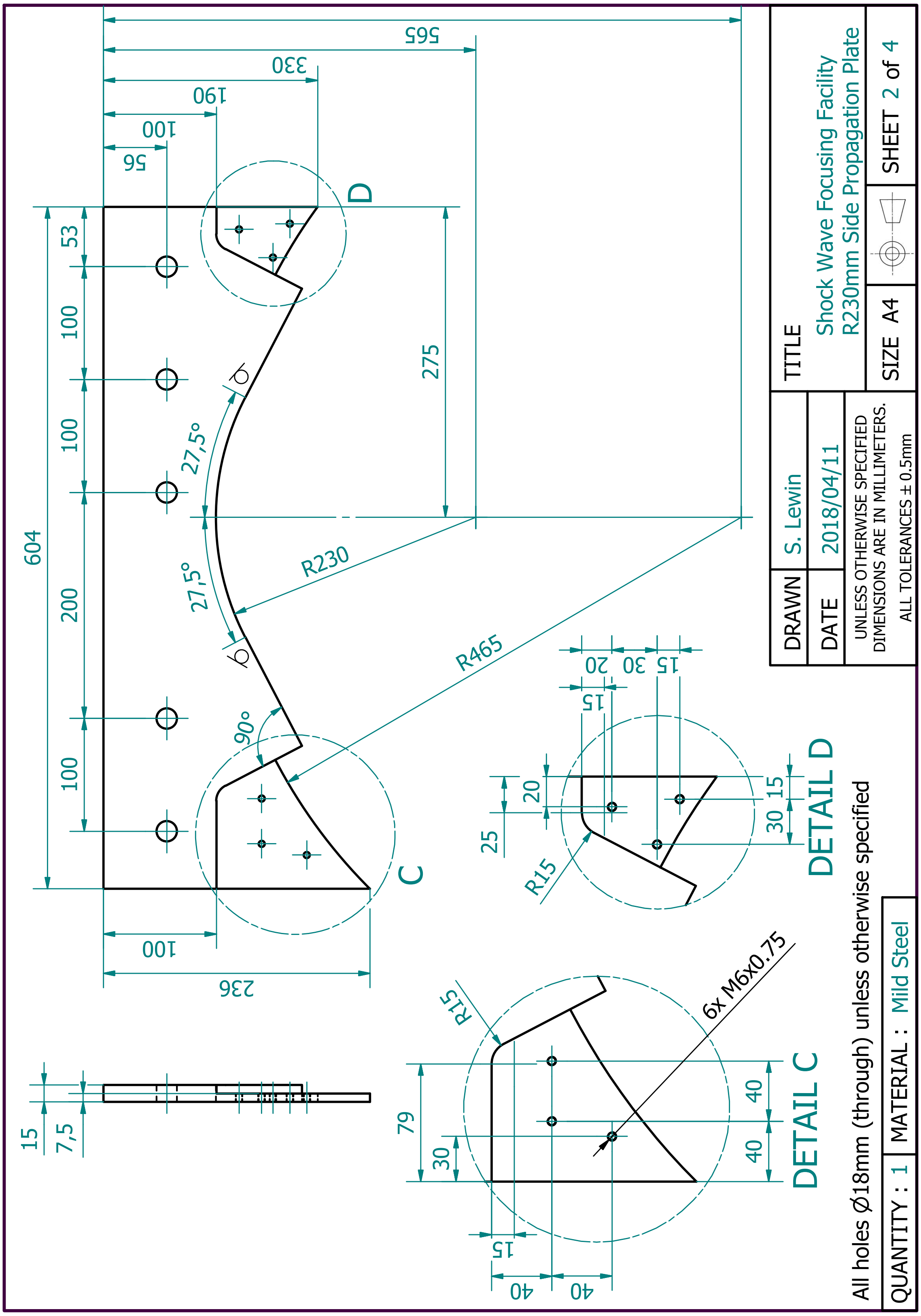

Figure B.5: Engineering drawing of side propagation plate for a shock wave with an initial curvature radius of 215 mm

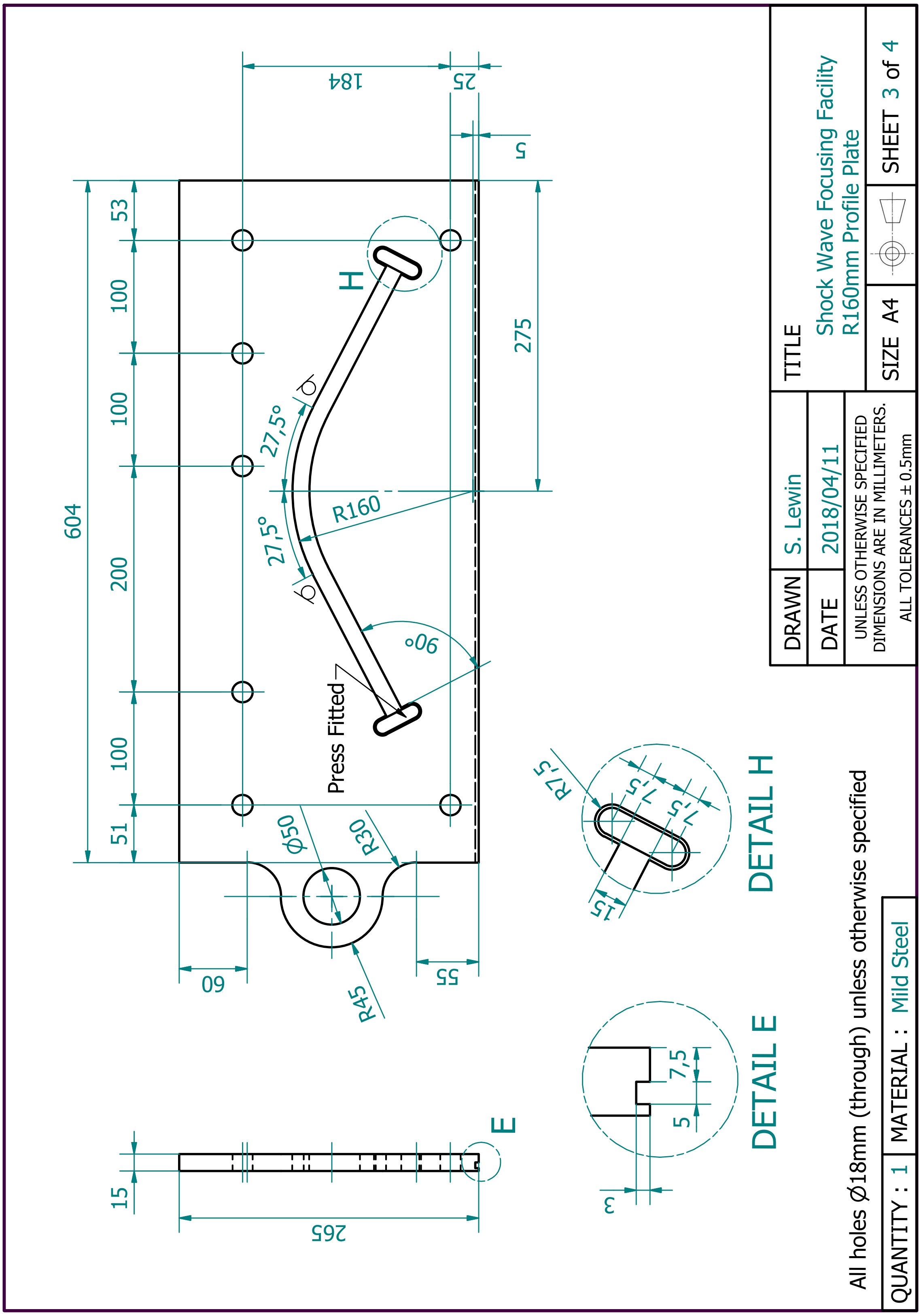

Figure B.6: Engineering drawing of profile plate for a shock wave with an initial curvature radius of 145 mm

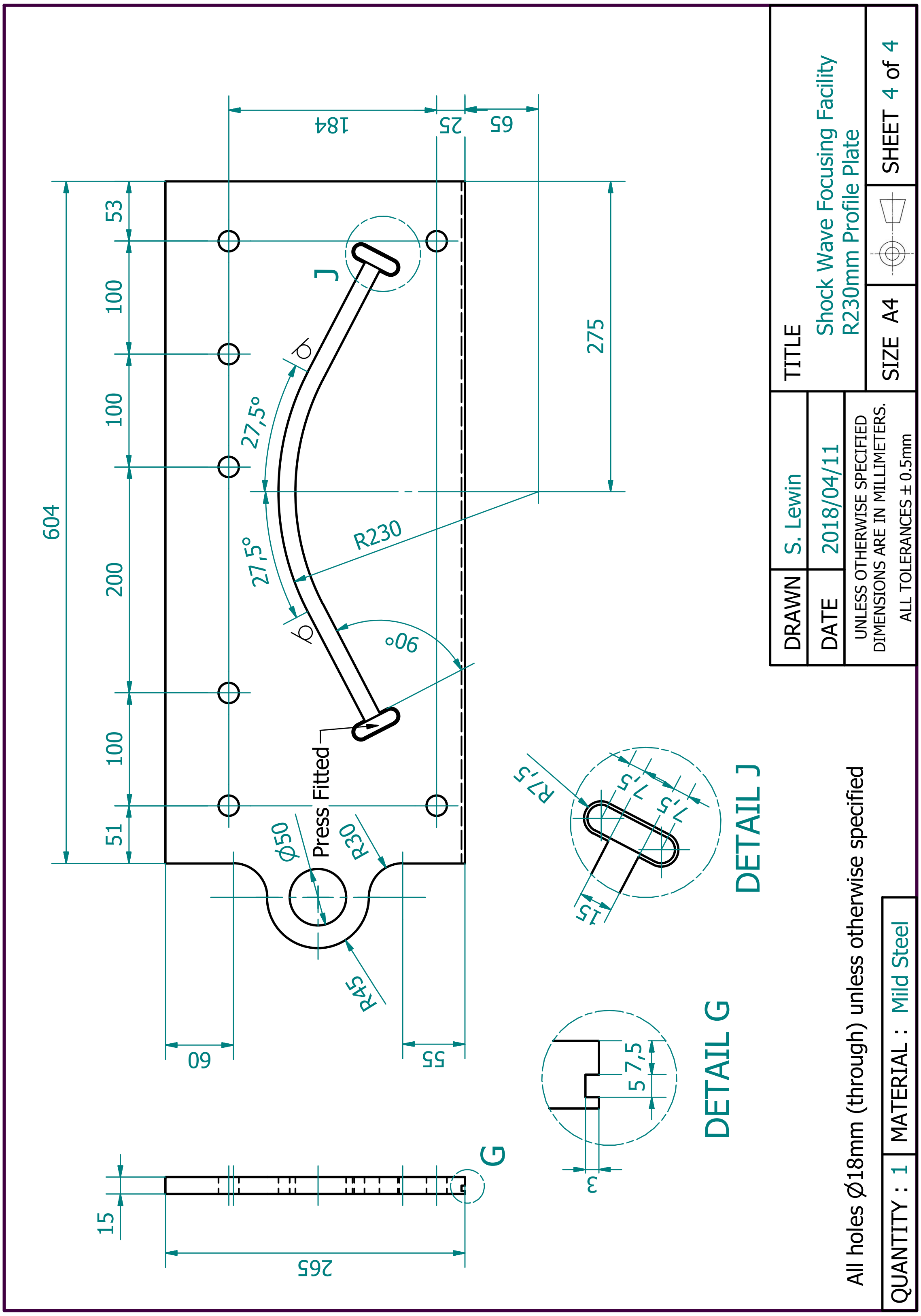

Figure B.7: Engineering drawing of profile plate for a shock wave with an initial curvature radius of 215 mm

Appendix C Product Information for the Optical Equipment and Auxiliary Instrumentation

The information required for identifying the optical equipment and instrumentation used in the experimental component of this investigation are given in Table C.1.

Table C.1: Product information of optical equipment and instrumentation

Product Name	**Manufacturer**	**Part / Model Number**	**Serial Number**
LabLight MR-LL17	Megaray	MR9000-11000	LL175-002-15
FASTCAM SA5 High-Speed Camera	Photron	775K-C1	362429074
Signal Conditioner	PCB Piezotronics	482A04	2082
Oscilloscope	Hantek	-	-

Appendix D LSDST Operating Procedure

D.1 Start-up procedure

At the beginning of each day of testing, prior to commencing any tests, the following actions are executed.

1. All instrumentation is switched on. This includes the camera, laptop, signal conditioner, oscilloscope, trigger unit and delay box.
2. The globe valve which controls the workshop air supply is opened. Sufficient pressure must be supplied to allow efficient tightening and loosening of the nuts which secure together the driver and driven sections of the tube.

D.2 Testing procedure

1. Determine the diaphragm required (in terms of its thickness) for the current test and fit it across the inlet to the driven section on the driver flange. Secure it with masking tape.
2. Slide the driver closed and fit the securing nuts.
3. Close all the valves on the control panel, except the ball valve for venting the driver.
4. Open the pneumatic wrench ball valve and using the necessary Personal Protective Equipment (PPE) and pneumatic wrench, tighten the nuts in a star-shaped pattern (this ensures that tightening of subsequent nuts do not loosen those that have already been tightened).
5. Close the pneumatic wrench ball valve.
6. Record the ambient temperature in the laboratory.

7. Confirm that the correct oscilloscope and camera settings have been specified.
8. Set the trigger unit delay required for the current test.
9. Arm the trigger unit and the oscilloscope (it must say "waiting for trigger").
10. Ensure that the camera is ready for a recording.
11. Lock the doors to the testing room and sound the alarm to notify any persons in the vicinity that a test is about to commence.
12. Switch on the light source.
13. Wearing hearing protection, proceed to the control panel. Close the driver vent ball valve and open the driver ball valve.
14. Slowly open the glove valve to pressurize the driver vessel.
15. Continue opening the globe valve until the diaphragm spontaneously ruptures. Upon the diaphragm's rupture, the pressure measured by the gauge is noted (this is the burst pressure of the diaphragm). The globe valve and the driver ball valve is immediately closed, and the driver vent ball valve is opened.
16. Switch off the light source.
17. Record the burst pressure, trigger delay and the interval of time between the first voltage spike experienced by each channel (this is required so that the Mach number of the shock generated by the tube can be determined).
18. Save the relevant images from the test and the corresponding image numbers.
19. Open the pneumatic wrench ball valve.
20. Loosen and remove the driver securing nuts.
21. Close the pneumatic wrench ball valve.
22. Slide the driver vessel open.
23. Remove and dispose of the ruptured diaphragm.

D.3 Shut-down procedure

At the end of each day of testing, the following actions are executed.

1. Close the globe valve controlling the workshop air supply.
2. Switch off all instrumentation.

D.4 Precautions

1. Before commencing a test, ensure that the pressure transducers are working by checking that the oscilloscope is displaying signals from the corresponding channels.

2. Hearing protection must be worn while operating the pneumatic wrench.

3. Ensure that the nuts which secure the driver to the driven section of the tube have been tightened sufficiently. If any of the nuts are loose, air may leak from the interface between the driver vessel and expansion chamber, and it will take longer to pressurize the driver.

4. Hearing protection must be worn while running the shock tube.

5. A whistle must be sounded immediately before the globe valve for pressurizing the driver is opened. Thereafter, it is sounded each time the pressure gauge on the control panel indicates, that the pressure in the driver has increased by approximately half a bar. This alerts any persons in the vicinity of the test room of the impending test.

6. Ensure that all diaphragm fragments have been cleared from the tube and the apparatus' slit. Any fragments left in the tube or test section will interfere with the shock generated in the subsequent test and thus compromise that test's results.

7. Before proceeding with the next test, ensure that the oscilloscope has recorded a pressure trace and that the camera has recorded images from the test.

Appendix E Determination of Shock Wave Velocity in the Experiments

E.1 Converting image coordinates to real coordinates

In each experiment, high-speed images of the shock wave propagation were captured at intervals of approximately 24 μs. To compare the positions of the shock wave and its velocity at the axis of symmetry, in the experimental images, to the values predicted by the CFD, any point on the shock front needs to be measured relative to a datum common to the CFD and the experiment. The datum assumed for this was the origin in the CFD; the centre-point of the leading edge of the slit. The coordinates, in pixels, of any point taken from the experimental images had to be converted into coordinates in millimetres, and then transformed into a measurement relative to the selected datum. The method employed for this was adapted from Gray (2014).

Since the leading edge of the slit is not captured in the images, it was first necessary to identify a point common to all frames from which the distance to the datum was known. In Figure E.1, the region of the propagation chamber visible in the viewing window is shown. The window frame intersects the walls of the propagation chamber at the points A and B, and the horizontal and vertical distance from the datum to any point on the line AB can be obtained from the engineering drawings of the facility. By measuring a point on the image relative to any point on this line, and applying the appropriate translations, the coordinates of the point can be converted into a measurement relative to the datum. The midpoint of line AB (x_m, y_m) was chosen as this common reference point, as it lies on the same line as the datum, and thus, only a horizontal translation would need to be applied to any point. The coordinates of any point on the image in pixels (x_i, y_i) was transformed relative to the midpoint with Equation E.1,

$$(x'_{im}, y'_{im}) = (x_i - x_m, -(y_i - y_m)) \tag{E.1}$$

where the midpoint of line AB is given by Equation E.2 as,

$$(x_m, y_m) = \frac{1}{2}(x_A + x_B, y_A + y_B) \tag{E.2}$$

and the negative sign in Equation E.1, in front of the transformation of the y-coordinate, is required to convert the coordinates from the left-handed coordinate system, used in the images, to the conventional right-handed coordinate system, used in the CFD. An adjustment for the tilt of the image was then applied using Equation E.3.

$$\begin{bmatrix} x_{im} \\ y_{im} \end{bmatrix} = \begin{bmatrix} \cos\theta_t & -\sin\theta_t \\ \sin\theta_t & \cos\theta_t \end{bmatrix} \begin{bmatrix} x'_{im} \\ y'_{im} \end{bmatrix} \tag{E.3}$$

θ_t is the angle at which the image was tilted and was calculated with Equation E.4.

$$\theta_t = \arctan\left(\frac{x_B - x_m}{y_B - y_m}\right) \tag{E.4}$$

Finally, the coordinates of the point in millimetres with respect to the specified datum (x, y) are obtained with Equation E.5.

$$(x, y) = (Sx_{im} + x_{0m}, Sy_{im}) \tag{E.5}$$

In Equation E.5, x_{0m} is the horizontal distance between the midpoint of AB and the datum, and S is the scale of the image, which was determined from Equation E.6 as,

$$S = \frac{H}{AB} \tag{E.6}$$

where H was obtained from the engineering drawings of the facility as 218 mm, and AB was determined with Equation E.7.

$$AB = \sqrt{(x_B - x_A)^2 + (y_B - y_A)^2} \tag{E.7}$$

To reduce the error from the choice of points A and B, the values in Equation E.2, E.4 and E.7 were taken as the average across all frames and tests.

E.2 Calculating the shock velocity at the axis of symmetry

In each experiment, the velocity of the shock wave at the axis of symmetry was determined from the change in its position in successive frames. The point on the shock front which coincides with the axis of symmetry is the midpoint. For each frame, this was determined from the coordinates of the top and bottom of the shock front. The average velocity $\overline{v}$ between two frames was then obtained from Equation E.8,

$$\overline{v} = \frac{\Delta x}{\Delta t} \tag{E.8}$$

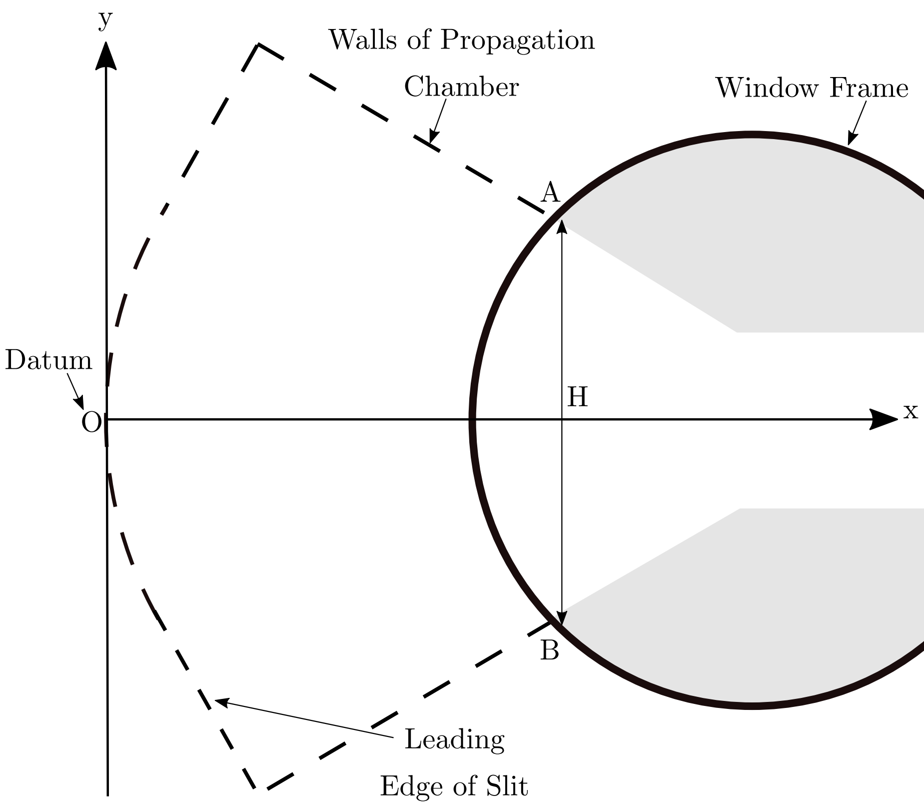

Figure E.1: Reference schematic for transformation of image coordinates in pixels to real coordinates in millimetres, with respect to the specified datum (O)

where Δx is the change in the horizontal position of the shock front between the two frames (since we are determining the velocity at the axis of symmetry, there is no change in the vertical position of the shock front at this point), and Δt is the interval of time between the two frames. Equation E.8 then gives the instantaneous velocity in-between the two frames.

If the velocity is calculated between successive frames, the error in the Mach number in the worst case was 13.7 %. This was reduced to 3.3 % by calculating the velocity over four frames, which corresponded to a time interval of 95 μs. This time interval was chosen since any further increase in this interval did not result in a significant decrease in the error.

E.3 Uncertainty in the shock Mach number

The uncertainty ΔM in the Mach number of the shock wave at the axis of symmetry is given by,

$$\Delta M = \frac{\Delta \overline{v}}{a} \tag{E.9}$$

where a is the acoustic velocity of the air within the propagation chamber, which was determined from Equation 1.1 and the ambient temperature in the laboratory at the time of each test. $\Delta\overline{v}$ is the uncertainty in the shock velocity, which is given by,

$$\Delta\overline{v} = \frac{\Delta(\Delta x)}{\Delta t} \tag{E.10}$$

where $\Delta(\Delta x)$ is the uncertainty in the position of the shock front at the axis of symmetry and was taken as half the width of the shock front in each frame.